Optoelectronic Device Modeling of GaAs Nanowire Solar Cells

by

Kyle Robertson

Thesis submitted to the
Faculty of Graduate and Postdoctoral Studies
In partial fulfillment of the requirements
For the M.Sc degree in
Physics

Department of Physics
Faculty of Science
University of Ottawa

© Kyle Robertson, Ottawa, Canada, 2019

Abstract

Nanowire solar cells have great potential as candidates for high efficiency, next-generation solar cell devices. To realize their potential, accurate and efficient modeling techniques encompassing both optical and electrical phenomena must be developed. In this work, a coupled optical and electronic model of GaAs nanowire solar cells was developed, with the goal of building a platform for automated, algorithmic device optimization.

Significant work was done on the optical portion of model, with the goal of reducing runtimes and improving the level of automation. Enhancements were made to an open-source implementation of the Rigorous Coupled Wave Analysis method for solving Maxwell's equations, to make it more accurate for modeling nanowire solar cells. Its accuracy and efficiency were thoroughly investigated, and with the enhancements presented here it was shown to be an effective technique for rapid optical modeling of nanowire devices. Purely optical optimizations of a sample AlInP-passivated GaAs nanowire on a GaAs substrate were performed to demonstrate the efficacy of the technique using a Nelder-Mead simplex optimization of device geometry.

The optical model was then coupled into a finite volume method based electrical model implemented in TCAD Sentaurus, to compute device efficiencies and ultimately optimize electrical device performance. As a first step, an algorithmic optimization of a p-i-n nanowire solar cell consisting of an AlInP-passivated GaAs nanowire on a Si substrate was performed using the generation rates computed by the enhanced RCWA implementation. The overall geometry was fixed to the result of the optical optimization, and only internal electrical parameters were optimized. The results showed that significant performance improvements can be obtained with the right choice of doping levels and doping region configurations, even without optimizing the global device geometry.

Acknowledgements

First and foremost, I would like to thank my advisor Jacob Krich. My path through this degree was not always conventional, but your endless patience, compassion, and guidance made it all possible for me. I could not have asked for a better advisor. It was a privilege to work with you, and I truly cannot thank you enough.

I would also like to thank my parents, Tammy and Wes, for their unwavering support in all aspects of my life. Had a bit of a rough go at the end of this thing, but you both saw me through it and I will always be grateful for that.

Big thank you to Ray Lapierre and Paige Wilson for being awesome collaborators, and for the many helpful discussions we had. Many of the wonderful things I experienced and things I accomplished while working on this degree would not have been possible without both of you.

I would be remiss if I didn't thank both Anna Trojnar and Matt Wilkins. Anna, for all the work she did on this project and the trail of breadcrumbs she left for me to follow. Matt, for his invaluable physical insight and willingness to share his mastery of Sentaurus.

Of course, gratitude goes to my partner Delainey for reminding me that there is much more to life than work and physics. Adventure is the spice of life, and you've always had a heavy hand.

Finally, thanks to all my physics peers out there. You made the hard parts bearable and the easy parts fun, and I certainly could not have made it this far alone.

Dedication

To all the other physics students out there. If I can do it, you can. Go get 'em.

Table of Contents

1 Introduction **1**

1.1 Literature Review and Motivation 1

1.2 Thesis Outline, Objectives, and Statement of Originality 3

Nomenclature **1**

2 Basic Operating Principles of a Solar Cell **5**

2.1 Introduction 5

2.2 Optical Processes 5

2.2.1 Maxwell's Equations in Dielectric Media 6

2.3 Electrical Processes 10

2.3.1 Carrier Statistics 11

2.3.2 Band Gap Narrowing 12

2.3.3 Recombination Model 13

2.3.4 Interface Transport 15

2.3.5 Doping Dependent Mobilities 17

3 Simulation Methods **19**

3.1 Rigorous Coupled Wave Analysis 19

3.2 Maxwell's Equations and the Plane Wave Representation of the Fields . . . 19

3.3 Fast Fourier Factorization Rules 22

3.4 Computing the Layer Eigenmodes 25

3.5 Electric and Magnetic Fields 27

3.6 Scattering Matrix Method 28

4 Verification of RCWA **31**

4.1 Introduction 31

4.2 RCWA 33

4.3 Continuous variable formulation 39

4.4 Rescaling technique 42

4.5 Conclusion 45

5 Optical Optimization of Passivated GaAs Nanowires on GaAs Substrates **47**

5.1 Introduction 47

5.2 Methods 48

5.3 Results 51

5.4 Conclusion 52

6 Electrical Optimization of Passivated GaAs Nanowires on Silicon Substrates **55**

6.1 Introduction 55

6.2 Optical-to-Electrical Conversion 57

6.3 Convergence Testing 59

6.4 Electrical Model and Optimization 60

6.5 Results 62

6.6 Conclusion 66

7 Conclusion & Future Work **68**

APPENDICES **69**

A Derivation of Fourier Space Maxwell's Equations **70**

B Phasor Notation **72**

B.1 Setting Amplitudes in S4 73

References **76**

Chapter 1

Introduction

As global energy demand increases by roughly 2% per year and the threat of global climate change looms near, it becomes imperative to explore clean, renewable methods of energy generation. Photovoltaics (PV) are a cost effective, efficient source of renewable energy consuming a rapidly increasing fraction of the global energy market [1]. With efficiency improvements of market standard PV technologies stalling, it is imperative to explore new, innovative PV technologies that have potential for high power conversion efficiency. Nanowire solar cells (NWSC) are a new, underexplored PV technology that have the potential to circumvent existing challenges in PV and boost efficiencies of existing devices.

1.1 Literature Review and Motivation

Nanowires are nanometer-scale, columnar structures with varying cross-sectional geometry that exhibit many useful properties for the fabrication of optoelectronic devices. Nanowires have found applications in a wide range of devices, from photodetectors and light emitting diodes to solar cells. Functional solar cell devices based an nanowire technology have only recently become viable due to advances in nanowire fabrication and characterization techniques. This section provides a brief overview of the existing literature on nanowire solar cells, and seeks to motivate the research contained in this thesis.

Nanowire solar cells have many advantages over the planar solar cells which currently dominate the field of PV. Through simulation, Anttu showed that with the appropriate set of parameters nanowire solar cells have the potential to exceed the Shockley-Quiesser limit of equivalent planar solar cells [2]. This stems from the reduced emissivity of nanowires relative to planar cells, which increases the open circuit voltage and boosts power conversion efficiencies. The favorable emission properties of nanowire solar cells, coupled with their reduced material requirements relative to planar solar cells, open up the opportunity for cheaper, more efficient devices [3].

It has been well demonstrated that nanowires are remarkably effective broadband light aborbers with low sensitivty to the incident angle of light [4, 5, 6]. Wallentin et al. showed that ray optics models of nanowires do not sufficiently explain their high absorption, and

accurate optical modeling of nanowires requires consideration of wave optics [7]. This stems from the fact that optimal nanowire shapes have geometric dimensions comparable to wavelengths found in the solar spectrum [8, 9]. Computational and analytical wave optics modeling performed by several research groups demonstrated that nanowires exhibit high absorption, despite small cross-sectional dimensions, due to resonant absorption phenomenon [10, 11, 12, 13, 8, 9]. The absorption behavior predicted by modeling has been confirmed by experiment in various semiconductor systems [14, 6, 15, 16, 13, 17].

The semiconductor materials used to fabricate nanowires have high refractive index contrast relative to their surrounding medium, allowing them to couple incident light into a number of wavelength-dependent waveguide modes. The excitation wavelength and strength of these modes are dependent on the geometric parameters of the nanowire, namely diameter, length, and in the case of nanowire arrays the array periodicity [12, 18]. Because it is possible to tune the resonant wavelength of nanowires by modifying their geometry, device fabricators can customize absorption profiles to suit a particular purpose [19].

In addition to their excellent optical properties, nanowires have features that are useful for charge carrier collection. One of the most intriguing features is the ability to grow nanowires on top of cheap, lattice mismatched substrates. Because nanowires have finite cross-sectional dimensions, they are able to accomodate the strain induced by growth on lattice mismatched substrates without introducing carrier-trapping defects in the crystal lattice [20, 21]. This opens up the avenue for both cost-effective single junction solar cells and multi-junction solar cells grown on silicon [22]. The columnar structure of nanowires also presents the opportunity for orthogonalizing the direction of light absorption and carrier collection via radial junction nanowire solar cells [23]. In a radial junction nanowire solar cell the p-n and p-i-n materials are arranged in radial layers moving outwards from the center of the nanowire, as opposed to along the axis of the nanowire [24, 25] (see Fig. 1.1). This allows the growth of long nanowires that maximize light absorption without increasing the distance charge carriers must travel to reach collection contacts, thereby increasing device efficiencies [4, 26, 27].

Despite the promise of nanowire solar cells, challenges remain. The current record efficiencies for bottom-up grown GaAs and InP nanowire solar cells are 15.3% and 13.8% respectively [1], which are both significantly lower than their thin film counterparts (28.8% for GaAs and 22.% for InP) [29, 7, 30]. These lower efficiencies are primarily caused by challenges in nanowire fabrication. First, the high surface-to-volume ratio of nanowires means there is a high concentration of surface states which trap carriers and prevent them from being collected. This problem has been mitigated by introduced passivating shells of higher band gap material around the nanowire core, but passivation adds an additional fabrication step that reduces the cost efficiency of nanowire solar cells [31, 32, 33, 34, 35, 36]. Fine control of doping during device fabrication is also a current issue [37, 38, 39, 40, 41, 42]. It has been shown that proper doping levels are critical to device performance [43, 44].

The large design parameter space of nanowires requires careful optimization to maxi-

[1]van Dam et. al. fabricated a top-down InP nanowire solar cell by etching material away from an epitaxially grown planar structure that reached an efficiency of 17.8% [5]

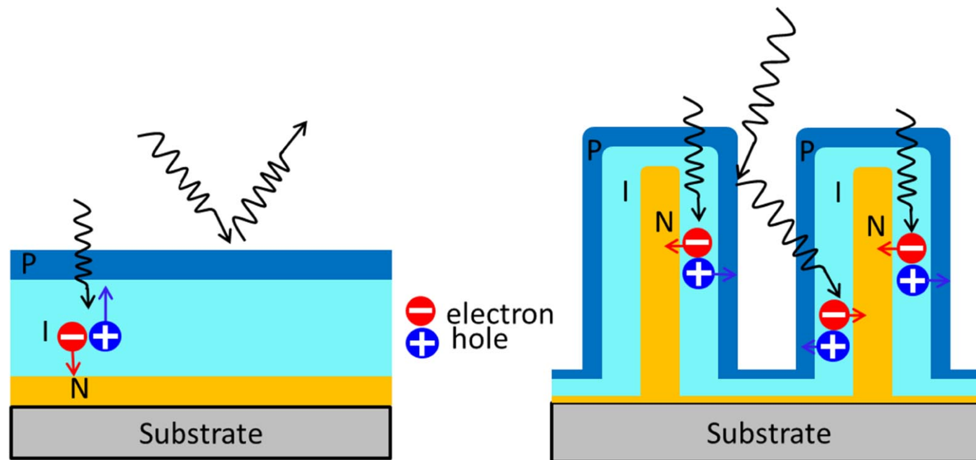

Figure 1.1: A axial p-i-n junction planar solar cell (left) radial p-i-n junction nanowire solar cell (right), reproduced from [28]. In the radial junction solar cell the direction of carrier collection is perpendicular to the direction of photon propagation.

mize device performance. There is a substantial existing body of literature on both computational and analytic modeling of NWSC, but in most cases either purely optical or electrical models are constructed with the other component of the model being overly simplistic or omitted entirely [45, 46, 44, 27, 16, 47]. The body of literature on fully coupled optoelectronic modeling is much smaller, and all cited authors use either the finite difference time domain (FDTD) technique or finite element method (FEM) for their optical models [26, 48, 49, 32]. While these techniques are highly accurate, they are computationally expensive, limiting their usefulness in a closed loop, global device optimization. Thus there is a need to develop fast, accurate optical modeling techniques for NWSC that can be easily coupled into a drift-diffusion based electronic model. The development of faster optical modeling techniques would admit global, algorithmic optimization of all key performance-related device parameters, a study that has yet to be published in the literature and would be hugely beneficial to the research community.

1.2 Thesis Outline, Objectives, and Statement of Originality

In this thesis, I built a fully automated optoelectronic device model of nanowire solar cells. For the optical component, I implemented an enhanced form of the optical modeling algorithm Rigorous Coupled Wave Analysis (RCWA) and applied some novel postprocessing techniques to maximize accuracy of the outputs of the model while minimizing computational cost. Previous optical models reported in the literature have used finite element and finite difference methods for optical modeling of NWSC, but there is little to no literature on the use of RCWA in this field. The structure of nanowire arrays is conducive to modeling via the more computationally efficient RCWA technique, making it an appropriate choice. I verify the accuracy of my enhanced RCWA implementation and postprocess-

ing techniques on a test nanowire system, and show that it captures essential physics at material interfaces that a vanilla implementation of RCWA does not. I then use my implementation to perform an algorithmic optimization of key geometric device parameters to maximize optical absorption.

The full 3D optical model is coupled into a 2D drift-diffusion based electronic model using the industry standard, Finite Volume Method software TCAD Sentaurus by Synopsys. To do this, I constructed an automated software system to take the 3D outputs of the optical model and interpolate them onto the 2D irregular grid used in the electronic model. I then used the electronic model to analyze an example nanowire system, and performed a unique, algorithmic optimization of some key electronic device parameters to maximize device efficiency. To the best of my knowledge, no such algorithmic optimization of a NWSC has been reported in the literature.

Chapter 2 of this thesis is used to establish the essential background physics and mathematics used by the optical and electrical model. Chapter 3 presents the mathematical foundations of RCWA. Chapters 4 and 5 are dedicated to establishing the enhancements I made to RCWA to increase its accuracy, and testing the enhanced implementation on some example nanowire systems. Chapter 6 uses the optimized output of the optical model to perform electronic optimizations of an example NWSC.

Chapter 2

Basic Operating Principles of a Solar Cell

2.1 Introduction

Photovoltaic devices convert light energy into electrical energy that may be harnessed to do useful work. A solar cell is the basic building block of a photovoltaic device. It is typically modeled as a small unit cell containing layers of semiconductor material with electrical contacts on the top and bottom of the device.

Modeling of solar cells can be broken down into analysis of two logically separate key processes. The first process is the optical process, by which incident light is absorbed by the cell and converted into collectable charge carriers. The second process is the electrical process, by which these generated carriers move through the cell and are collected at the contacts to do work. The next two sections lay out the mathematical underpinnings for these processes, and outline the physical phenomena accounted for in our model. A method for computing the optical generation from the electric field intensity is derived in Section 2.2, and used within our optical model to compute generation rates from the fields produced by the employed numerical technique (RCWA). Section 2.3 describes in mathematical detail the physical phenomena accounted for in our electrical model, to give the reader a sense of what approximations and assumptions underlie our results.

2.2 Optical Processes

The primary goal when optically modeling solar cells is to compute the carrier generation rate $g(\vec{r}, \lambda)$. This quantity gives the number of charge carriers that are generated per unit volume per unit wavelength of incident light per unit time at a given point $\vec{r}$ in the device. The amount of generation is strongly dependent on the incident wavelength of light. To compute the total generation of the entire spectrum, one must integrate over wavelength

$$G(\vec{r}) = \int g(\vec{r}, \lambda) d\lambda. \tag{2.1}$$

The simplest optical model of a single junction planar solar cell assumes light absorption is governed by the one-dimensional Beer-Lambert absorption law for a material of uniform absorption coefficient α [50]

$$I(\lambda, x) = I(\lambda, 0)e^{-\alpha(\lambda)x} \tag{2.2}$$

which states that the initial intensity of light $I(0)$ is exponentially attentuated with depth x according to the absorption coefficient α of the illuminated material. This model assumes that absorption is uniform in all directions orthogonal to $\hat{x}$. If we then assume that every above band gap photon absorbed from the incident light generates an electron-hole pair, this Beer-Lambert absorption can be easily used to compute a carrier generation rate. If the intensity I is expressed as a spectral irradiance in units of power per unit area per unit wavelength, then one can compute the generation rate via

$$g(x, \lambda) = \frac{\lambda}{hc} I(\lambda, 0)\alpha(\lambda)e^{-\alpha x} \tag{2.3}$$

where we have divided the spectral irradiance I by the photon energy hc/λ to arrive at a photon flux.

This simple model inherently assumes that the modeled solar cell is uniform and has infinite extent in the plane. This assumption is invalid for nanowire solar cells, and because the dimensions of the geometric features in nanowires are comparable to wavelengths present in the solar spectrum, a full solution to Maxwell's equations is required to accurately compute carrier generation rates.

2.2.1 Maxwell's Equations in Dielectric Media

To accurately compute carrier generation rates in a nanowire solar cell, one must solve Maxwell's equations

$$\nabla \times \vec{E} = \frac{\partial \vec{B}}{\partial t} \qquad \text{Ampere's Law} \tag{2.4}$$

$$\nabla \times \vec{H} = \vec{J}_f - \frac{\partial \vec{D}}{\partial t} \qquad \text{Faraday's Law} \tag{2.5}$$

$$\nabla \cdot \vec{B} = 0 \qquad \text{Gauss' Law} \tag{2.6}$$

$$\nabla \cdot \vec{D} = 0 \qquad \text{Coulomb's Law} \tag{2.7}$$

along with the constitutive relations

$$\vec{D} = \epsilon \vec{E} \tag{2.8}$$

$$\vec{B} = \mu \vec{H} \tag{2.9}$$

for the electric field $\vec{E}(\vec{r})$ as a function of space. For the modeling of nanowire solar cells, we assume all materials are nonmagnetic meaning $\mu_r = 1$ and $\mu = \mu_0$

Because Maxwell's equations are linear, general solutions can be built as linear combinations of single-frequency solutions according to

$$\vec{H}(\vec{r}, t) = \int_{-\infty}^{\infty} d\omega \vec{\mathcal{H}}(\vec{r}, \omega) e^{i\omega t} \tag{2.10}$$

for a complex-valued phasor $\vec{\mathcal{H}}$ (with an identical form for $\vec{E}(\vec{r}, t)$) [1]. This linearity allows us to solve Maxwell's equations at a fixed (but general) temporal angular frequency ω using the form in the integrand of Eq. 2.10, and then recover the general solution at the end by integrating over frequency according to Eq. 2.10. The $e^{i\omega t}$ time dependence of the fields allow us to eliminate all the time derivatives using

$$\frac{\partial \vec{H}}{\partial t} = i\omega \vec{H} \tag{2.11}$$

$$\frac{\partial \vec{E}}{\partial t} = i\omega \vec{E}. \tag{2.12}$$

By inserting Eq. (2.9) into (2.4) and Eq. (2.8) into (2.5), we arrive at the frequency domain Maxwell's equations

$$\nabla \times \vec{\mathcal{E}} = i\omega\mu_0 \vec{\mathcal{H}} \tag{2.13}$$

$$\nabla \times \vec{\mathcal{H}} = -i\omega\epsilon \vec{\mathcal{E}} \tag{2.14}$$

$$\nabla \cdot \vec{\mathcal{H}} = 0 \tag{2.15}$$

$$\nabla \cdot \vec{\mathcal{E}} = 0. \tag{2.16}$$

where we have assumed the free current $\vec{J}_f = 0$. This assumption is valid at optical frequencies, which do not couple in a DC current component. The solution of these equations yields the full electric field $\vec{E}(\vec{r})$ everywhere in space at a single frequency. The ultimate goal is to compute the carrier generation rate. This can be done by computing the power absorbed from the fields by the propagation medium, which can then be related directly to the carrier generation rate. To achieve this goal, we begin with Poynting's theorem [51]

$$\frac{dW}{dt} = -\frac{d}{dt}\int_V \left(\frac{1}{2}\epsilon_0 |E|^2 + \frac{1}{\mu_0}|B|^2\right) dV - \frac{1}{\mu_0}\oint_S (\vec{E} \times \vec{B}) \cdot d\vec{a}. \tag{2.17}$$

This theorem tells us the time rate of change of the work W done on a system by the electromagnetic forces (i.e the rate of change of the total electromagnetic energy) equals the time rate of change of the energy stored in the fields (integrated over the volume)

[1] For more detail concerning this phasor notation, see Appendix B

minus the energy leaving the volume through its bounding surface. We can recognize the energy density (energy per unit volume) as

$$u = \frac{1}{2}\left(\epsilon_0|E|^2 \ + \ \frac{1}{\mu_0}\ |B|^2\right) \tag{2.18}$$

and the Poynting vector (areal energy flux density or energy transmitted per unit area) as

$$\vec{S} = \frac{1}{\mu_0}\vec{E} \times \vec{B}. \tag{2.19}$$

The Poynting vector is often written in a slightly different form by using the constitutive relations as

$$\vec{S} = \vec{E} \times \vec{H} \tag{2.20}$$

which can be expressed directly in terms of phasors as

$$\vec{\mathcal{S}} = \frac{1}{2}\vec{\mathcal{E}} \times \vec{\mathcal{H}}^* \tag{2.21}$$

where the factor of 1/2 comes from time averaging a time-oscillating field over a full temporal period. The physical power transmitted per unit area follows the real part of $\vec{\mathcal{S}}$.

If we imagine waves traveling through a vacuum, then $dW/dt = 0$ meaning

$$\int_V \frac{du}{dt} dV = -\oint_S \vec{S} \cdot d\vec{a}. \tag{2.22}$$

Applying the divergence theorem to the right hand side of Eq. (2.22) gives the relation

$$\oint_S \vec{S} \cdot d\vec{a} = \int_V \nabla \cdot \vec{S} dV \tag{2.23}$$

which when substituted back into Eq. (2.22) yields

$$\int_V \frac{du}{dt} dV = -\int_V \nabla \cdot \vec{S} dV. \tag{2.24}$$

By equating the two integrands, we can establish the following key equality

$$\frac{du}{dt} = -\nabla \cdot \vec{S} \tag{2.25}$$

which in words means the rate of change of the energy stored in the fields per unit volume is equal to minus the divergence of the Poynting vector. Eq. (2.25) is essential, as it tells us we can integrate either of these two quantities over a volume of material to determine how much electromagnetic energy is being absorbed by that material per unit time, i.e, the power loss. To compute the time averaged power loss, we must insert the time averaged

phasor representation of the Poynting vector (Eq. (2.21)) into the right hand side of Eq. (2.25), which gives

$$p_{abs} = -\nabla \cdot \mathrm{Re}(\vec{\mathcal{S}}) \tag{2.26}$$

$$= \frac{1}{2}\mathrm{Re}\left(-\nabla \cdot (\vec{\mathcal{E}} \times \vec{\mathcal{H}}^*)\right). \tag{2.27}$$

We can use the vector identity [51]:

$$\nabla \cdot (\vec{a} \times \vec{b}) = \vec{b} \cdot (\nabla \times \vec{a}) - \vec{a} \cdot (\nabla \times \vec{b}) \tag{2.28}$$

to write

$$\nabla \cdot (\vec{\mathcal{E}} \times \vec{\mathcal{H}}^*) = \vec{\mathcal{H}}^* \cdot (\nabla \times \vec{\mathcal{E}}) - \vec{\mathcal{E}} \cdot (\nabla \times \vec{\mathcal{H}}^*). \tag{2.29}$$

Using Eqs. (2.4) and (2.5) to replace the curls in Eq. (2.29) with time derivates and reinserting the result back into Eq. (2.27) gives

$$p_{abs} = \frac{1}{2}\mathrm{Re}\left(\vec{\mathcal{E}} \cdot \frac{\partial \vec{\mathcal{D}}^*}{\partial t} + \vec{\mathcal{H}}^* \cdot \frac{\partial \vec{\mathcal{B}}}{\partial t}\right). \tag{2.30}$$

Next, we can eliminate $\vec{\mathcal{D}}$ and $\vec{\mathcal{B}}$ using the constitutive relations to get

$$p_{abs} = \frac{1}{2}\mathrm{Re}\left(\epsilon\vec{\mathcal{E}} \cdot \frac{\partial \vec{\mathcal{E}}^*}{\partial t} + \mu\vec{\mathcal{H}}^* \cdot \frac{\partial \vec{\mathcal{H}}}{\partial t}\right). \tag{2.31}$$

which gives

$$p_{abs} = \frac{1}{2}\mathrm{Re}\left(-i\omega\epsilon\vec{\mathcal{E}} \cdot \vec{\mathcal{E}}^* + i\omega\mu\vec{\mathcal{H}}^* \cdot \vec{\mathcal{H}}\right) \tag{2.32}$$

The permitivity ϵ and permeability μ are both potentially complex quantities, which we write as

$$\epsilon = \epsilon_0(\epsilon' + i\epsilon'') \tag{2.33}$$

$$\mu = \mu_0(\mu' + i\mu''). \tag{2.34}$$

Inserting this into Eq. (2.32) yields

$$p_{abs} = \frac{1}{2}\mathrm{Re}\left[\omega(\epsilon_0\epsilon''\ |\vec{\mathcal{E}}|^2 - \mu_0\mu''|\vec{\mathcal{H}}|^2) + i\omega(\mu_0\mu'|\vec{\mathcal{H}}|^2 - \epsilon_0\epsilon'|\vec{\mathcal{E}}|^2)\right] \tag{2.35}$$

which, when fully simplified, gives the final result for the power absorbed per unit volume in any material

$$p_{abs} = \frac{1}{2}\omega(\epsilon_0\epsilon''\ |\vec{\mathcal{E}}|^2 - \mu_0\mu''\ |\vec{\mathcal{H}}|^2) \tag{2.36}$$

Although Eq. 2.36 was derived assuming waves in a vacuum for simplicity, it still holds for linear dispersive media with losses. See [52] Section 6.8 for a full derivation lacking the assumption of waves in a vacuum. Most semiconductor materials are nonmagnetic, meaning $\mu'' = 0$ and the second term drops out. Further intuitive confirmation of this

formula can be found by noting that in vacuum $\epsilon'' = \mu'' = 0$ and no power is absorbed. The final step is to relate the power loss to the carrier generation rate. First, we divide the power loss by the energy of the incident photons to get the number of photons absorbed per unit time, per unit frequency, per unit volume

$$g(\vec{r}, \omega) = \frac{1}{2}\epsilon_0 \hbar \epsilon''(\omega) |\vec{\mathcal{E}}(\vec{r}, \omega)|^2 \tag{2.37}$$

where $\epsilon''(\omega)$ is potentially frequency-dependent in dispersive media. We can use the following relationship between the imaginary part of the permittivity and the index of refraction

$$\epsilon'' = 2nk \tag{2.38}$$

where n is the real part and k the imaginary part of the index of refraction, to arrive at an alternative form for g:

$$g(\vec{r}, \omega) = \epsilon_0 \hbar n(\omega) k(\omega) |\vec{\mathcal{E}}(\vec{r}, \omega)|^2 \tag{2.39}$$

which has been used in the literature [48]

To model a nanowire solar cell illuminated by the solar spectrum, $g(\vec{r}, \omega)$ needs to be computed for many incident frequencies ω where the amplitude of the incident plane wave is scaled to the spectrum. The beauty of the existing optical model is the small number of material parameters required. One only needs to know the real and imaginary parts of the index of refraction (n and k) as a function of incident frequency. These material parameters are assumed to be fully parameterized by frequency, and are independent of all other system parameters (for example, doping levels). This means one must solve the optical problem only once for a given geometry when attempting to optimize doping levels in an electrical model, reducing computational expense. Dopant incorporation is known to narrow the band gap of a material, which could presumably have an effect on optical absorption. However, doping creates disordered, localized states within the band gap that do not strongly absorb light and therefore have minimal effect on n and k. Here we choose to ignore the effect of band gap narrowing in the optical model, which may slightly underestimate the amount of optical absorption and therefore underestimate the current collected in a full device model.

2.3 Electrical Processes

Electronic modeling of solar cells ultimately comes down to solving the coupled carrier transport equations [50, 53]

$$\frac{\partial n}{\partial t} = \nabla \cdot \vec{J}_n + R_n \tag{2.40}$$

$$\frac{\partial p}{\partial t} = -\nabla \cdot \vec{J}_p + R_p \tag{2.41}$$

$$J_n = \mu_n n \nabla \phi + D_n \nabla n \tag{2.42}$$

$$J_p = -\mu_p p \nabla \phi + D_p \nabla p \tag{2.43}$$

$$\tag{2.44}$$

and Poisson equation

$$\nabla^2 \phi = \frac{q}{\epsilon}(-\rho + n - p) \tag{2.45}$$

for the electron concentration n, hole concentration p, and electrostatic potential ϕ throughout the entire device where

1. $\vec{J}_{n/p}$ is the electron/hole current density
2. $R_{n/p}$ is the net electron/hole generation
3. $\mu_{n/p}$ is the electron/hole mobility
4. $D_{n/p}$ is the electron/hole diffusion constant, which by the Einstein relation is $D = \mu k_B T/q$
5. ϵ is the electric permittivity of the environment
6. ρ is the fixed charge density produced by ionized dopants
7. q is the fundamental charge
8. T is the temperature
9. k_B is Boltzmann's constant

For anything other than a simple 1D p-n junction, these equations must be solved numerically. The commercial drift-diffusion solver TCAD Sentaurus version vL2016.03 by Synopsys is used to solve Eqs. 2.40- 2.45. Modeling of different devices and materials come down to constructing different models for $J_{n/p}$ and $R_{n/p}$ and applying the appropriate boundary conditions for the system being studied. Sentaurus contains an enormous library of models for the underlying physics of carrier densities, carrier transport, recombination rates, and boundary conditions. The physical models used in this work will be described in the following sections.

2.3.1 Carrier Statistics

In semiconductor device modeling, it is common to use Boltzmann statistics to model the carrier concentration as a function of particle energy

$$n = N_c e^{(E_{F,n} - E_c)/kT} \tag{2.46}$$

$$p = N_v e^{(E_v - E_{F,p})/kT} \tag{2.47}$$

where N_c and N_v are the effective density of states for electrons and holes, $E_{F,n/p}$ is the quasi-Fermi energy of electrons/holes, and E_c and E_v are the energy of the conduction and valence band. This approximation is valid when the distance from the band edges to the Fermi level is larger than the average thermal energy of particles, in other words

$$\frac{E_c - E_{F,n}}{kT} \gg 1 \tag{2.48}$$

$$\frac{E_{F,p} - E_v}{kT} \gg 1. \tag{2.49}$$

However, these conditions can be violated (and thus the Boltzmann approximation invalid) if the semiconductor is highly doped or there is a high density of defect states in the band gap. Therefore, in order to model devices in the high doping regime Fermi-Dirac statistics must be used. To lift any doping limitations on our model, we use Fermi-Dirac statistics and the carrier concentrations become

$$n = N_c F_{1/2}((E_{F,n} - E_c)/kT) \tag{2.50}$$

$$p = N_v F_{1/2}((E_v - E_{F,p})/kT) \tag{2.51}$$

where $F_{1/2}$ represents the Fermi integral of the second kind

$$F_{1/2}(x) = \int_0^\infty \frac{y^{1/2}dy}{1 + e^{y-x}} \tag{2.52}$$

Letting

$$\eta_n = \frac{E_{F,n} - E_c}{kT} \tag{2.53}$$

$$\eta_p = \frac{E_v - E_{F,p}}{kT} \tag{2.54}$$

we can rewrite the carrier concentrations as

$$n = \gamma_n N_c e^{\eta_n} \tag{2.55}$$

$$p = \gamma_p N_v e^{\eta_p} \tag{2.56}$$

where the $\gamma_{n/p}$ can be seen as correction factors to the Boltzmann distribution for carriers and are equal to

$$\gamma_n = \frac{n}{N_c} e^{-\eta_n} \tag{2.57}$$

$$\gamma_p = \frac{p}{N_v} e^{-\eta_p} \tag{2.58}$$

2.3.2 Band Gap Narrowing

The band gap of a semiconductor can be modified by both temperature effects and the introduction of ionized impurities into the crystal lattice. In the case of lattice impurities, the electron-electron, electron-hole, electron-impurity, and hole-impurity many-body interactions cause charge carriers to experience a screened Coulomb potential, which reduces the impurity ionization energy and modifies the band structure [54, 55]. For high

doping densities, this band gap narrowing (BGN) effect becomes significant and must be incorporated to capture essential device physics.

A variety of different BGN models exist, each applicable within only a certain range of doping densities [56, 57, 58, 59]. To extend the range of applicability of our model, a table of BGN values as a function of acceptor and donor impurities density is built and linearly interpolated in the logarithm of the impurity concentration to arrive at a BGN model that is a continuous function of impurity concentration. Default Sentaurus values are used to populate the table for constructing the interpolation.

In the presence of BGN, one must use an effective bandgap $E_{g,eff}$ in all calculations

$$E_{g,eff}(T) = E_g(T) - E_{BGN} \tag{2.59}$$

where E_{BGN} is the energy shift produced by the chosen band gap narrowing model and the temperature dependence of the band gap is captured according to

$$E_g(T) = E_g(0) - \frac{\alpha T^2}{T + \beta} \tag{2.60}$$

where α and β are material dependent parameters and $E_g(0)$ is the band gap at 0 K. The reduced band gap affects the intrinsic carrier density, and an effective intrinsic carrier density $n_{i,eff}$ must be used in all calculations such that

$$n_i(T) = \sqrt{N_C N_V} e^{-\frac{E_G(T)}{2kT}} \tag{2.61}$$

$$n_{i,eff}(T) = n_i(T) e^{\frac{E_{BGN}}{2kT}} \tag{2.62}$$

2.3.3 Recombination Model

The net carrier recombination rate R can be broken down into two terms, one for carrier generation and one for carrier recombination

$$R_{n/p} = U_{n/p} - G_{n/p} \tag{2.63}$$

where G represents generation and U represents recombination for the respective charge carrier (negative recombination is equivalent to generation). Optical carrier generation was discussed in Section 2.2 and is a fixed input to the electrical model. Carrier recombination is the result of several different physical processes, which can be broken down into the two overarching categories of radiative and nonradiative recombination [60]. Radiative recombination is a fundamentally unavoidable recombination process required by the principle of detailed balance, which states that, at equilibrium, an elementary process must be balanced by its reverse process. [50]. For a semiconductor under bias, radiative recombination can be modeled as [50, 61]

$$U_{\text{rad}} = B_{\text{rad}}(np - \gamma_n \gamma_p n_{i,eff}^2) \tag{2.64}$$

where n and p are the concentration of electrons and holes, $n_{i,eff}$ is the instrinsic carrier concentration, and $B_{\rm rad}$ is the material dependent radiative recombination coefficient integrated over photon energy

$$B_{\rm rad} = \frac{1}{n_{i,eff}^2}\frac{1}{\pi\hbar^3c^2}\int_0^\infty n^2E^2\alpha(E)e^{\frac{E}{k_BT}}dE. \tag{2.65}$$

The radiative recombination rate in silicon is small compared to other recombination processes due to its indirect bandgap, with $B_{\rm rad}$ on the order of 10^{-15}cm^3/s [61, 62] at room temperature. Gallium arsenide is a direct band gap material, and therefore radiative recombination is more significant, with $B_{\rm rad}$ on the order of 10^{-10} cm^3/s [63, 64] at room temperature.

Auger recombination is a nonradiative recombination process caused by an interaction between two similar free charge carriers. This interaction causes one of the free carriers to recombine, and impart the energy of recombination to the other carrier. In an electron-electron interaction, one electron absorbs the energy and the other recombines with a hole while in a hole-hole interaction, one hole absorbs the energy and the other recombines with an electron [65]. The net recombination rate due to both processes is

$$U_{\rm Aug} = (C_pn + C_pp)(np - \gamma_n\gamma_pn_{i,eff}^2). \tag{2.66}$$

Auger recombination varies strongly with doping due to the squared dependence on carrier density. In highly doped semiconductors with large carrier densities and good crystal quality, Auger recombination is the primary recombination process.

Shockley-Read-Hall (SRH) recombination is another important recombination process [66] which, due to limitations on crystal quality, is the predominant recombination process in real solar cells. SRH recombination is caused by crystal defects which create localised trap states at energies within the band gap of semiconductor materials. These states can trap carriers and prevent them from being collected. If two charge carriers of opposite polarity are trapped by the same state, they recombine. The rate of recombination is given by

$$U_{\rm SRH} = \frac{np - \gamma_n\gamma_pn_{i,eff}^2}{\tau_{\rm n,SRH}(p+\gamma_pp_t) + \tau_{\rm p,SRH}(n+\gamma_nn_t)} \tag{2.67}$$

where $\tau_{\rm n/p,SRH}$ is the average amount of time an electron/hole will occupy the conduction/valence band before it is captured by the trap (i.e a trap lifetime) and

$$n_t = n_{i,eff}e^{\frac{E_t-E_i}{k_BT}} \tag{2.68}$$

$$p_t = n_{i,eff}e^{\frac{E_i-E_t}{k_BT}} \tag{2.69}$$

are the electron/hole densities when the electron/hole Fermi levels are equal to the trap energy level E_t. The trap lifetimes for electrons and holes in general depend on the electric field, temperature, and doping levels in the device. We neglect temperature and electric

field effects in our electrical model and only include the doping dependence, which is described by the empirical Scharfetter relation [67, 68]

$$\tau(N_A + N_D) = \tau_{\min} + \frac{\tau_{\max} - \tau_{\min}}{1 + \left(\frac{N_A+N_D}{N_{\text{ref}}}\right)^{\gamma}} \tag{2.70}$$

where

1. $\tau_{\min}$ is the minimum carrier lifetime
2. $\tau_{\max}$ is the maximum carrier lifetime
3. N_A is the concentration of ionized acceptor dopants
4. N_D is the concentration of ionized donor dopants
5. N_{ref} is the reference dopant concentration and is a fit parameter provided by Sentaurus.

The final recombination process included in the model is surface SRH recombination. On material surfaces, dangling bonds in the crystal lattice and adsorbed impurity molecules [65, 48, 69, 47, 70] lead to large concentrations of "surface states" within the band gap which serve as recombination centers for charge carriers. This recombination mechanism is especially relevant for nanowire solar cells due to their high surface-to-volume ratio. The surface recombination model is structurally equivalent to the bulk SRH recombination model, but is characterized by a single parameter called the "surface recombination velocity", using the formula

$$U_{\text{surf}} = \frac{np - \gamma_n \gamma_p n_{i,eff}^2}{(p + \gamma_p p_t)/s_n + (n + \gamma_n n_t)/s_p} \tag{2.71}$$

where $s_{n,p}$ is the surface recombination velocity of electrons/holes, and E_{trap} is the energy level of the trap.

2.3.4 Interface Transport

In the devices modeled here, a staggered isotype heterojunction exists at the interface between the GaAs nanowire and Si substrate. A heterojunction is an interface between two semiconductor materials of different band gaps. Isotype means the dopant types (p-type versus n-type) are the same on both sides of the interface (in this case both p-type). Staggered means the discontinuity in the band edges 'jumps" in the same direction for both the valence and conduction bands, with no overlap between the band edges on the energy axis (see Fig. 2.1). This difference in band gaps creates a discontinuity in the band edges (see Fig. 2.2), which affects carrier transport.

In order to accurately predict the device behavior of GaAs nanowires grown on silicon substrates, a thermionic emission model is used to compute the carrier transport across

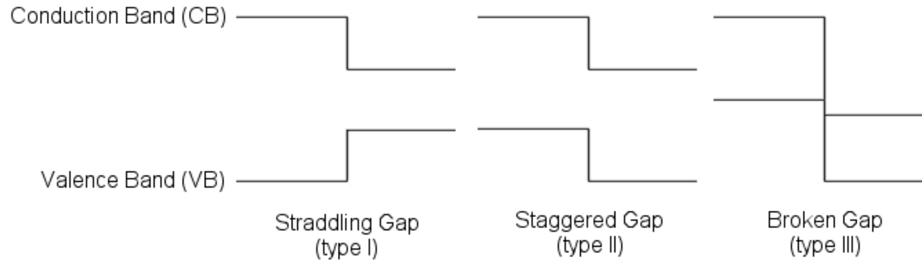

Figure 2.1: Classification of heterojunctions. (a) Type-I or straddling heterojunction. (b) Type-II or staggered heterojunction. (c) Type-III or broken-gap heterojunction. Adapted from [71], pg. 58.

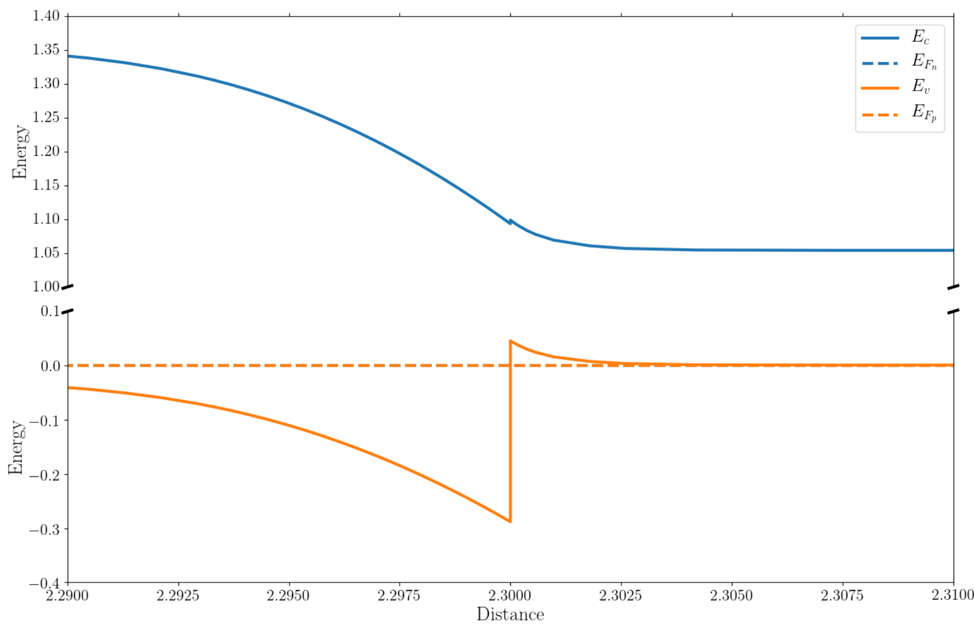

Figure 2.2: Example of band bending and discontinuities at a staggered isotype heterojunction. Note the Fermi energies are continuous, but the band edges have sharp discontinuities. Figured generated by Sentaurus at the GaAs-Si interface of the nanowire solar cell modeled in Ch. 6. The left hand side of the discontinuity contains p-type doped GaAs material, and the right hand side contains p-type doped Si, making the heterojunction an isotype heterojunction. The band gap of GaAs is 1.424 eV, whereas the band gap of Si is 1.17 eV. The band edges at the interface are staggered, as in the middle diagram of Fig. 2.1.

heterointerfaces [72]. Thermionic emission is the process by which charge carriers can pass over a potential energy barrier at the interface between two differing materials by means of their thermal kinetic energy. At a heterointerface between materials 1 and 2 with a positive conduction edge jump such that $\Delta E_C = E_{C,2} - E_{C,1}$, the current density $J_{n,2}$ leaving material 2 (using Fermi Dirac carrier statistics on both sides of the barrier) is

$$J_{n,2} = a_n q(v_{n,2} N_{C,2} \xi_{n,2} - \frac{m_{n,2}}{m_{n,1}} v_{n,1} N_{C,1} \xi_{n,1}) \tag{2.72}$$

$$\xi_{n,2} = \ln[1 + e^{-\eta_{n,2}}] + \eta_{n,2} \tag{2.73}$$

$$\xi_{n,1} = \ln[1 + e^{-\eta'_{n,1}}] + \eta'_{n,1} \tag{2.74}$$

$$\eta'_{n,1} = \eta_{n,1} - \frac{\Delta E_C}{kT} \tag{2.75}$$

where $m_{n/p,i}$ is the electron/hole effective mass in material i, $a_{n/p}$ is a material dependent integer coefficient, the thermal emission velocities $v_{n/p,i}$ are

$$v_{n/p,i} = \sqrt{\frac{kT}{2\pi m_{n/p,i}}} \tag{2.76}$$

and current continuity requires that $J_{n,2} = J_{n,1}$ [73]. As can be seen from the above equations, the phenomenon is heavily temperature dependent ([74], Section 3.3).

2.3.5 Doping Dependent Mobilities

In doped semiconductors, free carriers can scatter off charged impurity atoms, degrading the carrier mobility. To account for this effect, the empirical Arora model for doping dependent carrier mobilities built into Sentaurus is activated for both holes and electrons [75]. This model combines both temperature and doping dependence of the mobility into a single equation, and is built from a combination of theoretical models and fits to experimental data. The model (reparamaterized in Sentaurus for generality [53]) reads:

$$\mu_{\text{dop}} = \mu_{\text{min}} + \frac{\mu_d}{1 + \left(\frac{N_{A,0}+N_{D,0}}{N_0}\right)^{A^*}} \tag{2.77}$$

with

$$\mu_{\text{min}} = A_{\text{min}} \left(\frac{T}{300K}\right)^{\alpha_m} \tag{2.78}$$

$$\mu_d = A_d \left(\frac{T}{300K}\right)^{\alpha_d} \tag{2.79}$$

$$N_0 = A_N \left(\frac{T}{300K}\right)^{\alpha_N} \tag{2.80}$$

$$A^* = A_N \left(\frac{T}{300K}\right)^{\alpha_a} \tag{2.81}$$

where all the A and α are fit parameters that depend on material and carrier type. Table 2.1 contains values for GaAs and Si for both holes and electrons.

Symbol	Si Electrons	Si Holes	GaAs Electrons	GaAs Holes	Unit
A_{min}	88	54.3	2.14×10^3	21.48	$\mathrm{cm\,V^{-1}\,s^{-1}}$
α_m	-0.57	-0.57	-0.746	-1.12E+00	unitless
A_d	1252	407	6.33×10^3	3.31×10^2	$\mathrm{cm\,V^{-1}\,s^{-1}}$
α_d	-2.33	-2.23	-2.69	-2.37	unitless
A_N	1.25×10^{17}	2.35×10^{17}	7.35×10^16	5.14×10^17	$\mathrm{cm^{-3}}$
α_N	2.4	2.4	3.535	3.69	unitless
A_a	0.88	0.88	0.6273	0.8057	unitless
α_a	- 0.146	- 0.146	-0.144	0	unitless

Table 2.1: Parameters for the Arora doping dependent mobility model for both electrons and holes in GaAs and Si.

Chapter 3

Simulation Methods

3.1 Rigorous Coupled Wave Analysis

Rigorous Coupled Wave Analysis (RCWA, also referred to as the Fourier modal method), is a mathematical technique for modeling electromagnetic phenomenon with a surprisingly long and rich history. After the seminal paper pioneering the technique was published by Moharam and Gaylord in 1981 [76], a flurry of publications in the 1990's and early 2000's built upon their work to make the technique what it is today. During this time, several research groups made small, independent innovations that built directly upon the work of their peers. The interplay between these research groups (which is often directly called out in their publications) is an interesting and important part of RCWA's history. The powerful, diverse mathematical developments made by these researchers made it possible for RCWA to model general systems in an automated way, without requiring modifications to the implementation to suit a particular system of interest. To highlight this fascinating historical development, a derivation of a modern RCWA implementation is interwoven with historical anecdotes about who developed the various mathematical pieces of the theory below.

3.2 Maxwell's Equations and the Plane Wave Representation of the Fields

RCWA is a semi-analytic, frequency-domain method for solving Maxwell's equations

$$\nabla \times \mathbf{H} = -i\omega\epsilon\mathbf{E} + \mathbf{J}_f \tag{3.1}$$
$$\nabla \times \mathbf{E} = i\omega\mu\mathbf{H} \tag{3.2}$$
$$\nabla \cdot \mathbf{B} = 0 \tag{3.3}$$
$$\nabla \cdot \mathbf{D} = \rho_f. \tag{3.4}$$

By semi-analytic, here we mean that the technique does not require a full three dimensional discretization of real space (as in the finite element and finite difference methods) to approximate a solution to Maxwell's equations in continuous media. In their 1982 paper pioneering the technique, Moharam and Gaylord introduced the idea of decomposing systems into a set of discrete layers, wherein each layer's dielectric profile lacks any dependence on the coordinate orthogonal to the direction of periodicity [77]. This geometric simplification was motivated by their interest in diffraction gratings. Although in their paper they treat a diffraction grating with 1 dimensional periodicity, the technique is applicable to systems with 2 dimensional periodicity in the plane as well. We treat such systems here and define the unit cell of each layer using a set of real-space lattice vectors

$$\mathbf{L_{r,1}} = l_{1,x}\hat{\mathbf{x}} + l_{1,y}\hat{\mathbf{y}} \tag{3.5}$$

$$\mathbf{L_{r,2}} = l_{2,x}\hat{\mathbf{x}} + l_{2,y}\hat{\mathbf{y}}. \tag{3.6}$$

$$\tag{3.7}$$

These real-space lattice vectors come with an associated set of Fourier space reciprocal lattice vectors

$$\mathbf{L_{k,1}} = \frac{2\pi}{l_{1,x}l_{2,y} - l_{2,x}l_{1,y}}(l_{2,y}\hat{\mathbf{x}} - l_{2,x}\hat{\mathbf{y}}) \tag{3.8}$$

$$\mathbf{L_{k,2}} = \frac{2\pi}{l_{1,x}l_{2,y} - l_{2,x}l_{1,y}}(-l_{1,y}\hat{\mathbf{x}} - l_{1,x}\hat{\mathbf{y}}) \tag{3.9}$$

which define a point $\mathbf{G}$ in Fourier space according to $\mathbf{G} = m\,\mathbf{L_{k,1}} + n\,\mathbf{L_{k,2}}$ for some pair of integer m, n. Arbitrary dielectric profiles in the $x - y$ plane of the unit cell can be represented using their Fourier transform

$$\epsilon(\mathbf{r}) = \sum_{\mathbf{G}} \epsilon_{\mathbf{G}} e^{i\mathbf{G}\cdot\mathbf{r}} \tag{3.10}$$

where ϵ is the dielectric permittivity of the medium and $\mathbf{r} = x\,\hat{\mathbf{x}} + y\,\hat{\mathbf{y}}$. The Fourier coefficients $\epsilon_{\mathbf{G}}$ are defined according to

$$\epsilon_{\mathbf{G}} = \frac{1}{|L_r|}\int_{cell} \epsilon(\mathbf{r})e^{-i\mathbf{G}\cdot\mathbf{r}}d\mathbf{r} \tag{3.11}$$

where the integral is taken over the plane of the periodic unit cell. Devices with non-uniform ϵ along the z direction can be approximated as a "stack" of many layers with diminishing thickness (see Figure 3.1), although problems with this "staircase approximation" exist [78].

For the purposes of this derivation, we assume non-magnetic materials (as is the case for semiconductor materials used in solar cells) so that $\mu_r = 1$. We choose to use "natural" Lorentz Heaviside units where the speed of light $c = 1$ and the vacuum impedance $Z_0 = \sqrt{\frac{\epsilon_0}{\mu_0}} = 1$. This provides better numerical conditioning, bringing the electric and magnetic fields to the same order of magnitude. We assume no fixed charge or free current sources meaning $\rho_f = 0$ and $\mathbf{J}_f = 0$. Under these conditions, Maxwell's equations in Eq. (3.1)

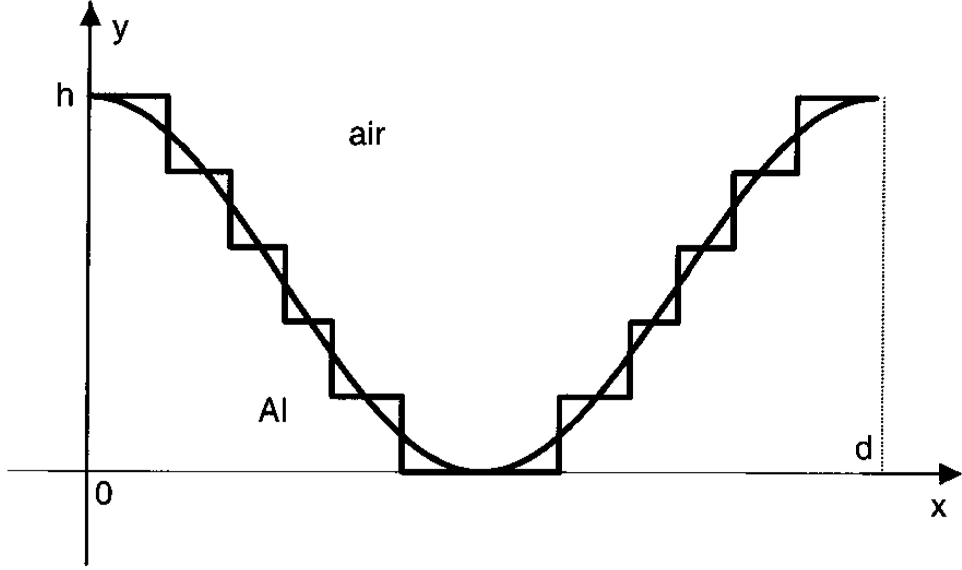

Figure 3.1: A staircase approximation to a continuously curved sinusoidal grating profile, reproduced from [78].

reduce to

$$\nabla \times \mathbf{H} = -i\omega\epsilon(\mathbf{r})\mathbf{E} \tag{3.12}$$

$$\nabla \times \mathbf{E} = i\omega\mathbf{H} \tag{3.13}$$

$$\nabla \cdot \mathbf{B} = 0 \tag{3.14}$$

$$\nabla \cdot \mathbf{D} = 0. \tag{3.15}$$

where here $\epsilon(\mathbf{r})$ can be interpreted as the relative permittivity of the material and has the Fourier representation shown in Eq. (3.11).

With this set of physical and geometric assumptions, the z-axis and the x-y plane become separable and we can represent all solutions to Maxwell's equations using a 2-D plane wave basis

$$\mathbf{H}(\mathbf{r}, z) = \sum_{\mathbf{G}} \mathbf{H}_{\mathbf{G}}(z) e^{i(\mathbf{k}+\mathbf{G})\cdot\mathbf{r}} \tag{3.16}$$

$$\mathbf{E}(\mathbf{r}, z) = \sum_{\mathbf{G}} \mathbf{E}_{\mathbf{G}}(z) e^{i(\mathbf{k}+\mathbf{G})\cdot\mathbf{r}} \tag{3.17}$$

where z is the longitudinal coordinate, $\mathbf{k} = k_x\hat{x} + k_y\hat{y}$ is the in-plane component of the wave vector of the excitation, and the $\mathbf{E}_{\mathbf{G}}(z) = [E_{\mathbf{G},x}(z), E_{\mathbf{G},y}(z), E_{\mathbf{G},z}(z)]^T$ and $\mathbf{H}_{\mathbf{G}}(z) = [H_{\mathbf{G},x}(z), H_{\mathbf{G},y}(z), H_{\mathbf{G},z}(z)]^T$ are z-dependent vector expansion coefficients. The plane-wave representation of the fields is at the core of RCWA, and is what makes it "semi-analytic".

We expand the curl equations of Eq. (3.12) into component form to get

$$\partial_y E_z - \partial_z E_y = i\omega H_x \tag{3.18}$$
$$\partial_z E_x - \partial_x E_z = i\omega H_y \tag{3.19}$$
$$\partial_x E_y - \partial_y E_x = i\omega H_z \tag{3.20}$$
$$\partial_y H_z - \partial_z H_y = -i\omega\epsilon E_x \tag{3.21}$$
$$\partial_z H_x - \partial_x H_z = -i\omega\epsilon E_y \tag{3.22}$$
$$\partial_x H_y - \partial_y H_x = -i\omega\epsilon E_z. \tag{3.23}$$

Picking Eq. 3.22 for illustrative purposes and inserting Eqs (3.32) and (3.10) we get

$$\begin{aligned} \sum_G i(k_x + G_x) H_{G,y}(z) e^{i(\mathbf{k}+\mathbf{G})\cdot\mathbf{r}} - \sum_G i(k_y + G_y) H_{G,x}(z) e^{i(\mathbf{k}+\mathbf{G})\cdot\mathbf{r}} \\ = \\ -i\omega \sum_{G\prime} \epsilon_{G'} e^{i\mathbf{G}'\cdot\mathbf{r}} \sum_G E_{G,z}(z) e^{i(\mathbf{k}+\mathbf{G})\cdot\mathbf{r}} \end{aligned} \tag{3.24}$$

and we are left with the problem of how to treat the product of two summations on the right hand side of the equation, which is to say how do we handle the product

$$D_x(\mathbf{r}, z) = \epsilon(\mathbf{r}, z) E_x(\mathbf{r}, z) \tag{3.25}$$

when both ϵ and E_x are expressed as a Fourier series. The dielectric permittivity is sharply discontinuous across material boundaries. At an interface where epsilon changes, the normal component of **E** and the tangential component of **D** are both discontinuous, while the tangential component of **E** and normal component of **D** are both continuous. Depending on the in-plane geometry of the system, the normal and tangential components may not lie in any Cartesian direction, implying that the Cartesian components of the fields may be discontinuous. Proper mathematical treatment of a product of discontinuous functions expressed as Fourier series leads us to a discussion of the "Fast Fourier Factorization" Rules.

3.3 Fast Fourier Factorization Rules

Until now, our calculations have assumed an infinite number of **G** and have thus been exact. In the case of infinite Fourier series, given some function $h(x) = f(x)g(x)$, Laurent's rule

$$h_{\mathbf{G}_n} = \sum_{\mathbf{G}_m} f_{\mathbf{G}_n - \mathbf{G}_m} g_{\mathbf{G}_m} \tag{3.26}$$

for the Fourier coefficients of h is always valid. Seeking a more compact notation, we can denote by $[f]$ the vector of Fourier coefficients for the function f and by $[\![f]\!]$ the Toeplitz matrix containing the Fourier coefficients of the function f whose entries are defined as

$f_{mn} = f_{n-m}$. Using this notation, Laurent's rule for all the Fourier coefficients of h can be succinctly expressed as

$$[h] = [\![f]\!] \, [g] \tag{3.27}$$

Any numerical implementation of RCWA must necessarily truncate these vectors and matrices to a finite size. For many years, researchers utilizing RCWA assumed Laurent's rule also held for *truncated* Fourier series, which is not the case! They based their RCWA implementations on this flawed assumption, and were puzzled by its poor convergence behavior for certain system geometries. In a critical 1996 paper, Li provided mathematical insight about how to treat truncated products of Fourier series that provided firm mathematical footing for convergence improvements to RCWA discovered empirically by Lalanne and Morris [79, 80]. In his paper, Li provides three simple rules for handling these products:

1. If $f(x)$ and $g(x)$ have no spatially concurrent jump discontinuities, then Laurent's rule (Eqs (3.26) and (3.27)) is valid for products of truncated Fourier series.

2. If $f(x)$ and $g(x)$ do have spatially concurrent jump discontinuities, but $h(x)$ is continuous, then the inverse Laurent's rule must be used

$$[h] = \left[\!\!\left[\frac{1}{f}\right]\!\!\right]^{-1} [g] \tag{3.28}$$

   where $\left[\!\!\left[\frac{1}{f}\right]\!\!\right]$ is taken to mean the Toeplitz matrix of the Fourier coefficients of the real space function $1/f$

3. If $f(x)$ and $g(x)$ have spatially concurrent jump discontinuities and $h(x)$ is discontinuous, there is no technique for computing the Fourier coefficients of $h(x)$.

The key now is to formulate RCWA in such a way that products of functions have either no concurrent jump discontinuities or only pairwise, complementary jump discontinuities for arbitrary in-plane $\epsilon(\mathbf{r})$. In 2000 and 2001, building upon the work of Li, Popov and Nevierre published what they dubbed the "Fast Fourier Factorization" rules which recast the underlying equations of RCWA to do exactly this [81, 82]. In essence, their formulation assumes the existence of a locally defined, spatially varying vector field $\mathbf{N}$ or $\mathbf{T}$ that is everywhere normal or tangential to all material interfaces in a given system (see Fig. 3.2). Given such a vector field, one can decompose the Cartesian components of the $\mathbf{E}$ and $\mathbf{D}$ fields into components normal and tangential to material interfaces and reconstruct the underlying differential equations to solve for these components. The tangential components of $\mathbf{E}$ are continuous, and the normal component of $\mathbf{D}$ is a continuous function composed of a product of two functions with pairwise, complementary jump discontinuities (ϵ and the normal components of $\mathbf{E}$). These quantities all satisfy the rules established by Li, and thus solve many of the convergence problems that previously plagued RCWA.

We restate here without derivation Popov and Nevierre's Fast Fourier Factorization rule for computing the Fourier components of D_x and D_y using the inverse Laurent's rule and

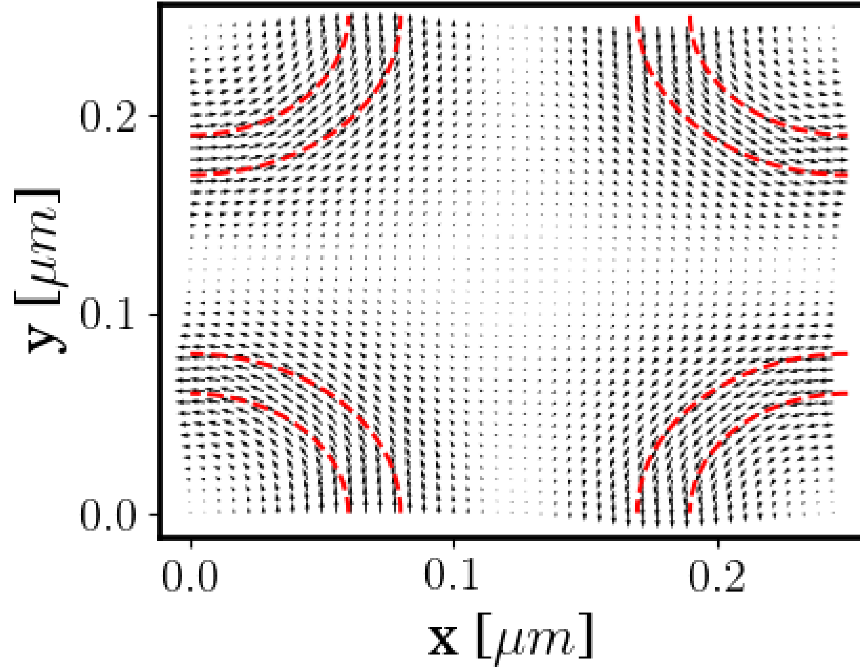

Figure 3.2: The spatially varying vector field tangential to material interfaces generated by S^4 for the optical modeling of a nanowire solar cell. This vector field provides a local coordinate system for describing physical electromagnetic fields. Since it is tangential to all material interfaces, it facilitates separating the tangential and normal components of the physical fields at all interfaces, while providing a smoothly varying coordinate system throughout the simulation cell. The solar cell has an array periodicity of 250 nm, with the figure containing the corner sections of 4 neighboring nanowires to demonstrate the periodicity of the vector field. The red dotted lines indicate the edges of the core and shell.

the normal vector field $\mathbf{N}$, simplified for the case of z-independent ϵ (for a full derivation, see Chapter IX of [83])

$$[D_x] = \{[\![\epsilon]\!] - \Delta[\![N_x^2]\!]\}[E_x] - \Delta[\![N_x N_y]\!][E_y] \tag{3.29}$$
$$[D_y] = \{[\![\epsilon]\!] - \Delta[\![N_y^2]\!]\}[E_y] - \Delta[\![N_x N_y]\!][E_x] \tag{3.30}$$

where $\Delta = [\![\epsilon]\!] - [\![1/\epsilon]\!]^{-1}$ and N_x, N_y are the x and y component, respectively, of the vector field normal to the material boundary [84]. Because we have assumed z-independent ϵ, E_z is always tangent to material boundaries, meaning it must be continuous at material boundaries and the product $\epsilon(\mathbf{r})E_z(\mathbf{r}, z)$ can be handled using Laurent's rule.

Popov and Nevierre presumed the existence of the vector field $\mathbf{N}$, however any practical implementation of RCWA requires some way of generating this vector field to capitalize on their mathematical improvements. A few papers published in the following years developed automated algorithms for generating $\mathbf{N}$ for arbitrary two dimensional dielectric profiles, making generic computer implementations of Popov and Nevierre's formulation possible [84, 85, 86]. An example vector field is shown in Figure 3.2. With the proper FFF rules in hand, we can now move on to calculate the eigenmodes of a single device layer.

3.4 Computing the Layer Eigenmodes

Next, we compute layer eigenmodes following the derivation of Ref. [86] and [87]. Because $\epsilon(\mathbf{r})$ is invariant along z, we can solve for the modes of each layer as propagating 2-D wave states with a simple plane wave e^{iqz} dependence (for some complex number q) along the z-direction. To do this, the z-dependent coefficients in Eq. (3.16) are expanded according to

$$\mathbf{H}_{\mathbf{G}}(z) = \left[\phi_x(\mathbf{G})\hat{\mathbf{x}} + \phi_y(\mathbf{G})\hat{\mathbf{y}} - \frac{(k_x + G_x)\phi_x(\mathbf{G}) + (k_y + G_y)\phi_y(\mathbf{G})}{q}\hat{\mathbf{z}}\right] e^{iqz}, \tag{3.31}$$

where the z-component has been chosen to satisfy the $\nabla \cdot \mathbf{H} = 0$ condition and the $\phi_{\mathbf{G}}$ are a set of $\mathbf{G}$-dependent expansion coefficients to be determined. The full $\mathbf{H}$ vector satisfies

$$\mathbf{H}(\mathbf{r}, z) = \sum_{\mathbf{G}} \left[\phi_x(\mathbf{G})\hat{\mathbf{x}} + \phi_y(\mathbf{G})\hat{\mathbf{y}} - \frac{(k_x + G_x)\phi_x(\mathbf{G}) + (k_y + G_y)\phi_y(\mathbf{G})}{q}\hat{\mathbf{z}}\right] e^{i(\mathbf{k}+\mathbf{G})\cdot\mathbf{r}+iqz}. \tag{3.32}$$

Transitioning to a more compact notation, we use N_G to denote the number of $\mathbf{G}$ retained in the computation and let

1. $\phi_x = [\phi_x(\mathbf{G}_1), \phi_x(\mathbf{G}_2), ...]^T$ be the column vector of coefficients $\phi_x(\mathbf{G})$, length N_G.
2. $\phi_y = [\phi_y(\mathbf{G}_1), \phi_y(\mathbf{G}_2), ...]^T$ be the column vector of coefficients $\phi_y(\mathbf{G})$, length N_G.

3. $\hat{k_x}$ be the diagonal matrix of size $N_G \times N_G$ with elements $(\hat{k_x})_{\mathbf{GG}} = (k_x + G_x)$, with an analogous definition for $\hat{k_y}$.

4. $\hat{\epsilon} = [\![\epsilon]\!]$, size $N_G \times N_G$

5. $\eta = \frac{1}{\epsilon}$ and $\hat{\eta} = [\![1/\epsilon]\!]$, size $N_G \times N_G$

6. $h_x(z)$ be the column vector containing the x-component of $\mathbf{H_G}(z)$ for each $\mathbf{G}$, with similar definitions for the remaining components of $\mathbf{H_G}$, $\mathbf{E_G}$, and $\mathbf{D_G}$. All of size N_G.

Using this notation and the form of the fields in Eqs. (3.16) and (3.17), we can utilize the orthogonality of plane waves (see Appendix A) to rewrite Eqs. (3.18) - (3.23) as a system of equations for the Fourier coefficients of $\mathbf{H}$, $\mathbf{E}$, and $\mathbf{D}$, where $\partial_x \to i\hat{k_x}$, $\partial_y \to i\hat{k_y}$, and we substitute $\epsilon E_x \to D_x$ and $\epsilon E_y \to D_y$ in anticipation of the FFF rules

$$i\hat{k_y} e_z - \partial_z e_y = i\omega h_x \tag{3.33}$$
$$\partial_z e_x - i\hat{k_x} e_z = i\omega h_y \tag{3.34}$$
$$i\hat{k_x} e_y - i\hat{k_y} e_x = i\omega h_z \tag{3.35}$$
$$i\hat{k_y} h_z - \partial_z h_y = -i\omega d_x \tag{3.36}$$
$$\partial_z h_x - i\hat{k_x} h_z = -i\omega d_y \tag{3.37}$$
$$i\hat{k_x} h_y - i\hat{k_y} h_x = -i\omega \hat{\epsilon} e_z \tag{3.38}$$

Rearranging Eqs. (3.35) and (3.38) to isolate the z-components we get

$$e_z = \frac{\hat{\epsilon}^{-1}}{\omega}(\hat{k_y} h_x - \hat{k_x} h_y) \tag{3.39}$$
$$h_z = \frac{1}{\omega}(\hat{k_y} e_x - \hat{k_x} e_y) \tag{3.40}$$

Next, we insert Eq. (3.39) into Eqs (3.33) & (3.34) and Eq. (3.40) into Eqs. (3.36) & (3.37) to get

$$\omega^2 d_x = \hat{k_y}\hat{k_y} e_x - \hat{k_y}\hat{k_x} e_y - i\omega\partial_z h_y \tag{3.41}$$
$$\omega^2 d_y = i\omega\partial_z h_x + \hat{k_x}\hat{k_y} e_x - \hat{k_x}\hat{k_x} e_y \tag{3.42}$$
$$\omega^2 h_x = i\omega\partial_z e_y + (\hat{k_y}\hat{\epsilon}^{-1}\hat{k_y} h_x - \hat{k_y}\hat{\epsilon}^{-1}\hat{k_x} h_y) \tag{3.43}$$
$$\omega^2 h_y = (\hat{k_x}\hat{\epsilon}^{-1}\hat{k_x} h_y - \hat{k_x}\hat{\epsilon}^{-1}\hat{k_y} h_x) - i\omega\partial_z e_x \tag{3.44}$$

which, after defining the matrices

$$K = \begin{bmatrix} \hat{k_x}\hat{k_x} & \hat{k_x}\hat{k_y} \\ \hat{k_y}\hat{k_x} & \hat{k_y}\hat{k_y} \end{bmatrix} \tag{3.45}$$

$$\mathcal{K} = \begin{bmatrix} \hat{k_y}\hat{\epsilon}^{-1}\hat{k_y} & -\hat{k_y}\hat{\epsilon}^{-1}\hat{k_x} \\ -\hat{k_x}\hat{\epsilon}^{-1}\hat{k_y} & \hat{k_x}\hat{\epsilon}^{-1}\hat{k_x} \end{bmatrix} \tag{3.46}$$

can be written as

$$\omega^2 \begin{bmatrix} -d_y \\ d_x \end{bmatrix} = K \begin{bmatrix} -e_y \\ e_x \end{bmatrix} - i\omega \begin{bmatrix} \partial_z h_x \\ \partial_z h_y \end{bmatrix} \tag{3.47}$$

$$(\omega^2 I - \mathcal{K}) \begin{bmatrix} h_x \\ h_y \end{bmatrix} = -i\omega \begin{bmatrix} -\partial_z e_y \\ \partial_z e_x \end{bmatrix} \tag{3.48}$$

The FFF rules in Eqs. (3.29) and (3.30), when cast into the matrix form using our current notation, become

$$\begin{bmatrix} -d_y \\ d_x \end{bmatrix} = \hat{P} \begin{bmatrix} -e_y \\ e_x \end{bmatrix} \tag{3.49}$$

where

$$\hat{P} = \begin{bmatrix} \hat{\epsilon} - \widehat{\Delta N_x^2} & \Delta \widehat{N_x N_y} \\ \Delta \widehat{N_x N_y} & \hat{\epsilon} - \widehat{\Delta N_x^2} \end{bmatrix}. \tag{3.50}$$

Noting that the Fourier coefficients $\mathbf{E}_G$ must have the same e^{iqz} dependence as $\mathbf{H_G}$, we can insert the components of $\mathbf{H_G}$ shown in Eq. (3.31) and Eq. (3.49) into Eqs. (3.47) & (3.48) to get

$$(\omega^2 \hat{P} - K) \begin{bmatrix} -e_y \\ e_x \end{bmatrix} = \omega q \begin{bmatrix} \phi_x \\ \phi_y \end{bmatrix} \tag{3.51}$$

$$(\omega^2 I - \mathcal{K}) \begin{bmatrix} \phi_x \\ \phi_y \end{bmatrix} = \omega q \begin{bmatrix} -e_y \\ e_x \end{bmatrix} \tag{3.52}$$

which when eliminating the Fourier components of $\mathbf{E}$ and noting $K\mathcal{K} = 0$ finally gives

$$(\hat{P}(\omega^2 - \mathcal{K}) - K) \begin{bmatrix} \phi_x \\ \phi_y \end{bmatrix} = q^2 \begin{bmatrix} \phi_x \\ \phi_y \end{bmatrix} \tag{3.53}$$

Eq. (3.53) is an eigenvalue equation in $\mathbf{A} \cdot \mathbf{x} = \lambda \mathbf{x}$ form where

$$\mathbf{A} = (\hat{P}(\omega^2 - \mathcal{K}) - K) \tag{3.54}$$

$$\mathbf{x} = \begin{bmatrix} \phi_x \\ \phi_y \end{bmatrix} \tag{3.55}$$

$$\lambda = q^2 \tag{3.56}$$

which can be solved for the eigenvalues q and the components of the eigenvectors ϕ_x, ϕ_y using standard numerical algorithms for solving eigenvalue problems. S^4 utilizes the QR algorithm for finding the eigenvalues and eigenvectors of the matrix $\mathbf{A}$ [88].

3.5 Electric and Magnetic Fields

The solution of the eigenvalue equation (3.53) provides a set of eigenmodes for the layer. These eigenmodes can be used to expand the Fourier coefficients of the field $\mathbf{H}$ according

to

$$\begin{bmatrix} h_x \\ h_y \end{bmatrix} = \sum_n \begin{bmatrix} \phi_{x,n} \\ \phi_{y,n} \end{bmatrix} (a_n e^{iq_n z} + b_n e^{iq_n (d_i - z)}) \tag{3.57}$$

where the a_n, b_n are unknown coefficients of forward and backward propagating modes, respectively, that must be determined from the boundary conditions at the top and bottom of the layer and d_i is the thickness of the ith layer [89, 90]. The Fourier coefficients of the **E** field can be obtained by combining Eqs (3.57) and (3.52) to get

$$\begin{bmatrix} -e_y \\ e_x \end{bmatrix} = \sum_n (\omega^2 I - \mathcal{K}) \begin{bmatrix} \phi_{x,n} \\ \phi_{y,n} \end{bmatrix} \frac{a_n e^{iq_n z} + b_n e^{iq_n (d_i - z)}}{\omega q} \tag{3.58}$$

We can cast Eqs. (3.57) and (3.58) into a compact matrix form by defining

1. $\hat{f}(z)$ to be the diagonal matrix operator with $e^{iq_n z}$ on the diagonal, of size N_G x N_G.
2. $\hat{q}$ to be the diagonal matrix operator with q_n on the diagonal, of size N_G x N_G.
3. Φ to be the matrix whose columns are the eigenvectors ϕ_n.
4. a and b to be the column vectors $[a_1, a_2, a_3 \cdots]^T$ and $[b_1, b_2, b_3 \ldots]^T$, both of length N_G.

to get

$$\begin{bmatrix} -e_y \\ e_x \\ h_x \\ h_y \end{bmatrix} = \begin{bmatrix} (\omega^2 - \mathcal{K})\Phi\omega^{-1}\hat{q}^{-1} & -(\omega^2 - \mathcal{K})\Phi\omega^{-1}\hat{q}^{-1} \\ \Phi & \Phi \end{bmatrix} \begin{bmatrix} \hat{f}(z)a \\ \hat{f}(d-z)b \end{bmatrix} \tag{3.59}$$

$$= M \begin{bmatrix} \hat{f}(z)a \\ \hat{f}(d-z)b \end{bmatrix} \tag{3.60}$$

3.6 Scattering Matrix Method

All of the mathematical components described thus far have allowed us to solve Maxwell's equations in a single layer with one, fixed dielectric profile for the electromagnetic modes of that layer. The final piece of this puzzle is to introduce a method for joining the single layer modal solutions from multiple layers together so we may propagate an incident plane wave excitation through a realistic multi-layer device (like a solar cell). A class of recursive matrix algorithms exists for solving exactly this problem. Among them are the Transfer Matrix Method, Enhanced Transmittance Matrix Method, R-Matrix method, and the scattering matrix (S-Matrix) Method [79, 91, 92]. While conceptually it makes sense to introduce these matrix algorithms after discussing the Fast Fourier Factorization rules, they were actually incorporated into RCWA long before the innovations of Popov and Nevierre as early as 1988 [92, 91, 87, 93]. Among the matrix algorithms, the S-matrix

method has won out as the de-facto standard algorithm for RCWA implementations due to it's simplicity and numerical stability when modeling many-layered structures with thick layers [78].

The Scattering Matrix (S-Matrix) relates the forward and backward propagating amplitudes in Eqs (3.58) and (3.57) in two arbitrary layers of the device

$$\begin{bmatrix} a_l \\ b_{l'} \end{bmatrix} = S(l, l') \begin{bmatrix} a_{l'} \\ b_l \end{bmatrix} = \begin{bmatrix} S_{11} & S_{12} \\ S_{21} & S_{22} \end{bmatrix} \begin{bmatrix} a_{l'} \\ b_l \end{bmatrix} \tag{3.61}$$

where l has been used to index layers. The amplitudes in two adjacent layers of the device are related by the interface matrix

$$\begin{bmatrix} \hat{f}_l(d_l) a_l \\ b_l \end{bmatrix} = I(l, l+1) \begin{bmatrix} a_{l+1} \\ \hat{f}_{l+1}(d_{l+1}) b_{l+1} \end{bmatrix} = \begin{bmatrix} I_{11} & I_{12} \\ I_{21} & I_{22} \end{bmatrix} \begin{bmatrix} a_{l+1} \\ \hat{f}_{l+1}(d_{l+1}) b_{l+1} \end{bmatrix} \tag{3.62}$$

where $\hat{f}_l = \hat{f}(d_l)$. The interface matrix can be obtained by requiring continuity of the components of the fields tangential to the interface (i.e the in-plane components E_x, E_y, H_x, and H_y). Looking to Eq. (3.60) we have the equality

$$M_l \begin{bmatrix} \hat{f}_l(d_l) a_l \\ b_l \end{bmatrix} = M_{l+1} \begin{bmatrix} a_{l+1} \\ \hat{f}_{l+1}(d_{l+1}) b_{l+1} \end{bmatrix} \tag{3.63}$$

from which we can see that

$$I(l, l+1) = M_l^{-1} M_{l+1} \tag{3.64}$$

With the interface matrix in hand, our goal is to construct the scattering matrix relating the coefficients in some layer l to the next layer $l+1$

$$\begin{bmatrix} a_{l+1} \\ b_l \end{bmatrix} = S(l, l+1) \begin{bmatrix} a_l \\ b_{l+1} \end{bmatrix}. \tag{3.65}$$

Once we have computed $S(l, l+1)$, we can start from the known coefficients of an excitation and compute the coefficients in layer $l = 1$ using the scattering matrix $S(0, 1)$. This technique can be applied successively to obtain $S(0, N)$, the scattering matrix for the entire structure. Expanding Eqs. (3.61) and (3.62) gives

$$a_l = S_{11}(l', l) a_{l'} + S_{12}(l', l) b_l \tag{3.66}$$

$$b_{l'} = S_{21}(l', l) a_{l'} + S_{22}(l', l) b_l \tag{3.67}$$

$$\hat{f}_l a_l = I_{11}(l, l+1) a_{l+1} + I_{12}(l, l+1) \hat{f}_{l+1} b_{l+1} \tag{3.68}$$

$$b_l = I_{21}(l, l+1) a_{l+1} + I_{22}(l, l+1) \hat{f}_{l+1} b_{l+1} \tag{3.69}$$

By inserting Eqs. (3.68) and (3.69) into (3.66) and (3.67) we can eliminate a_l and b_l to retrieve the elements of the matrix $S(l', l+1)$, which can be identified from the coefficients

of the $a_{l'}$ and b_{l+1} terms after performing this substitution. These terms are

$$\begin{aligned} S_{11}(l', l+1) &= \left(I_{11} - \hat{f}_l S_{12}(l', l) I_{21}\right)^{-1} \hat{f}_l S_{11}(l', l) \\ S_{12}(l', l+1) &= \left(I_{11} - \hat{f}_l S_{12}(l', l) I_{21}\right)^{-1} \\ &\times \left(\hat{f}_l S_{12}(l', l) I_{22} - I_{12}\right) \hat{f}_{l+1} \\ S_{21}(l', l+1) &= S_{22}(l', l) I_{21} S_{11}(l', l+1) + S_{21}(l', l) \\ S_{22}(l', l+1) &= S_{22}(l', l) I_{21} S_{12}(l', l+1) + S_{22}(l', l) I_{22} \hat{f}_{l+1} \end{aligned} \tag{3.70}$$

which, when letting $l' \to l$ and noting $S(l,l) = 1$, yields the components of the desired matrix $S(l, l+1)$. Computing the fields requires knowledge of a_l and b_l, which are obtained by calculating $S(0,l)$ and $S(l,N)$ using the above recipe (where N labels the bottom layer of the device). The coefficients in some layer l are

$$\begin{aligned} a_l &= [1 - S_{12}(0,l) S_{21}(l,N)]^{-1} \\ &\times [S_{11}(0,l) a_0 + S_{12}(0,l) S_{22}(l,N) b_N] \\ b_l &= [1 - S_{21}(l,N) S_{12}(0,l)]^{-1} \\ &\times [S_{21}(l,N) S_{11}(0,l) a_0 + S_{22}(l,N) b_N] \end{aligned} \tag{3.71}$$

Chapter 4

Verification of RCWA

This chapter exists as a journal article in [94], and is reproduced with permission here.

4.1 Introduction

Nanowire solar cells (NWSC) are a new solar cell technology with the potential to improve upon existing solar cell devices. Their potential stems from their ability to effectively absorb incident light while using less semiconductor material than planar solar cells.

The optimal nanowire solar cell arrays consists of nanowires that are a few microns in height and with diameters and periodicities comparable to the wavelengths present in the solar spectrum [9, 8]. These small sizes require full wave optics simulations to accurately model their optical properties, unlike in standard planar devices [7, 95]. Both experimental measurements and modeling have shown high levels of absorption with low sensitivity to the incident angle of light [6]. Additionally, the finite in-plane dimensions of nanowires can accommodate strain due to growth on lattice-mismatched substrates without introducing dislocation faults in the crystal lattice [20]. This capability opens up the possibility for high-efficiency III-V tandem cells grown on silicon [22].

The larger design parameter space of NWSC relative to planar solar cells requires careful optimization of geometric parameters to maximize device performance [96]. There is a need for fast, accurate modeling tools to enable rapid exploration and optimization of nanowire designs. Conventionally, finite element [16, 95, 12, 48] and finite difference methods [9, 11, 97] have been used in optical models of NWSC. While these techniques are highly accurate, they are computationally expensive, limiting their usefulness in a closed-loop global device optimization. Rigorous coupled wave analysis (RCWA) is another wave-optics modeling technique that lacks the memory and computational requirements of competing techniques [98]. RCWA is a Fourier domain technique ideally suited to periodic arrays. It is promising for its speed and is highly accurate when computing far-field quantities such as total absorptance, reflectance, and transmittance. RCWA simulations become more accurate as the number of plane waves N_G increases, and the computational cost scales as N_G^3. However, naive implementations lack accuracy at reasonable N_G when

computing near-fields internal to the device due to the well-known Gibbs phenomenon [99]. Such near-fields are required to compute carrier generation rates and are thus an essential component of a fully-coupled optoelectronic device model.

In this work, we show that RCWA can be used for accurate optical modeling of nanowire solar cells. We examine a test device (see Fig. 4.1 and Table 4.1), indicate where standard RCWA formulations lack sufficient accuracy, and provide two techniques for increasing accuracy of the near fields. The first is an implementation of an already published technique for introducing proper discontinuities in the near fields and mitigating the Gibbs phenomenon [100, 101, 99, 102]. We extend the open source RCWA library S^4 to include this technique, and show it greatly increases the accuracy of local field computations [86]. The second is a new rescaling technique that increases the accuracy of device simulations while keeping computational cost reasonable when computing spectrally integrated quantities. We show that even with our two improvements, some spectrally resolved quantities continue to require more expensive calculations. Using our improvements, RCWA shows promise as an effective technique for rapid optical modeling of nanowire solar cells.

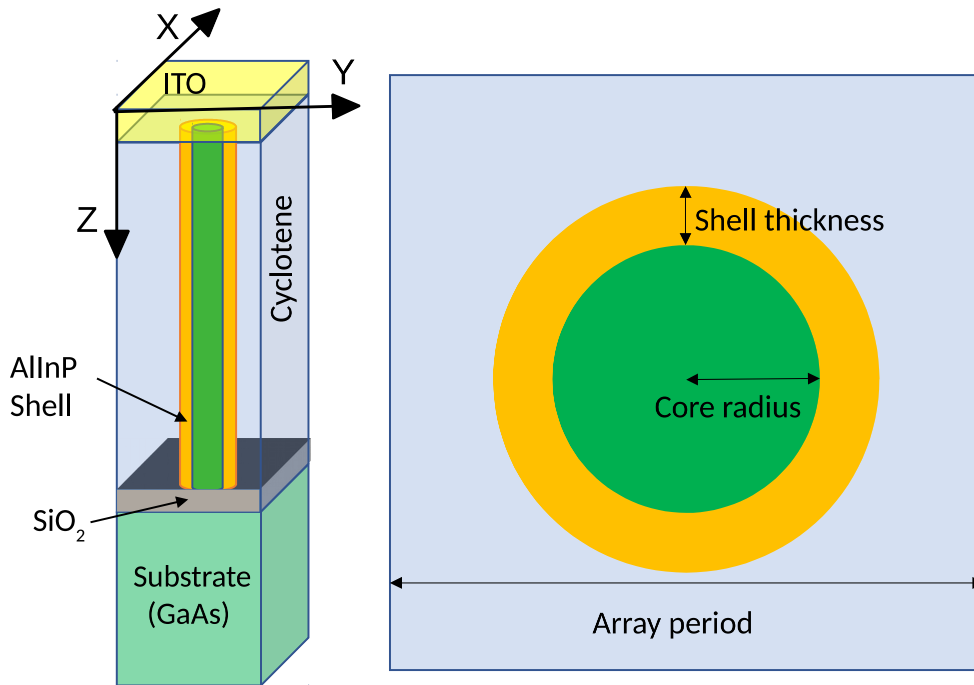

Figure 4.1: The test device used for assessment of RCWA. Left: A single unit cell in a square nanowire array containing a cylindrical GasAs nanowire passivated by an AlInP shell on a GaAs substrate, planarized by a cyclotene dielectric, and top-contacted with a layer of indium tin oxide. A thin layer of SiO_2, surrounding the GaAs core but lacking the AlInP shell, exists between the cyclotene and substrate. Right: A top down view of the unit cell, demonstrating the piecewise constant material parameters in the plane.

Table 4.1: Numerical values for all geometric parameters in the test device.

Parameter	Value
NW Core Length	1.3 μm
NW Shell Length	1.27 μm
SiO_2 Thickness	30 nm
Substrate Thickness	1 μm
ITO Thickness	300 nm
Array Period	250 nm
Core Radius	60 nm
Shell Thickness	20 nm

4.2 RCWA

RCWA is a Fourier-space method for solving the frequency domain Maxwell's equations with frequency ω:

$$\nabla \times \mathbf{H} = -i\omega\epsilon\mathbf{E} + \mathbf{J}_f \tag{4.1}$$

$$\nabla \times \mathbf{E} = i\omega\mu\mathbf{H} \tag{4.2}$$

$$\nabla \cdot \mathbf{B} = 0 \tag{4.3}$$

$$\nabla \cdot \mathbf{D} = \rho_f \tag{4.4}$$

where $\mathbf{B} = \mu\mathbf{H}$ is the magnetic field, $\mathbf{E}$ is the electric field, $\mathbf{D} = \epsilon\mathbf{E}$ is the displacement field, ϵ is the electric permitivitty, μ is the magnetic permeability, $\mathbf{J}_f$ is the free current density, and ρ_f is the free charge density. RCWA relies on two critical assumptions about the geometry of the system. First, the device must be composed of discrete, axially-invariant layers such that at a given x-y point within a layer, the material parameters along the z-direction remain constant. Second, the device must be decomposable into fundamental unit cells that are 2D periodic in the plane. If these conditions are satisfied, then the longitudinal and transverse dimensions are separable and the fields in a single layer can be written as:

$$\mathbf{H}(\mathbf{r}, z) = \sum_{\mathbf{G}} \mathbf{H}_{\mathbf{G}}(z) e^{i(\mathbf{k}+\mathbf{G})\cdot\mathbf{r}}, \tag{4.5}$$

where $\mathbf{G}$ is one of N_G in-plane reciprocal lattice vectors, $\mathbf{k}$ is the in-plane component of the excitation wave vector, and $\mathbf{r} = x\hat{\mathbf{x}} + y\hat{\mathbf{y}}$. Note the $\mathbf{G}$ is generally chosen to be an array of reciprocal lattice points with a circular truncation, keeping all $\mathbf{G}$ with $|\mathbf{G}|$ less than some constant, which maintains symmetry in Fourier space [86]. The in-plane dielectric profile $\epsilon(\mathbf{r})$ may depend on the material, allowing it to have piecewise-constant dependence on the transverse spatial coordinates. Vertical nanowire arrays (see Fig. 4.1) satisfy these geometric constraints.

We consider only non-magnetic materials, so $\mu = \mu_0$, the vacuum permeability. At optical frequencies, which we consider, ρ_f is negligible. $\mathbf{J}_f$ can be used to describe emission

from within structures; we will not make such considerations and will thus consider $\mathbf{J}_f = 0$ in the examples below, but such currents could be added without difficulty.

The approximation of step changes in ϵ, while convenient mathematically, is known to produce singularities in local fields and their gradients at internal corners and edges [103]. These singularities are square integrable, as is required for conservation of energy, but are generally not fully resolvable with standard FDTD, FEM, and RCWA methods, though specialized methods have been proposed to treat some of the singularities in particular geometries [104, 105, 106]. The cylindrical geometry considered here contains no corners and the active region of GaAs is convex, so the field singularities inside the nanowire material are relatively benign, but they are not accurately modeled here. Instead, we effectively spread the associated optical generation over a region given by the Fourier resolution, which scales as the unit cell period divided by $\sqrt{N_G}$. Since this length scale is smaller than material diffusion lengths, we do not anticipate effects in device modeling.

The essential part of RCWA is determining $\mathbf{H}_{\mathbf{G}}(z)$ in Eq. (4.5) for a given set of reciprocal lattice vectors $\mathbf{G}$. One can assume the coefficients in Eq. (4.5) take the form [86]

$$\mathbf{H}_{\mathbf{G}}(z) = \left[\phi_{\mathbf{G},x}\hat{\mathbf{x}} + \phi_{\mathbf{G},y}\hat{\mathbf{y}} - \frac{(k_x + G_x)\phi_{\mathbf{G},x} + (k_y + G_y)\phi_{\mathbf{G},y}}{q}\hat{\mathbf{z}} \right] e^{iqz}, \tag{4.6}$$

where the ϕ are expansion coefficients and the z-component has been chosen to satisfy the $\nabla \cdot \mathbf{H} = 0$ condition. This form of the fields illustrates one of the key advantages of RCWA over competing techniques, namely the analytic dependence on the z coordinate. By inserting Eq. (4.6) into Eq. (4.1), one arrives at an eigenvalue equation for determining the set of eigenvalues q and the components of the eigenvectors ϕ for a single layer. Once the eigenmodes of each layer have been determined, multilayer structures are joined together by introducing propagation amplitudes for the eigenmodes and using the scattering matrix method to join solutions at layer interfaces [79, 87, 107, 108, 109]. Results increase in accuracy with N_G. Our work is an extension to S^4, an open-source implementation of RCWA built on the scattering matrix method [86]. In the remainder of the manuscript, we refer to S^4 as the standard RCWA method, but it has included a significant number of improvements from the original RCWA methods; for details, see [86].

For optoelectronic device modeling, we are most concerned with determining the local carrier generation rate, which is determined from the local electric field strength in each material. RCWA expresses the fields using the Fourier series in Eq. (4.5). Any finite Fourier series representation is always continuous, even across in-plane material interfaces, as between the core and shell of a nanowire. In an exact solution, the normal components of $\mathbf{E}$ should be discontinuous across material boundaries, but a Fourier reconstruction requires an intractable number of terms to accurately model such a discontinuity, even though far-field quantities such as the total absorptance may be well converged. For any finite N_G, standard RCWA-produced fields have spurious oscillations, especially near material interfaces.

To assess the convergence of RCWA with N_G, we define two methods for computing the absorptance of a layer of the device. The first method relies only on the power passing

through the top and bottom of the layer. These powers can be computed entirely in Fourier space [86], and do not suffer from convergence issues in the reconstruction of the near fields. The net emitted powers of layer i are defined as:

$$P^i_{\text{up}}(\omega) = \int_{\text{top}} S_z(\omega) dA \tag{4.7}$$

$$P^i_{\text{down}}(\omega) = \int_{\text{bottom}} S_z(\omega) dA, \tag{4.8}$$

where S_z is the z-component of the Poynting vector and the integration is over the top or bottom surface of the unit cell, with the appropriate sign for emitted power. Considering the top (layer 1) and bottom (layer n) together, the total reflectance and transmittance are

$$R(\omega) = \frac{P^1_{\text{up}}(\omega)}{P_{\text{in}}(\omega)} \tag{4.9}$$

$$T(\omega) = \frac{P^n_{\text{down}}(\omega)}{P_{\text{in}}(\omega)}, \tag{4.10}$$

where P_{in} is the input power of the incident plane wave. Then total absorptance is:

$$A_{\text{far field}}(\omega) = 1 - R(\omega) - T(\omega). \tag{4.11}$$

The contribution of a single layer to the device absorptance can be calculated similarly. We consider the test structure detailed in Table 4.1 and use S^4 [86] to perform RCWA calculations with normally-incident circularly polarized light. Due to the circular symmetry of the nanowires, total absorption is independent of the handedness of the incident light, so we can consider just one polarization and determine the local field strengths even for incoherent illumination [48]. We consider 60 equally spaced frequencies corresponding to wavelengths from 300 nm to 900 nm, just beyond the GaAs absorption edge of 871 nm. Figure 4.2 shows that the far-field absorptance spectrum of the full device converges rapidly with basis terms, and is self-converged within 0.5% with $N_G = 75$.

Equation (4.11) expresses the power absorbed in a layer in terms of the fluxes into and out of the layer. The divergence theorem and Maxwell's equations allow rewriting that power in terms of the local fields, instead. The absorbed power can then be written,

$$\mathcal{P}_{\text{abs}}(\omega) = \epsilon_0 \omega \int n(x, y, z; \omega) k(x, y, z; \omega) |E(x, y, z; \omega)|^2 dV \tag{4.12}$$

$$A_{\text{near field}} = \frac{\mathcal{P}_{\text{abs}}}{P_{\text{in}}}. \tag{4.13}$$

The complex dielectric at each frequency is constructed from tabulated real n and imagi-

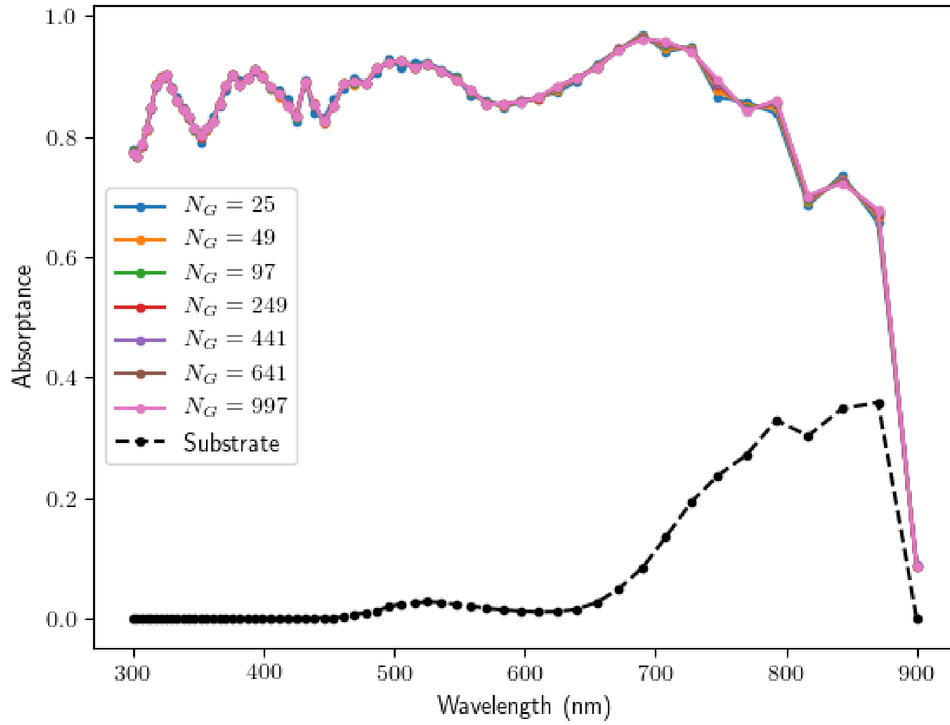

Figure 4.2: Absorptance of the entire device calculated using the far field fluxes, Eqs. (4.7) - (4.11). The markers for all values of N_G lie nearly on top of one another, indicating convergence at low numbers of basis terms. The dashed black line shows the portion of the absorptance that occurs in the GaAs substrate (calculated with $N_G = 997$), which is negligible at shorter wavelengths, becoming more significant at longer wavelengths.

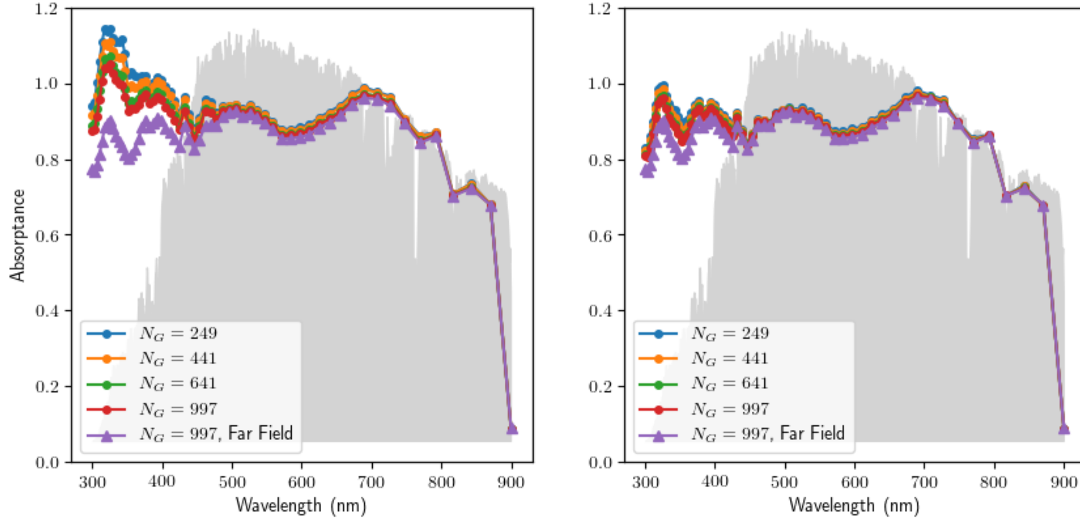

Figure 4.3: Absorptance calculated from near fields using Eqs. (4.12) - (4.13) (circles). Far field absorptance at $N_G = 997$ (triangles). a) S^4 implementation of RCWA. b) Continuous variable formulation. Gray background shows the AM1.5 solar spectrum. The CVF shows significant improvement, especially at short wavelengths.

nary k parts of the index of refraction in each material [110, 16].

We calculate $A_{\text{near field}}$ by extracting $\mathbf{E}(\mathbf{r})$ on a cubic mesh with 1 nm spacing in the plane for all layers. We use 3 nm spacing along the z-direction in the ITO layer and 3.5 nm spacing in the nanowire layer. A sparser mesh of 16 nm spacing is used in the substrate due to the weak absorption there. This choice of mesh is sufficiently dense to converge the result better than 1% using a simple trapezoidal rule integration. Figure 4.3(a) shows the convergence of $A_{\text{near field}}$ with N_G. Though the near fields are well converged for $\lambda > 450$ nm, they are not converged at short wavelengths even for $N_G = 997$.

Figure 4.4 shows some results of Figs. 4.2 and 4.3 as a function of N_G at three wavelengths and spectrally integrated with the AM1.5G solar spectrum [111], to more clearly show that the far-field method (green line) converges rapidly at all wavelengths, while the standard local-field method (blue line) only converges to the far-field result for long wavelength.

In the following sections, we provide two techniques for improving the accuracy of the near fields in RCWA. The first is an implementation of an existing technique, which we call the continuous variable formulation (CVF), which mitigates the Gibbs phenomenon and ensures proper discontinuities at interfaces by modifying the field computations such that only quantities that are continuous in real space are reconstructed from their Fourier components [99]. The discontinuities across in-plane material boundaries are then handled in real space. The second technique uses the well-converged, highly accurate far-field computation of each layer's absorption to rescale the near fields, ensuring correct total generation within a device layer.

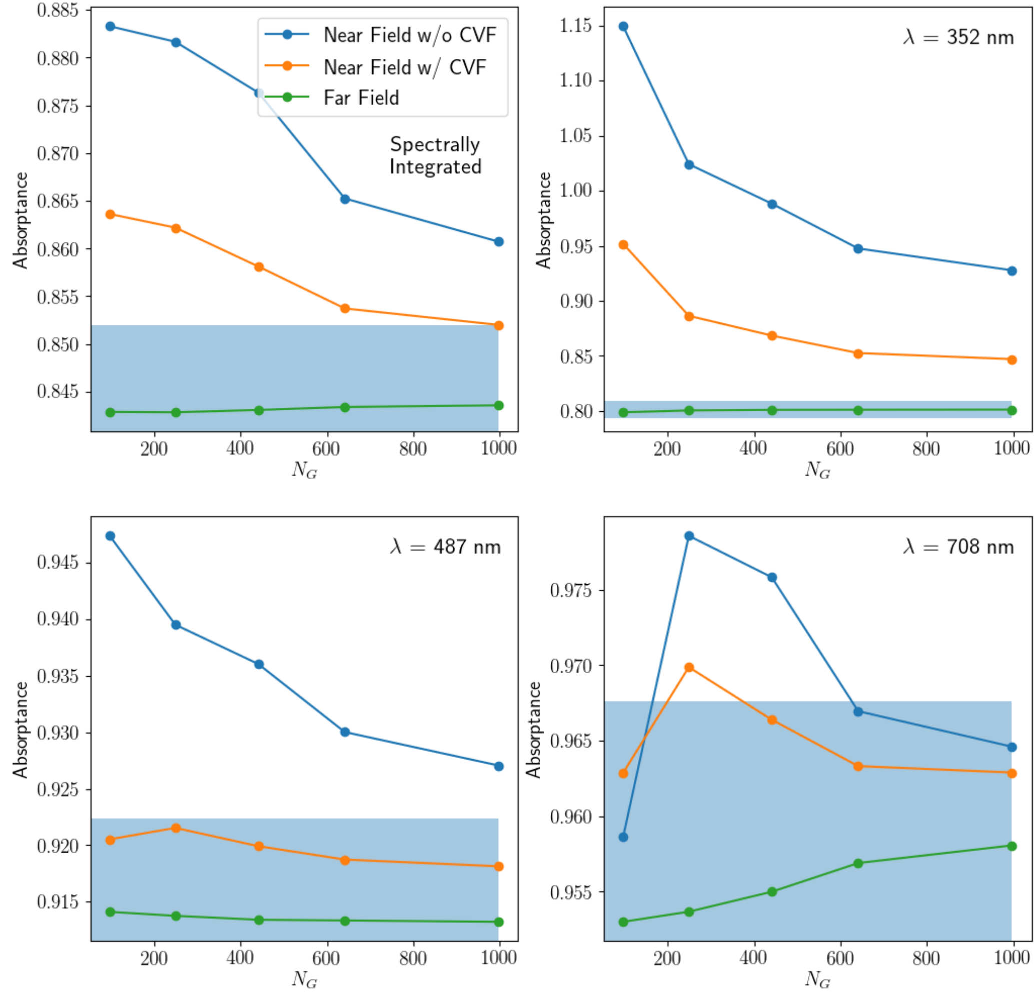

Figure 4.4: Convergence of the spectrally integrated and wavelength resolved $A_{\text{far field}}$, $A_{\text{near field}}$ using the CVF fields, and $A_{\text{near field}}$ using the unmodified fields. Blue box indicates 1% error bars around the $N_G = 997$ far field absorptance, showing that the far field absorptance is self-converged in all cases; at short wavelengths, neither near field absorptance line is converged. The CVF fields improve accuracy at all wavelengths.

4.3 Continuous variable formulation

The CVF is a modification to RCWA that only Fourier reconstructs quantities that are continuous across material interfaces in real space. Near material interfaces, these quantities are the components of the displacement field $\mathbf{D}$ that are normal to, and the components of the electric field $\mathbf{E}$ that are tangential to, the interface. Using these real-space continuous quantities, one can determine the full electric field everywhere by using the constitutive relationship

$$\mathbf{D} = \epsilon \mathbf{E} \tag{4.14}$$

with a discontinuous real-space ϵ. S^4 already uses a related technique for calculating the Fourier modes, but it does not use this method when extracting real-space quantities.

To perform this decomposition with arbitrarily shaped 2D regions within a layer, one must construct a locally-defined vector field that is tangent to all material interfaces and periodic in the plane, which can be generated automatically, as is done by S^4 [85, 86]. This vector field induces an associated projection operator T that can be used to project the Cartesian components of the electromagnetic fields onto this local coordinate system such that:

$$\begin{bmatrix} E_{T,x}(\mathbf{r}) \\ E_{T,y}(\mathbf{r}) \end{bmatrix} = T(\mathbf{r}) \begin{bmatrix} E_x(\mathbf{r}) \\ E_y(\mathbf{r}) \end{bmatrix} \tag{4.15}$$

$$\begin{bmatrix} D_{N,x}(\mathbf{r}) \\ D_{N,y}(\mathbf{r}) \end{bmatrix} = N(\mathbf{r}) \begin{bmatrix} D_x(\mathbf{r}) \\ D_y(\mathbf{r}) \end{bmatrix}, \tag{4.16}$$

where $N = 1 - T$, $\mathbf{E}_T$ is the component of $\mathbf{E}$ along the tangential vector field and $\mathbf{D}_N$ is the component of $\mathbf{D}$ perpendicular to the tangential vector field. The total field satisfies

$$\begin{bmatrix} E_x(\mathbf{r}) \\ E_y(\mathbf{r}) \end{bmatrix} = \begin{bmatrix} E_{T,x}(\mathbf{r}) \\ E_{T,y}(\mathbf{r}) \end{bmatrix} + \begin{bmatrix} E_{N,x}(\mathbf{r}) \\ E_{N,y}(\mathbf{r}) \end{bmatrix}. \tag{4.17}$$

By taking the Fourier transform of $T(\mathbf{r})$, the projection onto the tangential vector field can also be done in Fourier space. Mirroring the notation of [99], we denote discrete real-space quantities with upper case letters (as in E_x to represent the vector $E_x(\mathbf{r}_i)$ for many points $\mathbf{r}_i$), vectors of Fourier coefficients with lower case letters surrounded by single brackets (as in $[e_x]$), and Fourier space matrix operators with double brackets (as in $[\![T]\!]$). Using this notation, the Fourier transform of Eq. (4.15) is given by [99]:

$$\begin{bmatrix} e_{T,x} \\ e_{T,y} \end{bmatrix} = [\![T]\!] \begin{bmatrix} e_x \\ e_y \end{bmatrix}, \tag{4.18}$$

where $[\![T]\!]$ is the Fourier convolution matrix [86, 99]. That is, one calculates the Fourier transform $\tilde{T}(\mathbf{G})$ of $T(\mathbf{r})$, and the $(\mathbf{G}, \mathbf{G}')$ element of $[\![T]\!]$ is $\tilde{T}(\mathbf{G} - \mathbf{G}')$.

We extract $[e_x]$ and $[e_y]$ from a standard RCWA implementation and then construct $[d_{N,x}]$ and $[d_{N,y}]$. Since $\epsilon(\mathbf{r})$ and $\mathbf{E}_N(\mathbf{r})$ are both discontinuous, the proper Fourier factorization takes [112]

$$\left[\!\left[\frac{1}{\epsilon}\right]\!\right]^{-1}[\mathbf{d}_N] = [\mathbf{e}_N], \tag{4.19}$$

where $[\![1/\epsilon]\!]^{-1}$ is the $2N_G \times 2N_G$ block diagonal matrix whose upper-left and lower-right blocks are the inverse of the $N_G \times N_G$ Fourier convolution matrix of $1/\epsilon(\mathbf{r})$. In [99], Weismann et al. showed that the symmetric formulation,

$$\begin{bmatrix} d_{N,x} \\ d_{N,y} \end{bmatrix} = \frac{1}{2}\left([\![N]\!]\left[\!\left[\frac{1}{\epsilon}\right]\!\right]^{-1} + \left[\!\left[\frac{1}{\epsilon}\right]\!\right]^{-1}[\![N]\!]\right)\begin{bmatrix} e_x \\ e_y \end{bmatrix}, \tag{4.20}$$

converges well and conserves power for lossless structures, and we use this form.

After finding $d_{N,x}$ and $d_{N,y}$ we reconstruct the real space electric field

$$\mathbf{E}_N(\mathbf{r}) = \frac{\mathcal{F}^{-1}(\mathbf{d}_N)}{\epsilon_0\epsilon_r(\mathbf{r})}, \tag{4.21}$$

where $\mathcal{F}^{-1}$ indicates the inverse Fourier transform. This $\mathbf{E}_N(\mathbf{r})$ has correct discontinuities at material interfaces where ϵ_r jumps. Finally, the real space electric fields in Cartesian coordinates can be recovered using:

$$E_y(\mathbf{r}) = \frac{\mathcal{F}^{-1}(d_{N,y})}{\epsilon_0\epsilon_r(\mathbf{r})} + \mathcal{F}^{-1}(e_{T,y}) \tag{4.22}$$

$$E_x(\mathbf{r}) = \frac{\mathcal{F}^{-1}(d_{N,x})}{\epsilon_0\epsilon_r(\mathbf{r})} + \mathcal{F}^{-1}(e_{T,x}). \tag{4.23}$$

Figure 4.5 shows the norm-squared components of the electric fields computed using unmodified RCWA and the CVF on a line cut along the x-direction through the center of the nanowire. In this cut, E_x is normal to the interface and should therefore be discontinuous, while E_y should be continuous. Note the Gibbs oscillations in the standard result for E_x, while the CVF result has introduced discontinuities at the boundaries and significantly reduced the amplitude of the Gibbs oscillations.

Figure 4.3(b) shows the improved agreement between the CVF absorptance and the well-converged far field absorptance. Figure 4.6 shows the relative difference between the far and near field absorptances calculated with and without the CVF. It is clear that the CVF significantly improves the agreement at all wavelengths, but the disagreement is still significant for wavelengths shorter than 450 nm. Figure 4.6 indicates the AM1.5G spectrum, which shows that the CVF-based $A_{\text{near field}}$ agrees well with the far field results through the most important parts of the solar spectrum. In the next section, we introduce a simple rescaling technique to increase accuracy of the near fields at all incident wavelengths.

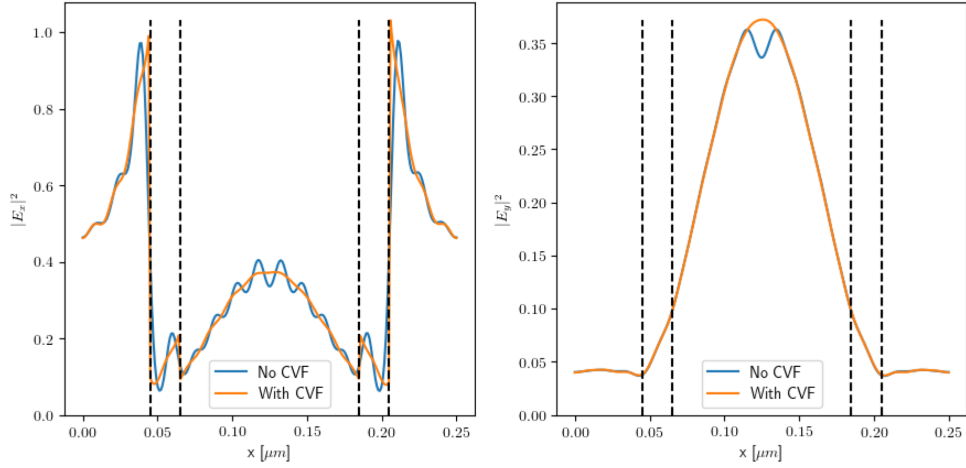

Figure 4.5: Line cuts of $|E_x|^2$ (left) and $|E_y|^2$ (right) along the x-direction through the center of the nanowire 101 nm from the top of the nanowire with and without use of the CVF with an incident wavelength of 453 nm and $N_G = 997$. The CVF formulation reduces the Gibbs oscillations in E_x and introduces proper discontinuities while maintaining the continuity of E_y.

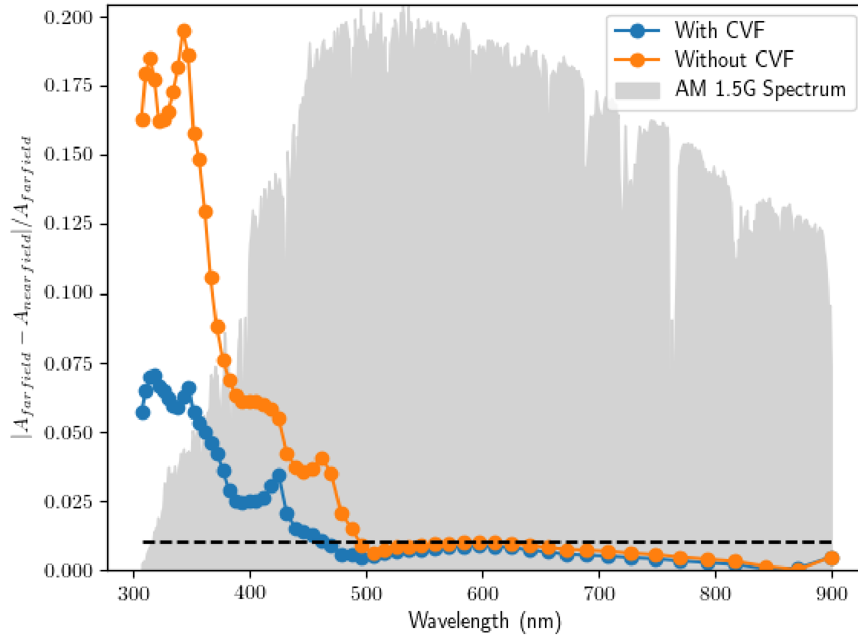

Figure 4.6: Relative difference between the far field and near field calculations of A with $N_G = 997$. Orange line uses the unmodified fields in Eq. 4.13, blue line uses the CVF fields. Gray background shows the AM1.5G solar spectrum, which is strongest in the region of good convergence. Black dashed line indicates the 1% mark.

4.4 Rescaling technique

In device simulations, the total optical generation rate must be determined accurately. The exact position where generation occurs is somewhat less important, as the carriers drift and diffuse, and deviations on the scale of a few nanometers are rarely significant. We can ensure that the total generation in each layer is calculated correctly, even with inexpensive RCWA calculations that have not fully converged the local fields. To achieve this goal, we use the well-converged far field results (as shown in Fig. 4.2) to rescale the components of the near fields in each layer such that $A_{\text{far field}}$ and $A_{\text{near field}}$ agree exactly. We define a rescaling factor F for each layer i and frequency ω:

$$F_i(\omega) = \frac{A^i_{\text{far field}}(\omega)}{A^i_{\text{near field}}(\omega)}. \tag{4.24}$$

Then, the components of $\mathbf{E}$ are rescaled such that:

$$\mathbf{E}^{\text{rescaled}}(\omega) = \sqrt{F_i(\omega)}\mathbf{E}(\omega) \tag{4.25}$$

for fields in the appropriate layer, ensuring that the total generation rate in each layer matches the accurate far-field result exactly.

This rescaling technique allows accurate determination of spectrally-integrated generation rates with small numbers of basis terms. Figures 4.7 and 4.8 show line cuts through the test structure at three representative wavelengths and spectrally integrated under AM1.5G illumination, calculated with 60 equally spaced frequencies. At 487 nm, the fields are quantitatively converged at small N_G, while the Gibbs oscillations are not entirely removed either at shorter or longer wavelengths. Calculations dependent on spectrally resolved local fields, such as external quantum efficiency (EQE), thus require relatively large N_G at some wavelengths. When the fields are spectrally integrated, however, the essentially random phases of the oscillations average away, and the spectrally-integrated fields are quantitatively converged by $N_G = 197$. Figure 4.9 compares the rescaled spectrally-integrated generation rates along a plane through the center of the nanowire at $N_G = 997$ and 197, showing the excellent agreement that rescaling permits, even at low N_G. This spectrally integrated generation rate is sufficient for optoelectronic modeling while reducing the requirements for N_G by a factor of 5.

The computational cost of the RCWA method scales as N_G^3, so reducing N_G by a factor of 5 (from 1000 to 200) theoretically reduces the runtime by a factor of 125, and reducing to $N_G = 100$ can reduce the runtime by a factor of 1000. Extracting the electric fields on a dense mesh of points, however, also has a computational cost, and for sufficiently small N_G, this electric-field extraction limits the runtime. Figure 4.10 shows an estimate of the simulation run times for a single incident wavelength. Each desired wavelength must be calculated separately, and they all take approximately the same amount of processor time. Simulations were run on a single core of an Intel Xeon E5-2640 v4 CPU with a 2.40GHz clock speed, and utilized OpenBLAS matrix libraries for all matrix manipulations. The figure shows both the simulation time for RCWA to determine the field amplitudes, in

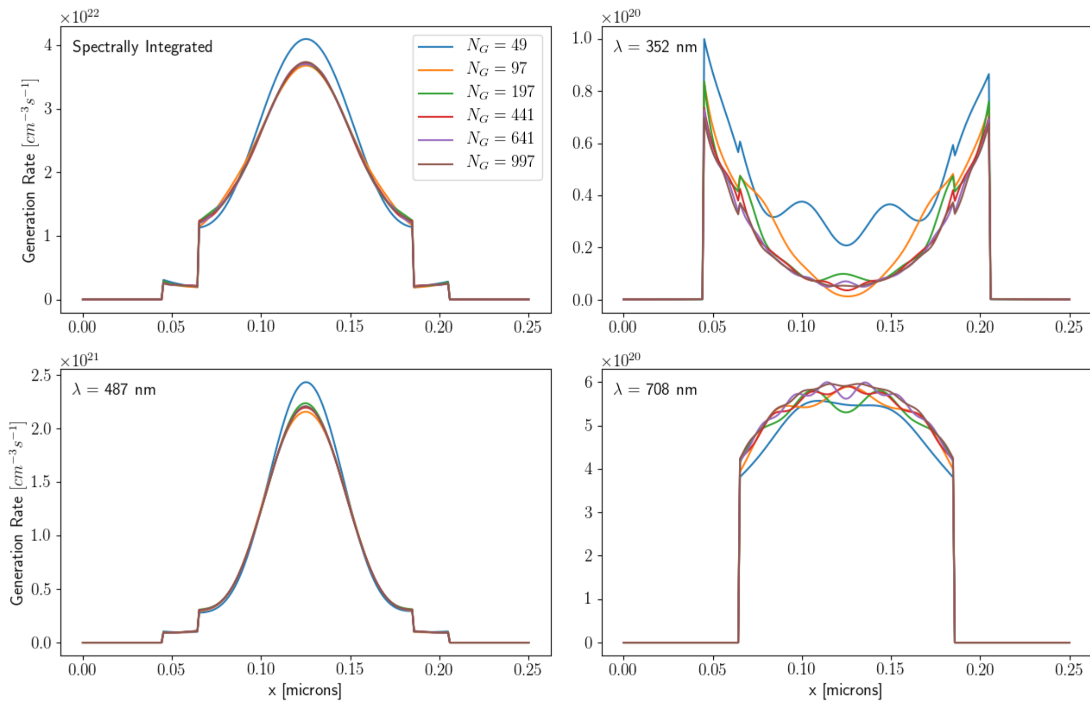

Figure 4.7: Rescaled generation rate on a line cut along the x direction through the center of the nanowire 83 nm from the top of the nanowire layer. The spectrally integrated and $\lambda = 487$ nm case are clearly converged even at $N_G = 197$, while the longer and shorter wavelengths need high N_G to remove all the Gibbs oscillations.

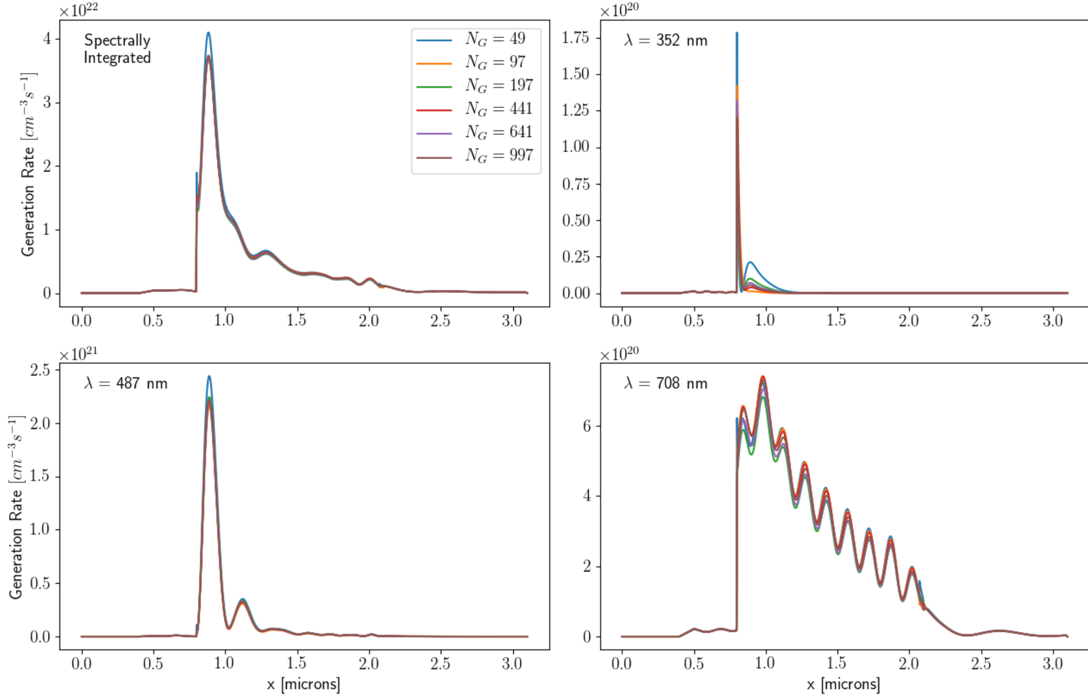

Figure 4.8: Rescaled generation rate on a line cut along the z direction through the center of the nanowire core. As in Fig. 4.7, the spectrally integrated results are well converged at low N_G while the shortest and longest wavelengths require higher N_G for convergence.

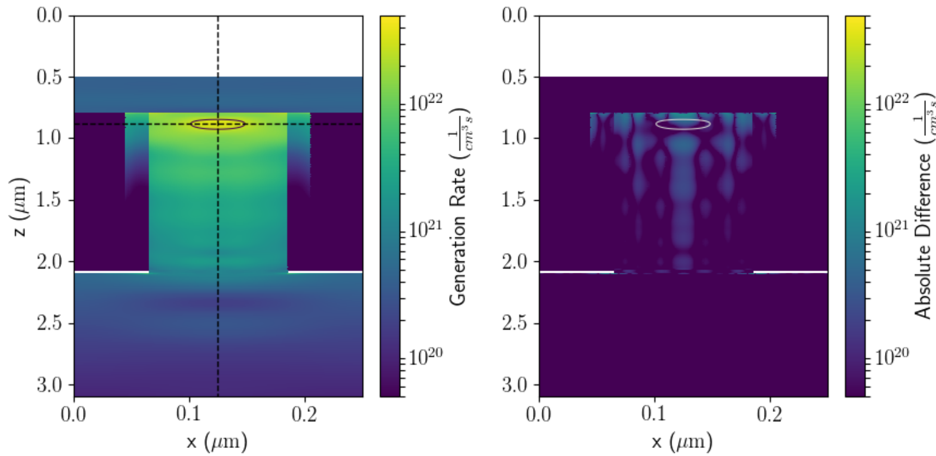

Figure 4.9: Left: Spectrally integrated generation rate with AM1.5G spectrum along a cut through the middle of the nanowire using the rescaled fields with $N_G = 197$. Right: Absolute difference between the generation rate shown at left and the well-converged, rescaled generation rate at $N_G = 997$. The deviations between the two generation maps are small. White regions are areas of vacuum and SiO_2, where the generation rate is zero. Area within the solid contour indicates the location of peak generation, greater than 2.75×10^{22} $cm^{-3}s^{-1}$, while the differences there are much smaller. Dashed lines indicate line cuts shown in Figs. 4.7 and 4.8.

Fourier space, and for the extraction of those fields on the dense real-space mesh described above. The CVF method does not significantly change the run times. Efforts were made to minimize data input/output time and resource contention in all benchmarks. These results show that running at $N_G = 197$ has a cost 25 times less than at $N_G = 997$, and that cost is dominated by the field calculation and export. The field calculation and export time can possibly be optimized further and would certainly be reduced if a coarser mesh were requested. Decreasing that cost could allow computation times to be reduced by an additional factor of 5. Simulations at each frequency are completely independent, so computation time for a full spectral sweep can be easily reduced by running all frequencies in parallel [113]. With a sufficient number of CPU cores, a full spectral sweep can be run in the same clock time as a single simulation.

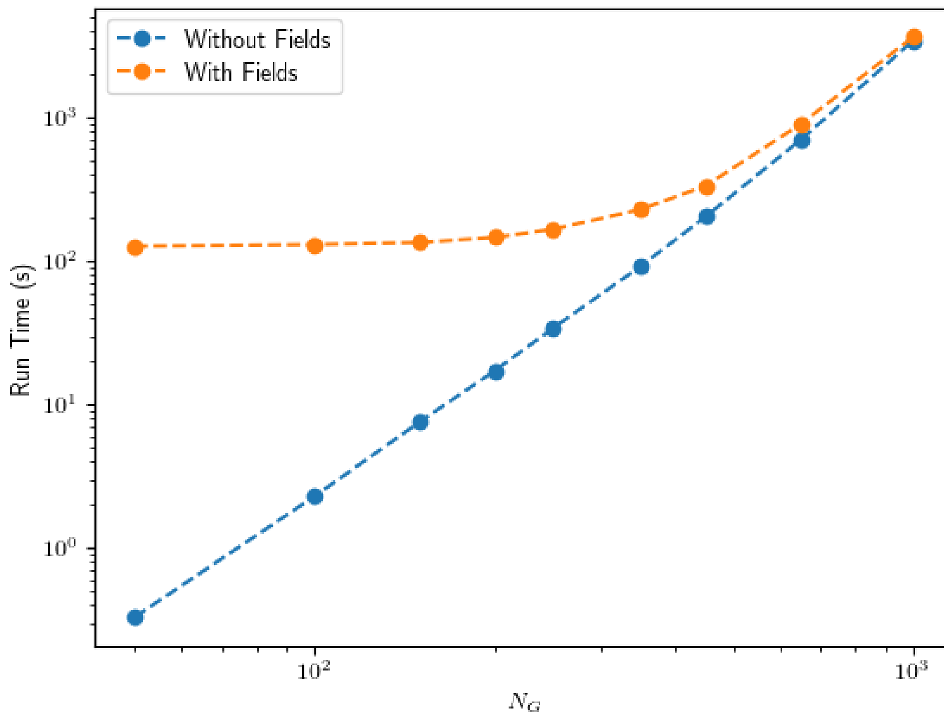

Figure 4.10: Run time of a single simulation as a function of basis terms with and without computation of the local fields. Field computations dominate the runtime at small N_G. A least-squares fit to the blue line yields a slope of 3.06, consistent with the N_G^3 scaling of the QR algorithm for solving eigenvalue problems. Dashed lines are guides to the eye.

4.5 Conclusion

In this work, we investigate the accuracy of RCWA for optical modeling of nanowire solar cells. We find excellent accuracy with low computational cost at long incident wavelengths, but poor accuracy at short incident wavelengths. To increase the accuracy of RCWA we extend the open-source library S^4 [86] to include an already published technique for

improving near field computations in RCWA [99]. Our implementation mitigates the Gibbs phenomenon and introduces physically expected discontinuities in the fields at material interfaces, improving convergence of the near fields at all incident wavelengths. To bring convergence within a 1% tolerance, we introduce a simple rescaling technique that uses the well converged far field quantities to rescale the near fields on a per layer basis. These improvements open up the possibility of using RCWA as a low cost optical modeling technique in a full optoelectronic device model of nanowire solar cells.

Chapter 5

Optical Optimization of Passivated GaAs Nanowires on GaAs Substrates

This chapter exists as a conference proceeding article in [96], and is reproduced with permission here.

5.1 Introduction

Nanowire solar cells (NWSC) have emerged as promising candidates for highly efficient, inexpensive solar energy harvesters. With the correct choice of nanowire array geometry, one can reduce material requirements relative to flat-panel solar cells without sacrificing absorption or device efficiencies.

The excellent broadband absorption of NWSC has been widely demonstrated [114, 15, 17, 3] and is due to nanowires having larger absorption cross sections than their physical cross sections. Additionally, the optical modes of the nanowire create internal resonances that enhance overall absorption [115] [9]. The small cross sectional area of the nanowires allows them to be grown on lattice-mismatched substrates with the resulting strain accommodated without dislocations. This flexibility enables growth on inexpensive substrates and creation of tandem solar cells of lattice-mismatched materials, further reducing cost and improving potential efficiency [20, 21].

Despite the promising optical properties of NWSC, their large surface area contributes to high levels of surface recombination. This problem has been solved by introducing a passivating shell of higher bandgap material around the nanowire core (as illustrated in Figure 5.1), which has proven to be an effective method for increasing device performance [44].

While the necessity of a passivating shell for electrical device performance has been well demonstrated [48], little work has been done to investigate the optical consequences of adding such a shell. Because the shell material has a higher bandgap and different optical properties than the core material, it has the potential to change the optical characteristics of nanowire devices.

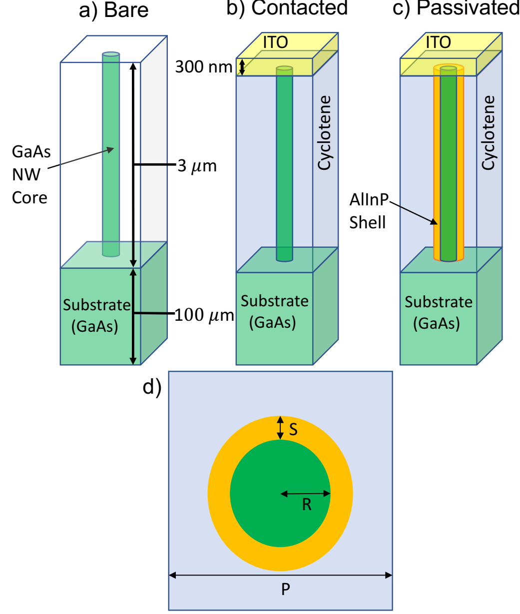

Figure 5.1: A single unit cell of the square lattice nanowire array. a) An unpassivated and uncontacted bare nanowire. b) An unpassivated, contacted nanowire planarized with dielectric material. Although there is a non-trivial geometry in the x-y plane, the material parameters remain constant along z within each layer. c) A fully passivated nanowire. d) A top down view of the nanowire layer with core radius R, array period P, and shell thickness S.

In this work, we use rigorous coupled wave analysis (RCWA) to perform wave-optics simulations of a square array of GaAs nanowires passivated by AlInP shells. We discuss the advantages of the RCWA method and present the shell thickness, core radius, and array periodicity that optimize the maximal photocurrent density J_{ph}. We then give valuable guidance for the design of optical NWSC arrays.

5.2 Methods

RCWA [76, 98] (also referred to as the Fourier modal method) is a semi-analytic, frequency-domain method for solving Maxwell's equations. Unlike the finite element method (FEM) or the finite difference methods, RCWA propagates fields in the z-direction analytically, reducing the number of discretized dimensions from three to two. This analytic propagation requires the device to be composed of discrete layers, where the material parameters must be constant along the z-direction within a layer. Vertical nanowire designs (see Figure 5.1) are ideal systems for such analysis. Because the axial spatial direction is treated analytically, simulation times are independent of the layer thicknesses and any number of layer thicknesses can be explored during a single simulation essentially for free. We implement our model using the open-source RCWA library S^4 [86]. At each frequency, S^4 expands the electromagnetic fields within each layer using a 2D plane-wave basis with exponential

dependence in the axial direction. The fields are made to satisfy continuity conditions at layer interfaces using the S-matrix algorithm.

We simulate the nanowire array absorption spectrum by dividing the AM1.5G spectrum into 120 equally spaced frequency bins from 350-900 nm. A circularly polarized plane wave is injected at normal incidence onto the first layer of the device. Due to the circular symmetry of the nanowire, this polarization choice removes the need to simulate two independent polarizations for incoherent illumination [48]. We impose periodic boundary conditions at the x and y limits of the simulation domain to simulate an array of nanowires. The materials are defined solely through their frequency-dependent refraction coefficient n and extinction coefficient k [16, 110]. Referring to Fig. 5.1, we first model a "bare" nanowire. We then model a nanowire contacted by a top layer of ITO and planarized with a cyclotene dielectric ("contacted" nanowire). Finally, we model a contacted, planarized, passivated nanowire ("passivated" nanowire).

We seek to maximize the photocurrent density, where we assume that each absorbed photon produces one excited electron. Thus, we maximize spectral absorbance weighted by photon number

$$\bar{A} = \frac{\int \frac{\lambda}{hc} A(\lambda) I(\lambda) d\lambda}{\int \frac{\lambda}{hc} I(\lambda) d\lambda} \tag{5.1}$$

where $A(\lambda)$ is the wavelength dependent absorption coefficient of the NWSC, $I(\lambda)$ is the AM1.5G spectrum in W·m^{-2}·nm^{-1}, and hc/λ is the energy of the incident photon. Assuming perfect carrier collection, the photocurrent density is then

$$J_{ph} = \frac{q}{hc} \int \lambda A(\lambda) I(\lambda) d\lambda \tag{5.2}$$

which is directly relatable to Eq. (5.1) by $J_{ph} = \bar{A} \cdot 33.37$ mA/cm^2. We obtain the wavelength-dependent absorption coefficients from

$$R(\lambda) = \frac{P_{ref}}{P_{in}} \tag{5.3}$$

$$T(\lambda) = \frac{P_{tran}}{P_{in}} \tag{5.4}$$

$$A(\lambda) = 1 - R(\lambda) - T(\lambda) \tag{5.5}$$

where P_{in} is the incident power, and P_{ref} and P_{tran} are the reflected and transmitted powers, respectively.

There exists a subtle but important detail concerning where in the device we choose to calculate $T(\lambda)$. Referring back to Figure 5.1, there are two reasonable choices. The first places the calculation of $T(\lambda)$ at the bottom of the substrate. The second places the calculation of $T(\lambda)$ at the nanowire-substrate interface. Looking forward to an electronic drift-diffusion based model, we want our optical simulations to maximize the number of charge carriers generated near the p-n junction of the device. By doing this, we decrease the distance carriers must travel to reach the junction and thus increase their likelihood

Table 5.1: Optimization Results

System	**Array Period** [nm]	**Core Radius** [nm]	$\mathbf{J}_{ph}$ [mA cm^{-2}]
Bare Nanowire	338	85	29.27
Unpassivated nanowire	326	103	28.45

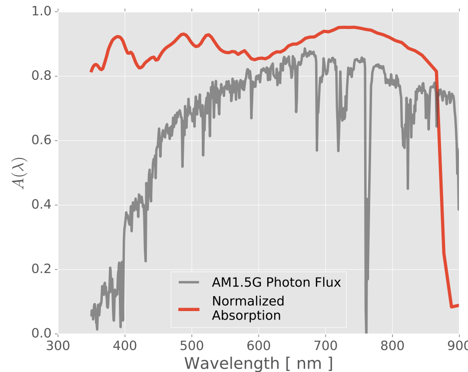

Figure 5.2: The normalized absorption spectrum, $A(\lambda)$, of the optimized contacted nanowire (see Table 5.1) and the photon-weighted AM1.5G spectrum, $\frac{\lambda}{hc}I(\lambda)$, in arbitrary units.

of being separated and collected. In axial junction nanowires, the junction is usually placed near the top of the nanowire core. By choosing to calculate $T(\lambda)$ at the nanowire-substrate interface when optimizing $\bar{A}$, the optimizer searches for a device geometry that shifts absorption into the nanowire. This achieves the desired affect of concentrating carrier generation near the junction. In all optimizations and figures, $T(\lambda)$ was calculated at the nanowire-substrate interface.

As a first example of modeling NWSC via the RCWA method, we use Nelder-Mead simplex optimization to find the optimal array period and nanowire radius. This optimization allows us to find the desired geometric parameters to high precision without the unnecessary overhead of blind parameter sweeps. During all optimizations, the ITO thickness is fixed at 300 nm, the nanowire length at 3 μm, and the substrate thickness at 100 μm.

We find the array period and core radius that maximize $\bar{A}$ for the bare nanowire (shown in Table 5.1), in good agreement with previous FEM-based results [16]. The results from this optimization are used as a starting point to find the optimal parameters for the contacted nanowire. Finally, we explore the effects of adding a passivating shell to the contacted nanowire.

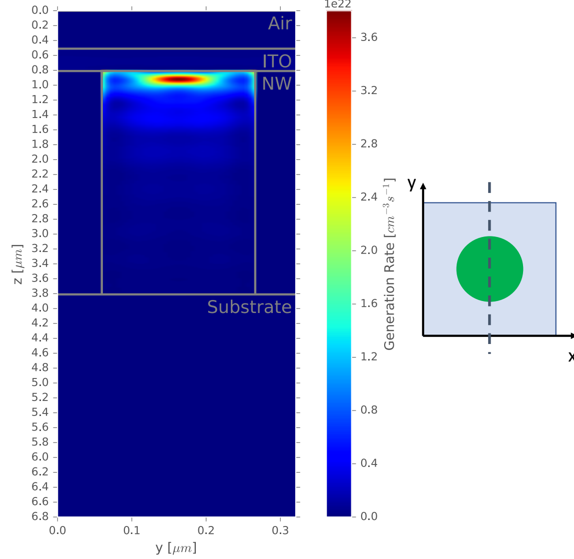

Figure 5.3: The generation rate of the device along a fixed yz plane through the center of the nanowire core. The schematic on the right clarifies where the axial slice through the device was taken.

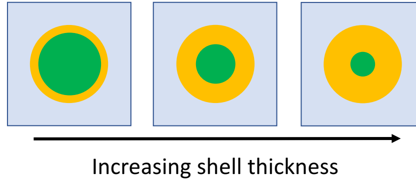

Figure 5.4: A top down view of the nanowire layer as the shell thicknesses is increased. Green represents GaAs and orange represents the AlInP shell.

5.3 Results

When ITO and cyclotene are added to the optimized bare nanowire, J_{ph} drops to 28.01 mA/cm^2. Reoptimizing the geometry improves J_{ph} by 1.5%, resulting in a value of 28.46 mA/cm^2. Table I shows the optimal geometric parameters for the bare nanowire and the contacted nanowire, indicating the significant geometric changes when the ITO and dielectric are included. The absorption spectrum for a contacted nanowire using those parameters is shown in Figure 5.2. As expected, the geometry of the nanowire is tuned to place an absorption peak at the strongest part of the spectrum, between roughly 600-800 nm. Figure 5.3 shows the generation rate profile along a 2D slice through the contacted nanowire. Our choice for $T(\lambda)$ has concentrated the generation rate within the desired region at the tip of the nanowire.

Next, we sweep through shell thicknesses of 10-80 nm in steps of 10 nm while keeping the total core+shell radius fixed at 103 nm (see Figure 5.4), which is the optimal value from Table 5.1. The affect is shown in Figure 5.5. Below 40 nm absorption losses are minimal, and beyond that dramatic losses to J_{ph} occur. In terms of overall performance,

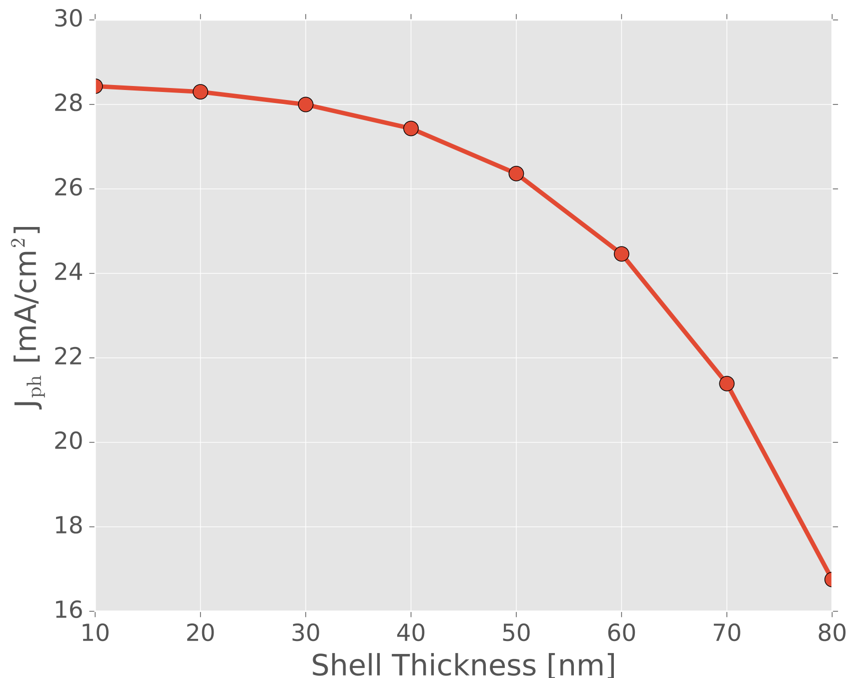

Figure 5.5: Photocurrent density vs. shell thickness for an array period of 315 nm and a core radius of 106 nm.

the passivating shell is a necessity and the small absorption gains accrued from removing it do not outweigh the performance costs due to surface recombination.

We now consider fixed thicknesses and reoptimize to find the optimal core diameter and array period, with results shown in Figure 5.6. These parameters vary considerably from the contacted nanowire optimal values, and in general one needs to increase the array period and decrease the core radius as the shell thickness increases. Figure 5.7 shows the improvement gained from reoptimizing for each shell thickness. Herein lies the value of device optimization through simulation. We see that by reoptimizing the geometry of the nanowire array all losses to J_{ph} can be almost entirely recovered. It is possible to accommodate the electrical benefits of a passivating shell without negatively affecting device absorption by appropriately readjusting the array period and core radius. With the correct choice of geometric parameters, device fabricators can dramatically improve optical NWSC performance.

5.4 Conclusion

In this paper, we outline a method for efficient optical simulation of NWSC devices. Our first demonstration of this method is a geometric optimization to enhance photon-weighted optical absorption. This method will be useful for combined optical and electrical simulations [48], with a significant reduction in computational cost. We find that optimal

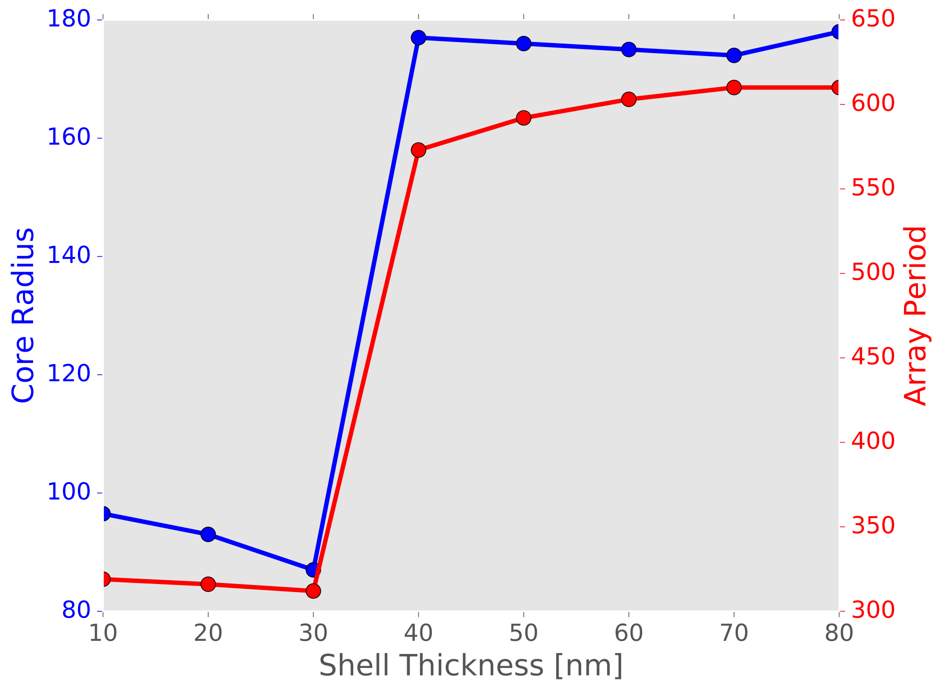

Figure 5.6: Reoptimized core radius (left axis) and array period (right axis) that give the maximum possible J_{ph} for fixed shell thicknesses. Lines are guides to the eye.

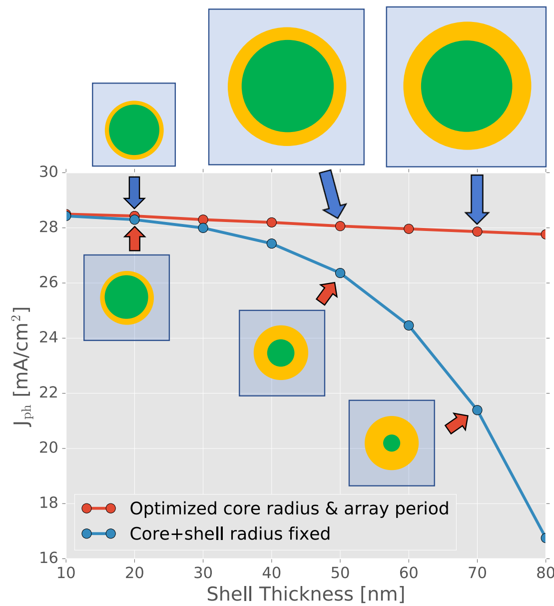

Figure 5.7: A comparison of optimized and unoptimized photocurrent densities for a fixed shell thickness. The unoptimized data is the same as in Figure 5.5. The optimized data is the maximal photocurrent density resulting from a reoptimization of the array period and core radius at each shell thickness.

absorption occurs in the absence of a passivating shell, and outline the losses to the photocurrent density as a function of the shell thickness. In the presence of a shell of fixed thickness, we present the array period and core radius that maximize the photocurrent density and show that by reoptimizing the nanowire geometry the losses incurred by adding a shell can be almost completely recovered. This information will be invaluable for use in growing efficient GaAs NWSC.

Chapter 6

Electrical Optimization of Passivated GaAs Nanowires on Silicon Substrates

6.1 Introduction

Nanowires are excellent light absorbers in the visible range due to their unique geometry. However, their favorable light absorbing properties come at the price of increased complexity when attempting to optimize their electrical performance. In a p-i-n solar cell structure, the doping levels in each of the p, i, and n regions and their relative heights must be tuned to maximize efficiency. The process of optimizing these doping levels and heights is in essence an optimization of the band diagram to maximize carrier separation and carrier transport out of the active semiconductor region of the device. In the approximations used here, these doping levels do not affect the optical properties of the nanowires. However, the thickness and doping of each region must be carefully designed to match the locations of optical generation [48], in order to maximize the collection of carriers. There also exists a trade off between the *optically optimal* device geometry and the *electrically optimal* device geometry due to the high rates of surface recombination along the nanowire side walls. Optically, increasing the length of the nanowire increases overall light absorption and therefore carrier generation. Electrically, increasing the length of the nanowire increases the surface to volume ratio and therefore increases the rate at which generated carriers are captured and recombined in trap states along the surface. Therefore, there must exist some ideal combination of nanowire length, period, and radius that maximizes light absorption while simultaneously minimizing surface recombination.

An additional benefit of the nanowire solar cell is the ability to grow nanowires on lattice mismatched substrates. This opens up the opportunity for both efficient GaAs solar cells grown on cheap silicon substrates and multi-junction solar cells grown on silicon. The finite in-plane dimensions of nanowires allow them to relieve the strain induced by growth on lattice mismatched substrates via lateral relaxation, avoiding efficiency-reducing threading dislocations in the crystal lattice. The critical nanowire radii below which dislocations do

not occur is dependent on the magnitude of the lattice mismatch. Theoretical predictions suggest 20 nm as the upper bound on critical radii for GaAs grown on Si [116], but larger values have been achieved experimentally, with radii up to 146 nm reported in Ref. [117].

As a first step in this chapter we perform optimizations of the doping levels and heights of the p-i-n regions in a GaAs nanowire of fixed total length grown on a silicon substrate (see Fig. 6.1) using a coupled opto-electronic device model. The optical model is performed in 3D using RCWA, and then interpolated onto a 2D cylindrically symmetric electrical model, which uses the finite volume method (FVM) implemented in TCAD Sentaurus [53]. We use the optically optimized array period and core radius from Ch. 5 as a starting point, and show doping levels and heights that maximize the overall device efficiency. This optimization does not require repeating the optical study, as only electrical properties change. The resulting parameters will provide valuable insight to device growers, and shed light on the underlying physics that must be utilized to maximize device performance. All computations were done using the same machine, CPU, and matrix libraries as the Chapters 4 and 5.

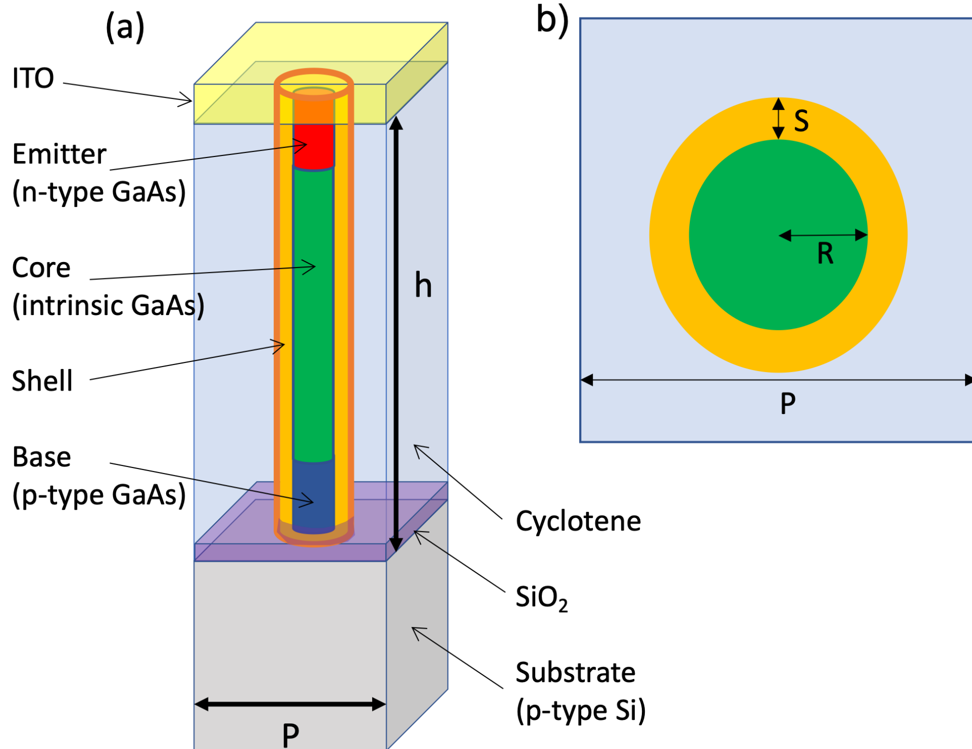

Figure 6.1: The test structure used in the electrical optimization procedure. Adapted from [96]. (Left) A unit cell of the periodic array of nanowires. (Right) Plan view, showing the dimensions of the unit cell, core, and shell.

6.2 Optical-to-Electrical Conversion

As discussed in Chapters 2-5, Maxwell's equations are solved in 3D using RCWA to compute the optical generation rate $G(\mathbf{r})$ as a function of space on a regular grid. The nanowire array absorption spectrum is simulated by dividing the AM1.5G spectrum into 120 equally spaced frequency bins from 300-900 nm. The number of basis terms N_G was fixed at 400 for all optical simulations, and the rescaling technique described in 4 was used to increase the accuracy of $G(\mathbf{r})$.

The computational cost of full 3D electrical models can be prohibitively expensive, making closed loop device optimizations infeasible. To reduce computational cost of the electrical model, the technique described in [48] was used to reduce the geometry of the system from 3D down to 2D (see Figure 6.2) by approximating the square unit cell as rotationally symmetric about the nanowire core. The explanation of this reduction is reproduced verbatim from [48] below.

> Due to the square array geometry, the problem does not have a rotational symmetry even for cylindrical nanowires. Deviations from rotational symmetry in the NW optical absorption are not significant and are unlikely to be practically important as carriers can quickly diffuse across the radius of the nanowire; the effect is slightly more significant in the substrate absorption. Due to the square symmetry of the array we only need the carrier generation rate $G(f_i, \mathbf{r})$ obtained from the 3D simulation within two planes: the y,z plane called cut A, that passes though the symmetry axis z and a middle of the side wall of the simulation domain, indicated in the top view of Fig. 6.2 (a), and the diagonal x=y,z plane (cut B), that passes though the symmetry axis of NW and a corner of simulation domain. We obtain the average generation rate needed for further calculations in a plane through the NW symmetry axis z, by averaging the $G(f_i, r)$ extracted in A and B cuts. The generation rate of all simulation domains contained within the green circle marked in Fig. 6.2(a) and obtained using this method, is a good approximation of the 3D average, as both A and B planes contain information about those domains. For the domain between the green and red circles the array periodicity is used to extend the plane A data to larger r. The averaged generation rate is then interpolated from the regular grid of the optical simulations onto the irregular FVM electrical mesh using a simple linear interpolation procedure.
>
> It is important to note that this procedure does not affect the absorption properties of the NW, and only impacts the treatment of the substrate absorption in the electrical model. In the cylindrical model, all quantities are defined on the r,z plane. The radius R must be chosen such that the area of a unit cell is correctly modelled, i.e. $a^2 = \pi R^2$. The comparison between these circular areas, and the square unit cell base in the 3D optical model is shown in Fig. 6.2(b). The approximation of the square by a circle results in the existence of the areas in which $G(f_i, r)$ is either double counted or neglected. These regions contain only substrate and are not expected to strongly affect results. In the worst case

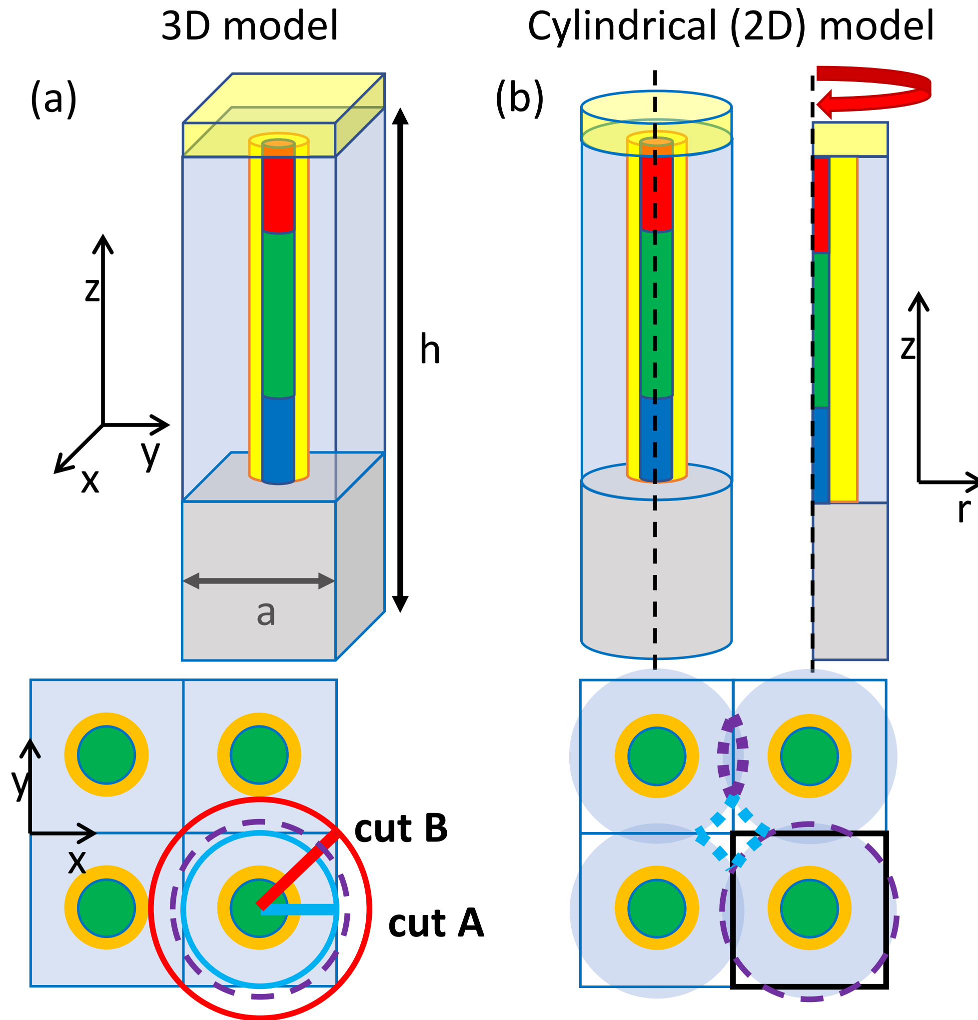

Figure 6.2: Adapted from [48](a). The 3D simulation structure containing one NW, and a top view of a part of the NW array. At the bottom, blue and red solid lines represent the planes on which $E(f_i, r)$ is extracted, while the circle of corresponding color shows the equivalent area. Purple-dashed line denotes simulation domain of the electrical model. (b) 3D geometry in cylindrical coordinates and the A simulation plane. A top view of the NW array shows the areas of the simulation domain overlap (purple-dottted lines) and areas that are not simulated in electrical model (blue-dotted lines)

this Cartesian to cylindrical transformation procedure produces integrated optical generation input to TCAD Sentaurus that is within 1.5% agreement with the integrated optical generation extracted from full 3D RCWA data. Generally the agreement is within 1%, which translates to 0.3 mA/cm^2 uncertainty for the maximum achievable current J_{ph} from the structure.

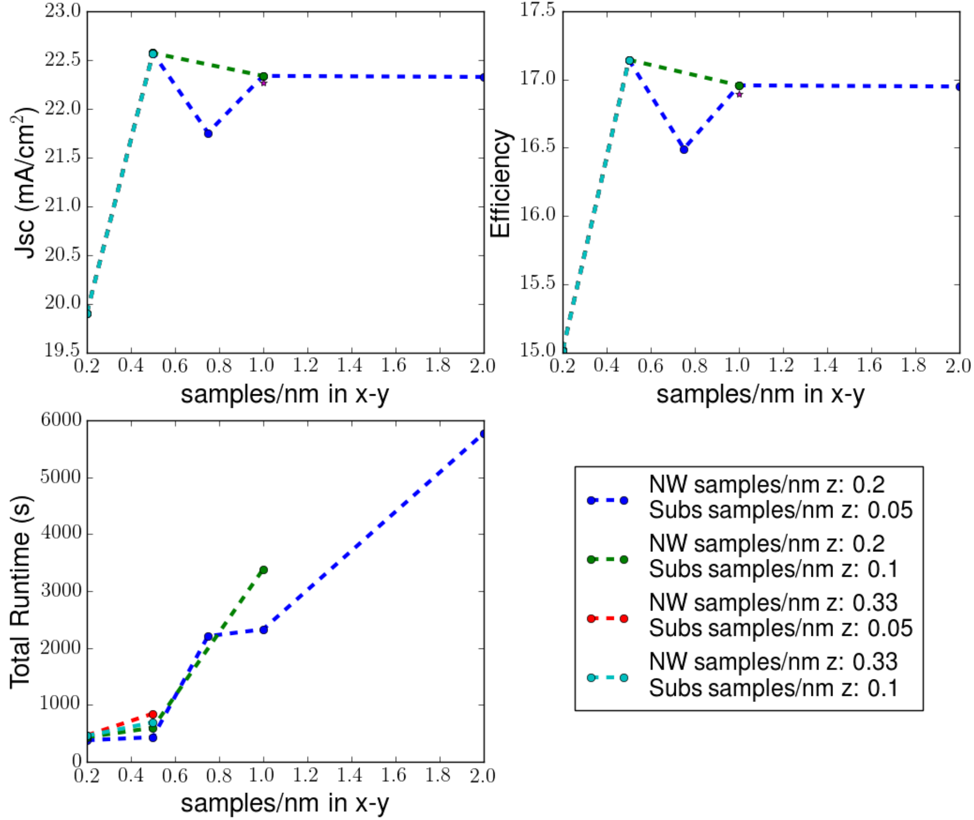

Figure 6.3: Analysis of the effect of the optical mesh density on short-circuit current density J_{sc} (top left plot) and the device efficiency (top right plot). 2% self-convergence by comparing one test to a test at the next higher mesh density is reached using 1 sample per nm along the x and y directions. The choice of z sampling is insignificant. The computation time of the electrical simulations and optical data export are shown in the bottom left plot.

6.3 Convergence Testing

To ensure accuracy of the model with respect to the density of sampling points in the optical mesh, a sensitivity analysis was performed to test the sensitivity of the short circuit current density J_{sc} and efficiency η to variations in the sampling density. Results are shown in Figure 6.3 for the optically optimized nanowire geometry of Chapter 5. In this sensitivity analysis, 3 meshing parameters were tuned: the number of samples per nm along x and y for all layers (the same for all layers), the number of samples per nm along z in the nanowire

layer, and the number of samples per nm along z in the substrate. The meshing parameters for the irregular FVM electrical mesh were held fixed, with mesh elements held to be no larger than 200 nm in diameter. The goal of the sensitivity analysis was to self-converge the results to within 2% by comparing one test to a test at the next higher mesh density while also minimizing runtime. The plot indicates that the choice of z-sampling has almost no effect on the results, so the least dense z-sampling scheme was used (corresponding to the blue line). The observed convergence behavior is non-monotonic, making it difficult to extrapolate results beyond the parameter regime explored here. This non-monoticity can be primarily attributed to the fact that here we are observing the effect of tuning a meshing parameter of the 3D regular grid used in the optical simulation on the output of the 2D electrical simulation, which uses an irregular FVM mesh. Due to the complicated series of steps involved in this geometric reduction and interpolation from a regular grid onto an irregular grid, we expect complex, non-monotonic convergence behavior. In the x-y plane, 1 sample per nm was used as it was the least dense sampling scheme to reach convergence.

6.4 Electrical Model and Optimization

A summary of the parameters in the simulation is shown in Table 6.1. In the optimization, the total nanowire height was held fixed at a height achievable by modern growth methods [117, 16]. The relative heights of the emitter region and doping region were allowed to vary such that the sum of the emitter, intrinsic, and base regions remained fixed. Both the emitter and base regions were constrained to have a minimum height of 5 nm.

To compute current voltage characteristics, at each parameter set tested by the optimizer a voltage sweep was performed. The current at each terminal of the device was computed at each voltage, allowing computation of the power produced by the device according to

$$P(V) = JV. \tag{6.1}$$

The maximum power point P_m can be computed from the max of $P(V)$, which then allows computation of the efficiency η according to

$$\eta = \frac{P_m}{P_{inc}} \tag{6.2}$$

where P_{inc} is the incident power of the AM1.5G spectrum integrated over the entire solar spectrum

$$\int_0^\infty I_{\text{AM1.5G}}(\lambda) d\lambda \tag{6.3}$$

which is normalized to 1000 W/m^2. The optimization procedure uses a Quasi-Newton optimization method to vary emitter thickness, base thickness, emitter doping, and base doping to maximize η subject to the above constraints. This optimization technique is appropriate because it does not require an analytic expression for the derivatives of the response function η. Instead, the algorithm computes finite difference approximations to

Parameter	**Type**	**Optimized Value**
ITO Height	Fixed	300 nm
NW Height	Fixed	2 microns
Substrate Height	Fixed	1 micron
Substrate Doping	Fixed	$2 \times 10^{19}\,\text{cm}^{-3}$
NW Emitter Height*	Optimized	5 nm
NW Emitter Doping*	Optimized	$1 \times 10^{19}\,\text{cm}^{-3}$
NW Intrinsic Height	Fixed	1.385 microns
NW Intrinsic Doping	Fixed	$1 \times 10^{15}\,\text{cm}^{-3}$
NW Base Height*	Optimized	610 nm
NW Base Doping	Optimized	$3.37 \times 10^{18}\,\text{cm}^{-3}$
NW Radius	Fixed	96 nm
Shell Thickness	Fixed	20 nm
Array Period	Fixed	326 nm
SiO_2 Height	Fixed	30 nm
Surface Recombination Velocity	Fixed	3000 cm s^{-1}
Bulk Carrier Lifetime	Fixed	10^{-6} s

Table 6.1: Fixed parameters and optimization results of the electrical simulation. Parameters marked with a * reached the boundary values enforced by constraints on the optimizer. Intrinsic doping was held fixed at a level found in real nanowire devices. Initial values for optimized parameters are shown in Table 6.2.

Parameter	**Initial Value**
NW Emitter Height	307.5 nm
NW Emitter Doping	$1 \times 10^{18}\,\text{cm}^{-3}$
NW Base Height	307.5 nm
NW Base Doping	$3.162 \times 10^{18}\,\text{cm}^{-3}$

Table 6.2: Initial values chosen before optimization for the optimized parameters in Table 6.1

the gradient along each optimization step using the Broyden–Fletcher–Goldfarb–Shanno update [118, 53]. The path taken through parameter space by the optimizer is shown in Fig. 6.4.

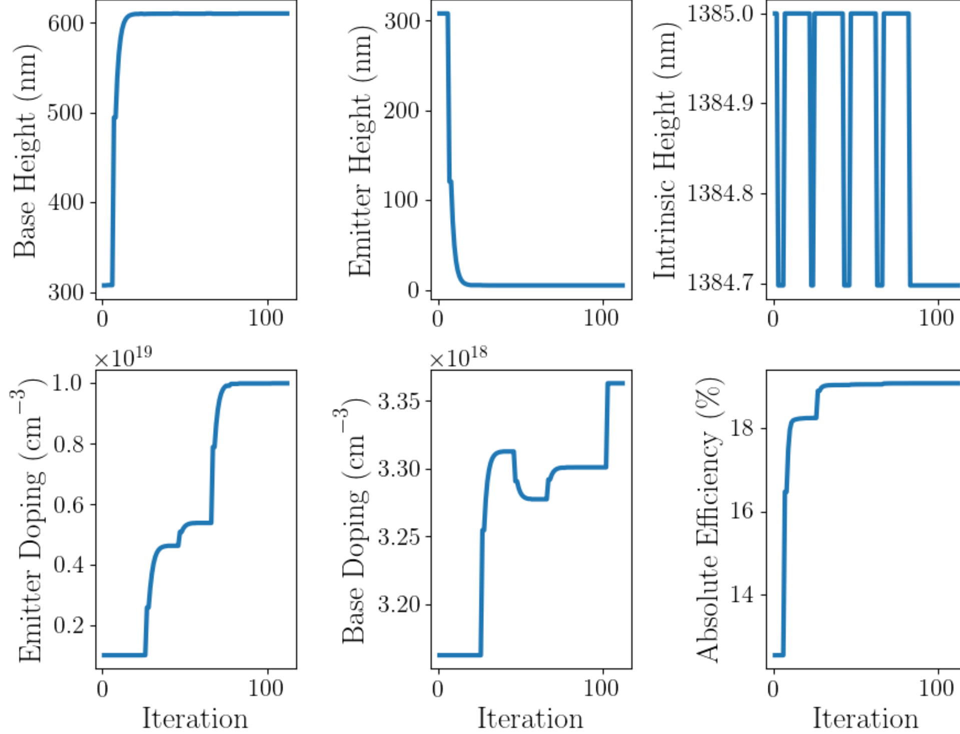

Figure 6.4: Doping region heights, doping levels, and device efficiency plotted against optimizer iteration number, showing the path the optimizer took through parameter space. Left most points on the plots indicate initial, pre-optimization values for all parameters (see Table 6.2 and Table 6.1). The flat regions on the right side of the base height, emitter height, and emitter doping plots indicate where the optimizer reached the boundary values set on those parameters.

6.5 Results

Values for the short circuit current J_{sc}, open circuit voltage V_{oc}, and efficiency η are show before and after optimization in Table 6.3. The current-voltage curves of the starting device structure and the optimized device structure are shown in Fig. 6.5. The open-circuit voltage V_{oc} and the short circuit current J_{sc} can be computed from the x and y intercepts, respectively, of these curves. As expected, V_{oc} changes very little with optimization, as V_{oc} is limited by the band gap of GaAs. The photocurrent density J_{ph} does not change with optimization because the optical model is independent of doping and the optimization does not change the overall geometric structure of the device, only the relative heights of doping regions within a nanowire of fixed total height. Optimization significantly improves J_{sc}

Parameter	Pre-Optimization Value	Post-Optimization Value	Percent Increase
J_{ph}	$26.58\,\mathrm{mA\,cm^{-2}}$	$26.58\,\mathrm{mA\,cm^{-2}}$	0
J_{sc}	$16.55\,\mathrm{mA\,cm^{-2}}$	$25.15\,\mathrm{mA\,cm^{-2}}$	51.96
V_{oc}	0.88 V	0.89 V	1.14
η	11.30%	17.17%	52.03

Table 6.3: Key performance parameters of the device before and after optimization

Mechanism	Value ($\mathrm{mA\,cm^{-2}}$)
Back Contact Surface	0.83
Core/Shell Surface	0.197
SRH Bulk	0.014
Auger Bulk	0.053
Radiative Bulk	0.003

Table 6.4: Contributions to current loss in units of $\mathrm{mA\,cm^{-2}}$ from both surface and bulk recombination processes. The dominant recombination process is due to minority carrier recombination at the back contact, which can be easily removed with proper device design.

relative to a naive guess for the initial device structure by about 10 mA/cm^2, and is smaller than J_{ph} (the maximal possible current achievable with the given optical absorption) by only $1.43\,\mathrm{mA\,cm^{-2}}$. Contributions to this loss from the various recombination mechanisms are shown in Table 6.4 as "recombination currents". The currents are computed using

$$J_{recomb} = q\frac{U}{A} \tag{6.4}$$

where A is the area of the device and q is the electron charge. The dominant loss mechanism is minority carrier recombination at the back contact, which can be easily reduced with a thicker substrate. We should find that $J_{ph} = J_{sc} + J_{recomb}$, but Table 6.4 shows that there is $0.33\,\mathrm{mA\,cm^{-2}}$ of loss currently unattributed to any mechanism, accounting for 1.2% of J_{ph}. We are not sure of the cause of this discrepancy but believe that the overall accounting for loss processes gives the correct qualitative analysis.

The improvement gained from optimization can be explained by looking to the band structure (see Figure 6.6) of and recombination within the unoptimized and optimized device. The increased height of the p-type doping region increases the thickness of the potential barrier to electrons, limiting their probability of being lost into the substrate. Additionally, reducing the thickness of the emitter region shifts carrier generation into the intrinsic region, meaning carriers are separated by means of the built-in electric field and do not rely on diffusion to reach the electron contact. Figure 6.7 shows the optical generation profile and the electric field on a line cut along the length of the nanowire through its center. Reducing the emitter thickness moves the region of high electric field such that it contains the region of maximum carrier generation, maximizing carrier separation.

To determine the effect of optimization on carrier recombination, the total bulk recombination rate in the device was computed by integrating radiative, Auger, and SRH

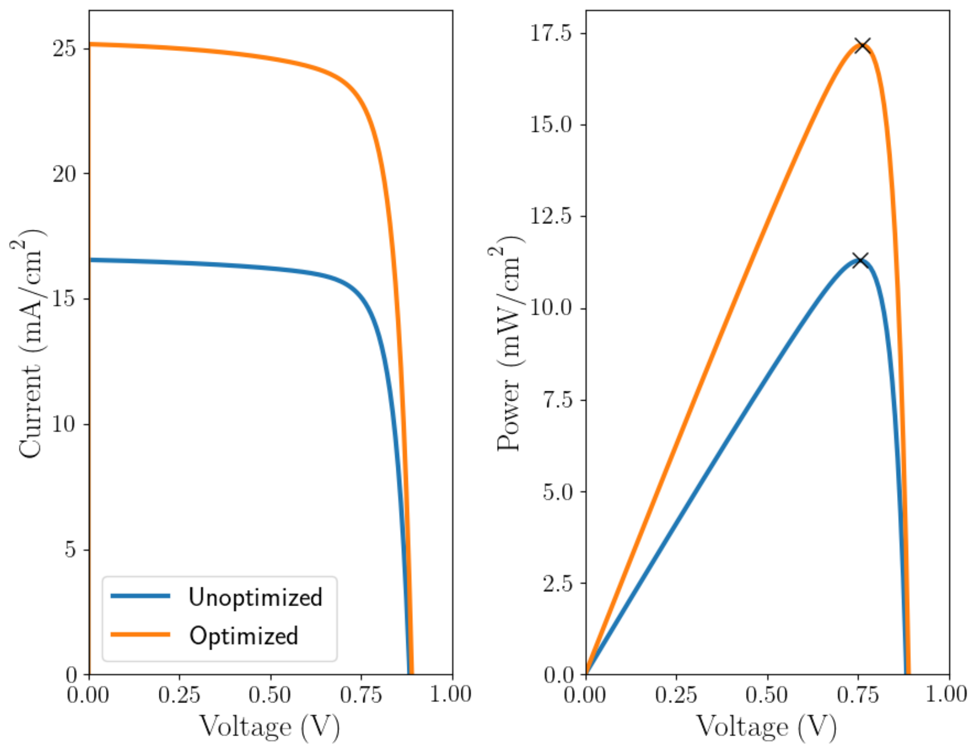

Figure 6.5: Current-voltage curve (left), from which V_{oc} and J_{sc} are extracted, and power-voltage curve (right) for the optimized (orange line) and unoptimized (blue line) device. Maximum power point is marked with a black X, and occurs at 0.75 V in both cases.

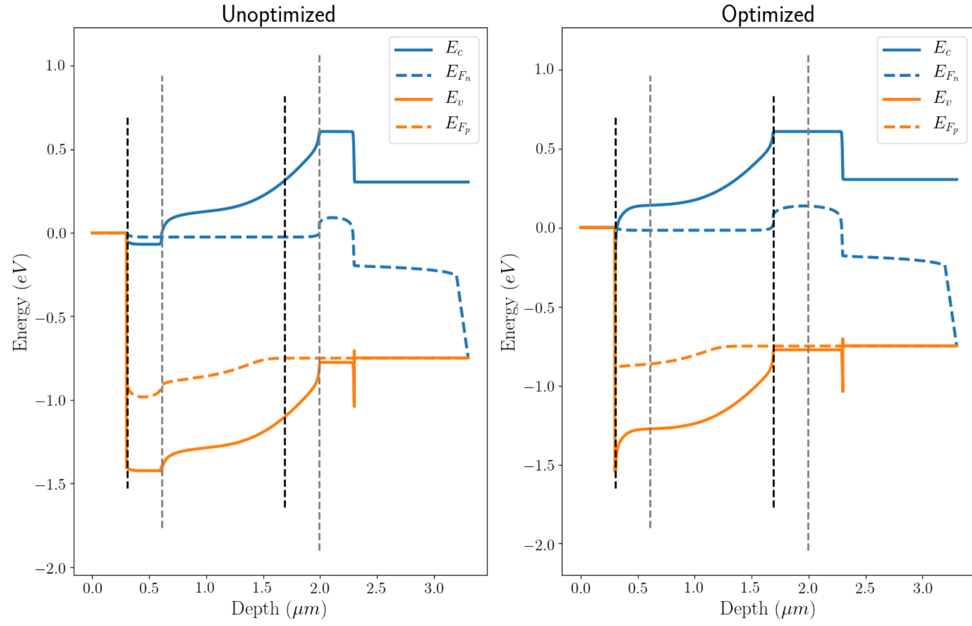

Figure 6.6: Band diagrams containing the conduction band and valence band edges (solid lines) and the electron and hole quasi-Fermi energies (dotted lines) at maximum power point (0.75 V). Electron contact is at the left edge, hole contact is at the right. Grey dotted lines indicate the initial emitter and base region boundaries. Black dotted lines indicate the emitter and base region boundaries after optimization.

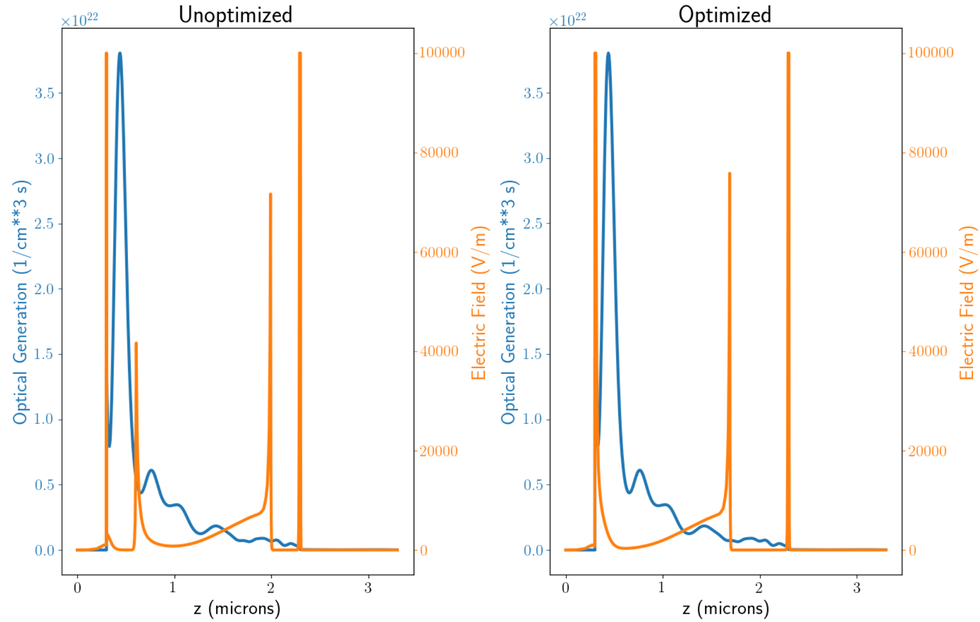

Figure 6.7: Optical generation (left axis) and electric field (right axis) on a line cut along the length of the nanowire through its center. In the optimized structure, the peak of optical generation (at around 500 nm) is fully contained in the intrinsic region, where carriers can be separated by the electric field.

Parameter	Pre-Optimization Value (s^{-1})	Post-Optimization Value
U_{surf}^{total}	$2.30 \times 10^6\,\text{s}^{-1}$	$1.31 \times 10^6\,\text{s}^{-1}$
$U_{surf}^{\text{emitter}}$	$1.33 \times 10^6\,\text{s}^{-1}$	$19.93\,\text{s}^{-1}$
$U_{surf}^{\text{intrinsic}}$	$9.62 \times 10^5\,\text{s}^{-1}$	$1.27 \times 10^6\,\text{s}^{-1}$
U_{surf}^{base}	$3.49 \times 10^3\,\text{s}^{-1}$	$3.75 \times 10^4\,\text{s}^{-1}$

Table 6.5: Total surface recombination in the device before and after optimization, broken down by the various doping regions. Minor contributions from the shell-cyclotene interface to the total are not shown. Optimization drastically reduces surface recombination in the intrinsic and emitter regions, at the cost of a slight increase in the base region

recombination rates over the volume according to

$$U_{\text{total}}^{\text{bulk}} = \int dV\, U_{SRH} + U_{Auger} + U_{rad}. \tag{6.5}$$

Comparing $U_{\text{total}}^{\text{bulk}}$ between the optimized and unoptimized device structure gives some sense of how much the optimizer is tuning doping levels to minimize bulk recombination. Total bulk recombination decreased after optimization, with $U_{\text{total, opt}}^{\text{bulk}} = 4.67 \times 10^5 s^{-1}$ and $U_{\text{total, unopt}}^{\text{bulk}} = 5.92 \times 10^5 s^{-1}$, indicating the optimizer tuned doping levels to minimize bulk recombination. Optimization also drastically reduced total surface recombination. Values of the integral

$$U_{\text{total}}^{\text{surf}} = \int_{\text{core-shell}} dA\, U_{surf} \tag{6.6}$$

integrated over the entire core-shell interface and the portion of the core-shell interface contained in each of the emitter, intrinsic, and base doping regions is shown in Table 6.5.

Optimization reduces total bulk and surface recombination by both tuning doping levels in the base and emitter and modifying the total surface area of the core-shell interface contained in each region.

6.6 Conclusion

Results from Trojnar et al. are corroborated, and thin emitters do indeed offer the best device performance for axial junction p-i-n nanowire solar cells [48]. In contrast, here we see thick intrinsic regions are not necessarily best. In their work, they studied GaAs nanowires on p-type GaAs substrates, allowing the substrate to be used as a base. Here the base exists in the nanowire, and the base height within the nanowire must be increased to maximize efficiency. Efficiency losses in the device shown here relative to their work can be attributed to lower optical absorption in the substrate and reduced transport across the NW-Substrate interface.

The benefit of automatic, algorithmic optimization is clearly demonstrated. Automated, algorithmic optimizations enable a more thorough search of the parameter space than the manual, low dimensional line cuts previously reported in the literature, and have

the potential to reveal interesting, useful device physics that might otherwise be missed. There is much still to be learned from full device optimizations, where both the device geometry and internal electrical parameters are simultaneously optimized. Such a study could indicate the optimal nanowire height, finding the right balance between reduced surface recombination and increased optical absorption. However, this work shows that even restricted optimization over doping levels and doping region heights for a fixed geometry can significantly enhance device performance for nanowire solar cells. This information may be useful for device fabricators who have geometric growth constraints, but full control over doping levels during growth.

Chapter 7

Conclusion & Future Work

In this work a fully coupled, automated optoelectronic device model of nanowire solar cells was constructed and tested on a realistic set of example nanowire systems. An optical modeling algorithm underrepresented in the nanowire modeling literature, RCWA, was used to build the optical model. Key modifications were made to the algorithm to enhance its accuracy, and after enhancement it was found to be an appropriate, lightweight technique for optical modeling of nanowire systems. Purely optical optimizations of nanowire solar cells maximizing optical absorption were performed using our enhanced implementation of RCWA, and results showed that optical optimization of passivated GaAs nanowire solar cells can provide measurable performance benefits by maximizing the photocurrent.

An automated software system was then constructed to feed the results of the full 3D optical model into a 2D electrical model for the purposes of computing key electrical performance metrics (efficiency, maximum power point, etc). The electrical model was built using a commercial software package TCAD Sentaurus, tuned to utilize device physics appropriate for nanowire solar cells. Using the optimized geometric output of the optical model, an algorithmic optimization of several electronic device parameters was performed to maximize the device efficiency. Significant performance enhancements were achieved over an unoptimized initial design.

The primary success of this work was the construction of a robust, reusable tool that can be easily modified to explore new systems. As such, there is much that can still be done. In particular, a global, algorithmic optimization of the fully coupled optoelectronic device model has not yet been performed. To do this, the memory management code of the optical model must be improved to handle the computational demands of such an optimization. Once improved, novel results not yet published in the literature can easily be generated using the framework constructed here. We anticipate interesting results from a coupled optoelectronic optimization, as parameter regimes that optimize optical absorption may be less than optimal for carrier collection, and vice versa. Such an optimization would be hugely beneficial to device fabricators, and would set useful targets for their nanowire growth and device fabrication processes.

APPENDICES

Appendix A

Derivation of Fourier Space Maxwell's Equations

Restating Eq. (3.24) below:

$$\sum_G i(k_x + G_x)H_{G,y}(z)e^{i(\mathbf{k}+\mathbf{G})\cdot\mathbf{r}} - \sum_G i(k_y + G_y)H_{G,x}(z)e^{i(\mathbf{k}+\mathbf{G})\cdot\mathbf{r}} = -i\omega \sum_{G'} \epsilon_{G'} e^{i\mathbf{G}'\cdot\mathbf{r}} \sum_G E_{G,z}(z)e^{i(\mathbf{k}+\mathbf{G})\cdot\mathbf{r}}$$

We multiply both sides of the equation by $e^{-i(\mathbf{k}+\mathbf{G}'')}$ for a particular $\mathbf{G}''$ to get

$$\sum_G i(k_x + G_x)H_{G,y}(z)e^{i(\mathbf{G}-\mathbf{G}'')\cdot\mathbf{r}} - \sum_G i(k_y + G_y)H_{G,x}(z)e^{i(\mathbf{G}-\mathbf{G}'')\cdot\mathbf{r}} = -i\omega \sum_{G\prime} \sum_G \epsilon_{G'} E_{G,z}(z)e^{i(\mathbf{G}'+\mathbf{G}-\mathbf{G}'')\cdot\mathbf{r}} \tag{A.1}$$

We know by the orthogonality of plane waves that when integrating over the real-space unit cell we have

$$\int_{cell} e^{i\mathbf{G}\cdot\mathbf{r}} d\mathbf{r} = |L_r|\delta_{\mathbf{G},0} \tag{A.2}$$

where δ is the Kronecker delta. Integrating both sides of Eq. (A.1) over the unit cell we get

$$\sum_G i(k_x + G_x)H_{G,y}(z)\delta_{\mathbf{G},\mathbf{G}''} - \sum_G i(k_y + G_y)H_{G,x}(z)\delta_{\mathbf{G},\mathbf{G}''} = -i\omega \sum_{G\prime} \sum_G \epsilon_{G'} E_{G,z}(z)\delta_{\mathbf{G}',\mathbf{G}''-\mathbf{G}} \tag{A.3}$$

The Kronecker delta $\delta_{\mathbf{G},\mathbf{G}''}$ collapses all the sums over $\mathbf{G}$ on the left hand side. On the right hand side the $\delta_{\mathbf{G},\mathbf{G}''}$ forces all terms except $\mathbf{G}' = \mathbf{G}'' - \mathbf{G}$ to zero so we end up with

$$i(k_x + G''_x)H_{G'',y}(z) - i(k_y + G''_y)H_{G'',x}(z) = -i\omega \sum_G \epsilon_{G''-G} E_{G,z}(z) \tag{A.4}$$

and note that the right side is an expression of Laurent's rule shown in Eq. (3.26). This equality must hold for all G'', allowing us to express the system of equations for all G'' using the matrix notation of Section 3.4 as

$$\hat{k_x} h_y - \hat{k_y} h_x = -i\omega \hat{\epsilon} e_z \tag{A.5}$$

which is Eq. (3.38).

Appendix B

Phasor Notation

Imagine a plane wave linearly polarized along the x direction and traveling in the z direction. This means the wave vector $\vec{k} = (0, 0, k)$ and the total electric field vector $\mathbf{E} = (E_x(z,t), 0, 0)$. We can represent such a plane wave as

$$E_x(z,t) = E_o \cos(\omega t - kz + \phi) \tag{B.1}$$

where E_o is the amplitude of the total electric field vector, ω is the temporal angular frequency, and ϕ is a unitless phase. Because the field is linearly polarized along only a single direction, the amplitude of the x component is equal to the amplitude of the total field. [1]

Another way to write this would be to make the fields complex, and use what we call phasor notation. In phasor notation the x component of the field would be

$$E_x = E_o \text{Re}[e^{i\phi} e^{i(\omega t - kz)}] \tag{B.6}$$

The actual fields in real space always track the real part of this phasor. However, that *does not* mean we can always just take the real part of the phasor be done with it in all our calculations, as we will see later.

[1] If the field was not linearly polarized along a single axis, and was perhaps polarized at an angle θ from the x axis then we would have

$$\mathbf{E} = (E_x(z,t), E_y(z,t), 0) \tag{B.2}$$

$$E_x(z,t) = E_o \cos(\theta) \cos(\omega t - kz + \phi) \tag{B.3}$$

$$E_y(z,t) = E_o \sin(\theta) \cos(\omega t - kz + \phi) \tag{B.4}$$

The important thing to note here is that the amplitude of the *total* field is E_o. With the above notation we can see

$$|\mathbf{E}(0,0)| = \sqrt{E_x^2 + E_y^2} = \sqrt{E_o^2 \cos^2(\theta) + E_o^2 \sin^2(\theta)} = E_o \tag{B.5}$$

and the magnitude comes out correctly. So the point here is that it is necessary to adjust the magnitude of the individual components such that the magnitude of the total field comes out correctly.

A common way to write phasor notation is to bring the phase and the amplitude together into a single, complex quantity called the phasor amplitude or the complex amplitude. All this means is that, if we call the complex amplitude $\tilde{E}$, then

$$\tilde{E} = E_o e^{i\phi} \tag{B.7}$$

and our EM wave becomes

$$E_x = \text{Re}[\tilde{E} e^{i(\omega t - kz)}] \tag{B.8}$$

If at any point we want to get the real amplitude of the real field out of this complex amplitude, we need to take the absolute value of the complex amplitude like so:

$$E_o = |\tilde{E}| = \sqrt{\tilde{E}^* \tilde{E}} \tag{B.9}$$

As it stands now, ϕ just controls the reference phase of our wave. It basically answers the question "When $t = 0$ and $z = 0$, at what point in its oscillation is our wave?". If $\phi = 0$, then the wave is at its peak because all the amplitude is contained in the real part of the phasor, which we know the actual fields in real space must track. If $\phi = \pi/2$, then all the amplitude is contained in the imaginary part of the phasor and the actual field in real space is zero.

When solving the frequency domain Maxwell's equations, it is assumed that we are seeking solutions with $e^{i\omega t}$ time dependence for a fixed temporal angular frequency ω. This allows us to effectively just remove the time dependence entirely, and seek solutions of the form

$$\tilde{\mathbf{E}}(x, y, z) = \left(\tilde{E}_x(x, y, z), \tilde{E}_y(x, y, z), \tilde{E}_z(x, y, z)\right) \tag{B.10}$$

where the components are all complex phasors described above.

B.1 Setting Amplitudes in S4

When setting the incident amplitude in S4, we are dealing with a phasor. If we imagine that $\vec{k} = (0, 0, k)$ such that the wave is normally incident propagating along the z-direction then we have

$$\mathbf{E}(z, t) = \tilde{\mathbf{E}}_o e^{i(\omega t - kz)} \tag{B.11}$$

When setting the incident wave, $z = 0$ and for the moment we can ignore the time-dependence. The amplitude $\tilde{\mathbf{E}}_o$ is a complex quantity composed of components which are themselves complex. In other words

$$\tilde{\mathbf{E}}_o = (\tilde{E}_x, \tilde{E}_y, \tilde{E}_z) \tag{B.12}$$

where each of the components is a complex phasor which is used to encapsulate the phase of the field relative to the z=0 point (for normally incident light the z-component is zero)

$$\tilde{E}_x = E_x e^{i\phi} \tag{B.13}$$

So, by adding a complex component to the incident amplitudes, we are introducing a phase. Imagine we've extracted some *total* electric field amplitude from an incident spectrum (say the AM1.5 spectrum) of magnitude E_o. If we wanted to specify an incident beam linearly polarized along the x-direction with zero phase we would set

$$\tilde{E}_x = E_o \tag{B.14}$$

in other words the incident wave is purely real and has only an x component. If we wanted to specify an incident beam linearly polarized along the x direction whose spatial oscillation was shifted forward by $\pi/2$ radians we would set

$$\tilde{E}_x = E_o \cos(\pi/2) + iE_o \sin(\pi/2) \tag{B.15}$$

meaning the real part is zero and the imaginary part has a positive magnitude equal to E_o.

When setting circular polarizations, we need to be a bit more careful to ensure the total field has the proper amplitude. With circularly polarized light, the complex phasors of the x and y components of the field are 90 degrees or $\pi/2$ radians out of phase with one another. To specify right hand circularly polarized light defined from the perspective of the source, we must have the components of the incident wave specified as

$$\tilde{E}_x = \frac{E_o}{\sqrt{2}} \tag{B.16}$$

$$\tilde{E}_y = -i\frac{E_o}{\sqrt{2}} \tag{B.17}$$

$$\tag{B.18}$$

Notice the factor of $1/\sqrt{2}$. When including this factor, we can see that

$$|\mathbf{E}_o|^2 = |\tilde{E}_x|^2 + |\tilde{E}_y|^2 + |\tilde{E}_z|^2 \tag{B.19}$$

$$= \frac{E_o^2}{2} + \frac{E_o^2}{2} = E_o^2 \tag{B.20}$$

and the amplitude of the total field comes out correctly. Specifying the initial components in this way is equivalent to saying

$$\tilde{E}_x = E_o e^{i\phi} \tag{B.21}$$

$$\tilde{E}_y = E_o e^{i(\phi - \frac{\pi}{2})} \tag{B.22}$$

You can verify by hand that when the real part of one component reaches a maximum, the real part of the other must be zero. For left hand circular polarized light defined from the perspective of the source we would just have

$$\tilde{E}_x = \frac{E_o}{\sqrt{2}} \tag{B.23}$$

$$\tilde{E}_y = i\frac{E_o}{\sqrt{2}} \tag{B.24}$$

$$\tag{B.25}$$

which is equivalent to saying

$$\tilde{E}_x = E_o e^{i\phi} \tag{B.26}$$

$$\tilde{E}_y = E_o e^{i(\phi+\frac{\pi}{2})} \tag{B.27}$$

References

[1] GEA. *Global Energy Assessment - Toward a Sustainable Future*. Cambridge University Press, Cambridge, UK and New York, NY, USA and the International Institute for Applied Systems Analysis, Laxenburg, Austria, 2012.

[2] Nicklas Anttu. Shockley–Queisser Detailed Balance Efficiency Limit for Nanowire Solar Cells. *ACS Photonics*, 2(3):446–453, March 2015.

[3] Peter Krogstrup, Henrik Ingerslev Jørgensen, Martin Heiss, Olivier Demichel, Jeppe V. Holm, Martin Aagesen, Jesper Nygard, and Anna Fontcuberta i Morral. Single-nanowire solar cells beyond the Shockley–Queisser limit. *Nature Photonics*, 7(4):306–310, April 2013.

[4] Erik Garnett and Peidong Yang. Light Trapping in Silicon Nanowire Solar Cells. *Nano Letters*, 10(3):1082–1087, March 2010.

[5] Dick van Dam, Niels J. J. van Hoof, Yingchao Cui, Peter J. van Veldhoven, Erik P. A. M. Bakkers, Jaime Gómez Rivas, and Jos E. M. Haverkort. High-Efficiency Nanowire Solar Cells with Omnidirectionally Enhanced Absorption Due to Self-Aligned Indium–Tin–Oxide Mie Scatterers. *ACS Nano*, 10(12):11414–11419, December 2016.

[6] O. M. Ghahfarokhi, N. Anttu, L. Samuelson, and I. Aberg. Performance of GaAs Nanowire Array Solar Cells for Varying Incidence Angles. *IEEE Journal of Photovoltaics*, 6(6):1502–1508, November 2016.

[7] Jesper Wallentin, Nicklas Anttu, Damir Asoli, Maria Huffman, Ingvar Åberg, Martin H. Magnusson, Gerald Siefer, Peter Fuss-Kailuweit, Frank Dimroth, Bernd Witzigmann, H. Q. Xu, Lars Samuelson, Knut Deppert, and Magnus T. Borgström. InP Nanowire Array Solar Cells Achieving 13.8% Efficiency by Exceeding the Ray Optics Limit. *Science*, 339(6123):1057–1060, March 2013.

[8] Björn C. P. Sturmberg, Kokou B. Dossou, Lindsay C. Botten, Ara A. Asatryan, Christopher G. Poulton, Ross C. McPhedran, and C. Martijn de Sterke. Optimizing Photovoltaic Charge Generation of Nanowire Arrays: A Simple Semi-Analytic Approach. *ACS Photonics*, 1(8):683–689, August 2014.

[9] Dan Wu, Xiaohong Tang, Kai Wang, and Xianqiang Li. An Analytic Approach for Optimal Geometrical Design of GaAs Nanowires for Maximal Light Harvesting in Photovoltaic Cells. *Scientific Reports*, 7:46504, April 2017.

[10] S. Mokkapati and C. Jagadish. Review on photonic properties of nanowires for photovoltaics [Invited]. *Optics Express*, 24(15):17345–17358, July 2016.

[11] Katherine T. Fountaine, William S. Whitney, and Harry A. Atwater. Resonant absorption in semiconductor nanowires and nanowire arrays: Relating leaky waveguide modes to Bloch photonic crystal modes. *Journal of Applied Physics*, 116(15):153106, October 2014.

[12] K. M. Azizur-Rahman and R. R. LaPierre. Wavelength-selective absorptance in GaAs, InP and InAs nanowire arrays. *Nanotechnology*, 26(29):295202, 2015.

[13] Linyou Cao. *Optical Resonant germanium nanoantenna photodetectors*. PhD thesis, Stanford, 2010.

[14] Nicklas Anttu, Alireza Abrand, Damir Asoli, Magnus Heurlin, Ingvar Åberg, Lars Samuelson, and Magnus Borgström. Absorption of light in InP nanowire arrays. *Nano Research*, 7(6):816–823, June 2014.

[15] Jia Zhu, Zongfu Yu, George F. Burkhard, Ching-Mei Hsu, Stephen T. Connor, Yueqin Xu, Qi Wang, Michael McGehee, Shanhui Fan, and Yi Cui. Optical Absorption Enhancement in Amorphous Silicon Nanowire and Nanocone Arrays. *Nano Letters*, 9(1):279–282, January 2009.

[16] Y. Hu, R. R. LaPierre, M. Li, K. Chen, and J.-J. He. Optical characteristics of GaAs nanowire solar cells. *Journal of Applied Physics*, 112(10):104311, 2012.

[17] Michael D. Kelzenberg, Shannon W. Boettcher, Jan A. Petykiewicz, Daniel B. Turner-Evans, Morgan C. Putnam, Emily L. Warren, Joshua M. Spurgeon, Ryan M. Briggs, Nathan S. Lewis, and Harry A. Atwater. Enhanced absorption and carrier collection in Si wire arrays for photovoltaic applications. *Nature Materials*, 9(3):239–244, March 2010.

[18] Khalifa M. Azizur-Rahman. *Simulation of III-V Nanowires for Infrared Photodetection*. PhD thesis, 2016.

[19] Linyou Cao, Justin S. White, Joon-Shik Park, Jon A. Schuller, Bruce M. Clemens, and Mark L. Brongersma. Engineering light absorption in semiconductor nanowire devices. *Nature Materials*, 8(8):643–647, August 2009.

[20] Karen L. Kavanagh. Misfit dislocations in nanowire heterostructures. *Semiconductor Science and Technology*, 25(2):024006, 2010.

[21] Veer Dhaka, Tuomas Haggren, Henri Jussila, Hua Jiang, Esko Kauppinen, Teppo Huhtio, Markku Sopanen, and Harri Lipsanen. High Quality GaAs Nanowires Grown on Glass Substrates. *Nano Letters*, 12(4):1912–1918, April 2012.

[22] M. T. Borgström, M. H. Magnusson, F. Dimroth, G. Siefer, O. Höhn, H. Riel, H. Schmid, S. Wirths, M. Björk, I. Åberg, W. Peijnenburg, M. Vijver, M. Tchernycheva, V. Piazza, and L. Samuelson. Towards Nanowire Tandem Junction Solar Cells on Silicon. *IEEE Journal of Photovoltaics*, 8(3):733–740, May 2018.

[23] Erik C. Garnett, Mark L. Brongersma, Yi Cui, and Michael D. McGehee. Nanowire Solar Cells. *Annual Review of Materials Research*, 41(1):269–295, 2011.

[24] Erik C. Garnett and Peidong Yang. Silicon Nanowire Radial p-n Junction Solar Cells. *Journal of the American Chemical Society*, 130(29):9224–9225, July 2008.

[25] C. Colombo, M. Heib, M. Grätzel, and A. Fontcuberta i Morral. Gallium arsenide p-i-n radial structures for photovoltaic applications. *Applied Physics Letters*, 94(17):173108, April 2009.

[26] Vladimir Maryasin, Davide Bucci, Quentin Rafhay, Federico Panicco, Jérôme Michallon, and Anne Kaminski-Cachopo. Technological guidelines for the design of tandem III-V nanowire on Si solar cells from opto-electrical simulations. *Solar Energy Materials and Solar Cells*, 172:314–323, December 2017.

[27] Brendan M. Kayes, Harry A. Atwater, and Nathan S. Lewis. Comparison of the device physics principles of planar and radial p-n junction nanorod solar cells. *Journal of Applied Physics*, 97(11):114302, May 2005.

[28] Soumyadeep Misra, Linwei Yu, Wanghua Chen, Martin Foldyna, and Pere Roca i Cabarrocas. A review on plasma-assisted VLS synthesis of silicon nanowires and radial junction solar cells. *Journal of Physics D: Applied Physics*, 47(39):393001, September 2014.

[29] Ziyuan Li, Hark Hoe Tan, Chennupati Jagadish, and Lan Fu. III–V Semiconductor Single Nanowire Solar Cells: A Review. *Advanced Materials Technologies*, 3(9):1800005, September 2018.

[30] I. Åberg, G. Vescovi, D. Asoli, U. Naseem, J. P. Gilboy, C. Sundvall, A. Dahlgren, K. E. Svensson, N. Anttu, M. T. Björk, and L. Samuelson. A GaAs Nanowire Array Solar Cell With 15.3% Efficiency at 1 Sun. *IEEE Journal of Photovoltaics*, 6(1):185–190, January 2016.

[31] A. C. E. Chia, M. Tirado, Y. Li, S. Zhao, Z. Mi, D. Comedi, and R. R. LaPierre. Electrical transport and optical model of GaAs-AlInP core-shell nanowires. *Journal of Applied Physics*, 111(9):094319, May 2012.

[32] N. Huang and M. L. Povinelli. Design of Passivation Layers on Axial Junction GaAs Nanowire Solar Cells. *IEEE Journal of Photovoltaics*, 4(6):1511–1517, November 2014.

[33] A. C. E. Chia, M. Tirado, F. Thouin, R. Leonelli, D. Comedi, and R. R. LaPierre. Surface depletion and electrical transport model of AlInP-passivated GaAs nanowires. *Semiconductor Science and Technology*, 28(10):105026, 2013.

[34] D. E. Aspnes. Recombination at semiconductor surfaces and interfaces. *Surface Science*, 132(1):406–421, September 1983.

[35] David S. L. Mui and L. A. Coldren. Effects of surface recombination on carrier distributions and device characteristics. *Journal of Applied Physics*, 78(5):3208–3215, September 1995.

[36] O Demichel, M Heiss, J Bleuse, and H Mariette. Impact of surfaces on the optical properties of GaAs nanowires. *Appl. Phys. Lett.*, page 3.

[37] Daniel E. Perea, Eric R. Hemesath, Edwin J. Schwalbach, Jessica L. Lensch-Falk, Peter W. Voorhees, and Lincoln J. Lauhon. Direct measurement of dopant distribution in an individual vapour–liquid–solid nanowire. *Nature Nanotechnology*, 4(5):315–319, May 2009.

[38] Jonathan E. Allen, Daniel E. Perea, Eric R. Hemesath, and Lincoln J. Lauhon. Nonuniform Nanowire Doping Profiles Revealed by Quantitative Scanning Photocurrent Microscopy. *Advanced Materials*, 21(30):3067–3072, August 2009.

[39] Kevin G. Stamplecoskie, Ling Ju, Shokouh S. Farvid, and Pavle V. Radovanovic. General Control of Transition-Metal-Doped GaN Nanowire Growth: Toward Understanding the Mechanism of Dopant Incorporation. *Nano Letters*, 8(9):2674–2681, September 2008.

[40] I. Kimukin, M. Saif Islam, and R. Stanley Williams. Surface depletion thickness of p-doped silicon nanowires grown using metal-catalysed chemical vapour deposition. *Nanotechnology*, 17(11):S240, 2006.

[41] E. Tutuc, J. O. Chu, J. A. Ott, and S. Guha. Doping of germanium nanowires grown in presence of PH3. *Applied Physics Letters*, 89(26):263101, December 2006.

[42] N. Isik Goktas, E. M. Fiordaliso, and R. R. LaPierre. Doping assessment in GaAs nanowires. *Nanotechnology*, 29(23):234001, 2018.

[43] Josef A. Czaban, David A. Thompson, and Ray R. LaPierre. GaAs Core-Shell Nanowires for Photovoltaic Applications. *Nano Letters*, 9(1):148–154, January 2009.

[44] R. R. LaPierre. Numerical model of current-voltage characteristics and efficiency of GaAs nanowire solar cells. *Journal of Applied Physics*, 109(3):034311, February 2011.

[45] J. Kupec and B. Witzigmann. Dispersion, Wave Propagation and Efficiency Analysis of Nanowire Solar Cells. *Optics Express*, 17(12):10399–10410, June 2009.

[46] Chenxi Lin and Michelle L. Povinelli. Optical absorption enhancement in silicon nanowire arrays with a large lattice constant for photovoltaic applications. *Optics Express*, 17(22):19371–19381, October 2009.

[47] Shuqing Yu, Friedhard Römer, and Bernd Witzigmann. Analysis of surface recombination in nanowire array solar cells. *Journal of Photonics for Energy*, 2(1):028002, September 2012.

[48] Anna H. Trojnar, Christopher E. Valdivia, Ray R. LaPierre, Karin Hinzer, and Jacob J. Krich. Optimizations of GaAs Nanowire Solar Cells. *IEEE Journal of Photovoltaics*, 6(6):1494–1501, November 2016.

[49] Xufeng Wang, Mohammad Ryyan Khan, Mark Lundstrom, and Peter Bermel. Performance-limiting factors for GaAs-based single nanowire photovoltaics. *Optics Express*, 22(S2):A344, March 2014.

[50] Jenny Nelson. *The Physics of Solar Cells*. Imperial College Press, 2003.

[51] David J Griffiths. *Introduction to Electrodynamics*. Pearson, 4 edition, 2013.

[52] John David Jackson. *Classical Electrodynamics*. Wiley, 3 edition, 1999.

[53] Sentaurus^{TM} Device User Guide. page 1574.

[54] V Palankovski, G Kaiblinger-Grujin, and S Selberherr. Study of dopant-dependent band gap narrowing in compound semiconductor devices. *Materials Science and Engineering: B*, 66(1):46–49, December 1999.

[55] S. Noor Mohammad and M. Abdus Sobhan. Doping Dependent Bandgap Narrowing in Silicon and Germanium. *physica status solidi (b)*, 156(1):287–302, November 1989.

[56] S. C. Jain and D. J. Roulston. A simple expression for band gap narrowing (BGN) in heavily doped Si, Ge, GaAs and GexSi1-x strained layers. *Solid-State Electronics*, 34(5):453–465, May 1991.

[57] J. W. Slotboom and H. C. de Graaff. Measurements of bandgap narrowing in Si bipolar transistors. *Solid-State Electronics*, 19(10):857–862, October 1976.

[58] Herbert S. Bennett and Charles L. Wilson. Statistical comparisons of data on bandgap narrowing in heavily doped silicon: Electrical and optical measurements. *Journal of Applied Physics*, 55(10):3582–3587, May 1984.

[59] J. del Alamo, S. Swirhun, and R. M. Swanson. Measuring and modeling minority carrier transport in heavily doped silicon. *Solid-State Electronics*, 28(1):47–54, January 1985.

[60] William Shockley and Hans J. Queisser. Detailed Balance Limit of Efficiency of p-n Junction Solar Cells. *Journal of Applied Physics*, 32(3):510–519, March 1961.

[61] T. Trupke, M. A. Green, P. Würfel, P. P. Altermatt, A. Wang, J. Zhao, and R. Corkish. Temperature dependence of the radiative recombination coefficient of intrinsic crystalline silicon. *Journal of Applied Physics*, 94(8):4930–4937, September 2003.

[62] Pietro P. Altermatt. Models for numerical device simulations of crystalline silicon solar cells—a review. *Journal of Computational Electronics*, 10(3):314–330, September 2011.

[63] Y. P. Varshni. Band-to-Band Radiative Recombination in Groups IV, VI, and III-V Semiconductors (I). *physica status solidi (b)*, 19(2):459–514, January 1967.

[64] G. W. 't Hooft. The radiative recombination coefficient of GaAs from laser delay measurements and effective nonradiative carrier lifetimes. *Applied Physics Letters*, 39(5):389–390, September 1981.

[65] Peter Wurfel and Uli Wurfel. *Physics of Solar Cells: From Basic Principles to Fundamental Concepts*. Wiley-VCH, 3 edition, 2016.

[66] W. Shockley and W. T. Read. Statistics of the Recombinations of Holes and Electrons. *Physical Review*, 87(5):835–842, September 1952.

[67] D. J. Roulston, N. D. Arora, and S. G. Chamberlain. Modeling and measurement of minority-carrier lifetime versus doping in diffused layers of n+-p silicon diodes. *IEEE Transactions on Electron Devices*, 29(2):284–291, February 1982.

[68] J. G. Fossum, R. P. Mertens, D. S. Lee, and J. F. Nijs. Carrier recombination and lifetime in highly doped silicon. *Solid-State Electronics*, 26(6):569–576, June 1983.

[69] Chia-Chi Chang, Chun-Yung Chi, Maoqing Yao, Ningfeng Huang, Chun-Chung Chen, Jesse Theiss, Adam W. Bushmaker, Stephen LaLumondiere, Ting-Wei Yeh, Michelle L. Povinelli, Chongwu Zhou, P. Daniel Dapkus, and Stephen B. Cronin. Electrical and Optical Characterization of Surface Passivation in GaAs Nanowires. *Nano Letters*, 12(9):4484–4489, September 2012.

[70] Mauro Zanuccoli, Jérôme Michallon, Igor Semenihin, Claudio Fiegna, Anne Kaminski-Cachopo, Enrico Sangiorgi, and Vladimir Vyurkov. Numerical Simulation of Vertical Silicon Nanowires based Heterojunction Solar Cells. *Energy Procedia*, 38:216–222, 2013.

[71] S. M. Sze and Kwok Kwok Ng. *Physics of semiconductor devices*. Wiley-Interscience, Hoboken, N.J, 3rd ed edition, 2007.

[72] K. Horio and H. Yanai. Numerical modeling of heterojunctions including the thermionic emission mechanism at the heterojunction interface. *IEEE Transactions on Electron Devices*, 37(4):1093–1098, April 1990.

[73] Dietmar Schroeder. *Modelling of interface carrier transport for device simulation*. Springer, Place of publication not identified, 2013. OCLC: 968511152.

[74] Joachim Piprek. *Semiconductor Optoelectronic Devices: Introduction to Physics and Simulation*. Academic Press, 2003.

[75] N. D. Arora, J. R. Hauser, and D. J. Roulston. Electron and hole mobilities in silicon as a function of concentration and temperature. *IEEE Transactions on Electron Devices*, 29(2):292–295, February 1982.

[76] M. G. Moharam and T. K. Gaylord. Rigorous coupled-wave analysis of planar-grating diffraction. *JOSA*, 71(7):811–818, July 1981.

[77] M. G. Moharam and T. K. Gaylord. Diffraction analysis of dielectric surface-relief gratings. *Journal of the Optical Society of America*, 72(10):1385, October 1982.

[78] Evgeny Popov, Michel Nevière, Boris Gralak, and Gérard Tayeb. Staircase approximation validity for arbitrary-shaped gratings. *Journal of the Optical Society of America A*, 19(1):33, January 2002.

[79] Lifeng Li. Formulation and comparison of two recursive matrix algorithms for modeling layered diffraction gratings. *Journal of the Optical Society of America A*, 13(5):1024, May 1996.

[80] Philippe Lalanne and G. Michael Morris. Highly improved convergence of the coupled-wave method for TM polarization. *Journal of the Optical Society of America A*, 13(4):779, April 1996.

[81] Evgeni Popov and Michel Nevière. Grating theory: new equations in Fourier space leading to fast converging results for TM polarization. *JOSA A*, 17(10):1773–1784, October 2000.

[82] Evgeny Popov and Michel Nevière. Maxwell equations in Fourier space: fast-converging formulation for diffraction by arbitrary shaped, periodic, anisotropic media. *JOSA A*, 18(11):2886–2894, November 2001.

[83] Michel Neviere and Evgeny Popov. *Light Propagation in Periodic Media : Differential Theory and Design*. CRC Press LLC, 2003.

[84] Thomas Schuster, Johannes Ruoff, Norbert Kerwien, Stephan Rafler, and Wolfgang Osten. Normal vector method for convergence improvement using the RCWA for crossed gratings. *JOSA A*, 24(9):2880–2890, September 2007.

[85] Peter Götz, Thomas Schuster, Karsten Frenner, Stephan Rafler, and Wolfgang Osten. Normal vector method for the RCWA with automated vector field generation. *Optics express*, 16(22):17295–17301, 2008.

[86] Victor Liu and Shanhui Fan. S4: A free electromagnetic solver for layered periodic structures. *Computer Physics Communications*, 183(10):2233–2244, October 2012.

[87] D. M. Whittaker and I. S. Culshaw. Scattering-matrix treatment of patterned multilayer photonic structures. *Physical Review B*, 60(4):2610–2618, July 1999.

[88] J. G. F. Francis. The QR Transformation A Unitary Analogue to the LR Transformation—Part 1. *The Computer Journal*, 4(3):265–271, January 1961.

[89] Ralf Bräuer and Olof Bryngdahl. Electromagnetic diffraction analysis of two-dimensional gratings. *Optics Communications*, 100(1):1–5, July 1993.

[90] M. G. Moharam and T. K. Gaylord. Three-dimensional vector coupled-wave analysis of planar-grating diffraction. *Journal of the Optical Society of America*, 73(9):1105, September 1983.

[91] M. G. Moharam, T. K. Gaylord, Drew A. Pommet, and Eric B. Grann. Stable implementation of the rigorous coupled-wave analysis for surface-relief gratings: enhanced transmittance matrix approach. *JOSA A*, 12(5):1077–1086, 1995.

[92] D. Y. K. Ko and J. R. Sambles. Scattering matrix method for propagation of radiation in stratified media: attenuated total reflection studies of liquid crystals. *Journal of the Optical Society of America A*, 5(11):1863, November 1988.

[93] N. P. K. Cotter, T. W. Preist, and J. R. Sambles. Scattering-matrix approach to multilayer diffraction. *Journal of the Optical Society of America A*, 12(5):1097, May 1995.

[94] Kyle W. Robertson, Ray R. LaPierre, and Jacob J. Krich. Efficient wave optics modeling of nanowire solar cells using rigorous coupled-wave analysis. *Optics Express*, 27(4):A133–A147, February 2019.

[95] Jan Kupec, Ralph L. Stoop, and Bernd Witzigmann. Light absorption and emission in nanowire array solar cells. *Optics Express*, 18(26):27589–27605, December 2010.

[96] Kyle W Robertson, Ray R LaPierre, and Jacob J Krich. Optical optimization of passivated GaAs nanowire solar cells. In *IEEE PVSC*, page 5, Washington, D.C, June 2017.

[97] Qing Guo Du, Chan Hin Kam, Hilmi Volkan Demir, Hong Yu Yu, and Xiao Wei Sun. Broadband absorption enhancement in randomly positioned silicon nanowire arrays for solar cell applications. *Optics Letters*, 36(10):1884–1886, May 2011.

[98] M. G. Moharam, T. K. Gaylord, Eric B. Grann, and Drew A. Pommet. Formulation for stable and efficient implementation of the rigorous coupled-wave analysis of binary gratings. *Journal of the Optical Society of America A*, 12(5):1068–1076, 1995.

[99] Martin Weismann, Dominic FG Gallagher, and Nicolae C. Panoiu. Accurate near-field calculation in the rigorous coupled-wave analysis method. *Journal of Optics*, 17(12):125612, 2015.

[100] Philippe Lalanne and Marie Paule Jurek. Computation of the near-field pattern with the coupled-wave method for transverse magnetic polarization. *Journal of Modern Optics*, 45(7):1357–1374, July 1998.

[101] Karl Heinz Brenner. Aspects for calculating local absorption with the rigorous coupled-wave method. *Optics Express*, 18(10):10369–10376, May 2010.

[102] Evgeni A. Bezus and Leonid L. Doskolovich. Stable algorithm for the computation of the electromagnetic field distribution of eigenmodes of periodic diffraction structures. *Journal of the Optical Society of America A*, 29(11):2307–2313, 2012.

[103] Martin Costabel and Monique Dauge. Singularities of electromagnetic fields in polyhedral domains. *Archive for Rational Mechanics and Analysis*, 151(3):221–276, April 2000.

[104] N. . Huynh and W. Heinrich. FDTD accuracy improvement by incorporation of 3D edge singularities. In *1999 IEEE MTT-S International Microwave Symposium Digest*, volume 4, pages 1573–1576, 1999.

[105] A. Farjadpour, David Roundy, Alejandro Rodriguez, M. Ibanescu, Peter Bermel, J. D. Joannopoulos, Steven G. Johnson, and G. W. Burr. Improving accuracy by subpixel smoothing in the finite-difference time domain. *Opt. Lett.*, 31(20):2972–2974, October 2006.

[106] C. Epstein and M. O'Neil. Smoothed corners and scattered waves. *SIAM J. Sci. Comput.*, 38(5):A2665–A2698, January 2016.

[107] M. G. Moharam and Andrew B. Greenwell. Rigorous analysis of field distribution and power flow in grating coupler of finite length. In *Diffractive Optics and Micro-Optics*, page DMC5. Optical Society of America, 2004.

[108] Hwi Kim, IlMin Lee, and Byoungho Lee. Extended scattering-matrix method for efficient full parallel implementation of rigorous coupled-wave analysis. *Journal of the Optical Society of America A*, 24(8):2313, August 2007.

[109] Raymond C. Rumpf. Improved formulation of scattering matrices for semi-analytical methods that is consistent with convention. *Progress In Electromagnetics Research B*, 35:241–261, 2011.

[110] Sadao Adachi. *Optical Constants of Crystalline and Amorphous Semiconductors: Numerical Data and Graphical Information*. Springer US, 1 edition, 1999.

[111] Standard tables for reference solar spectral irradiances: Direct normal and hemispherical on 37 degree tilted surface. Technical report, ASTM International, 2012.

[112] Lifeng Li. Use of Fourier series in the analysis of discontinuous periodic structures. *Journal of the Optical Society of America A*, 13(9):1870–1876, 1996.

[113] Ole Tange. GNU Parallel 2018. https://doi.org/10.5281/zenodo.1146014, March 2018.

[114] Lu Hu and Gang Chen. Analysis of Optical Absorption in Silicon Nanowire Arrays for Photovoltaic Applications. *Nano Letters*, 7(11):3249–3252, November 2007.

[115] Linyou Cao, Pengyu Fan, Alok P. Vasudev, Justin S. White, Zongfu Yu, Wenshan Cai, Jon A. Schuller, Shanhui Fan, and Mark L. Brongersma. Semiconductor Nanowire Optical Antenna Solar Absorbers. *Nano Letters*, 10(2):439–445, February 2010.

[116] Elif Ertekin, P. A. Greaney, D. C. Chrzan, and Timothy D. Sands. Equilibrium limits of coherency in strained nanowire heterostructures. *Journal of Applied Physics*, 97(11):114325, June 2005.

[117] J. P. Boulanger, A. C. E. Chia, B. Wood, S. Yazdi, T. Kasama, M. Aagesen, and R. R. LaPierre. Characterization of a Ga-Assisted GaAs Nanowire Array Solar Cell on Si Substrate. *IEEE Journal of Photovoltaics*, 6(3):661–667, May 2016.

[118] Roger Fletcher. *Practical Methods of Optimization*. Wiley, 2 edition, July 2000.